Purdue University
Purdue e-Pubs

Open Access Dissertations | Theses and Dissertations

January 2016

Shear-based Deformation Processing and Characterization of Electrical Steel Sheet

Andrew Benjamin Kustas
Purdue University

Follow this and additional works at: https://docs.lib.purdue.edu/open_access_dissertations

Recommended Citation
Kustas, Andrew Benjamin, "Shear-based Deformation Processing and Characterization of Electrical Steel Sheet" (2016). *Open Access Dissertations*. 1241.
https://docs.lib.purdue.edu/open_access_dissertations/1241

This document has been made available through Purdue e-Pubs, a service of the Purdue University Libraries. Please contact epubs@purdue.edu for additional information.

Graduate School Form
30 Updated 12/26/2015

PURDUE UNIVERSITY
GRADUATE SCHOOL
Thesis/Dissertation Acceptance

This is to certify that the thesis/dissertation prepared

By Andrew Benjamin Kustas

Entitled

SHEAR-BASED DEFORMATION PROCESSING AND CHARACTERIZATION OF ELECTRICAL STEEL SHEET

For the degree of Doctor of Philosophy

Is approved by the final examining committee:

Kevin P. Trumble
Co-chair

Srinivasan Chandrasekar
Co-chair

Rodney W. Trice

David R. Johnson

To the best of my knowledge and as understood by the student in the Thesis/Dissertation Agreement, Publication Delay, and Certification Disclaimer (Graduate School Form 32), this thesis/dissertation adheres to the provisions of Purdue University's "Policy of Integrity in Research" and the use of copyright material.

Approved by Major Professor(s): Kevin P. Trumble

Approved by: David F. Bahr 7/26/2016

Head of the Departmental Graduate Program Date

SHEAR-BASED DEFORMATION PROCESSING AND CHARACTERIZATION OF ELECTRICAL STEEL SHEET

A Dissertation

Submitted to the Faculty

of

Purdue University

by

Andrew Benjamin Kustas

In Partial Fulfillment of the

Requirements for the Degree

of

Doctor of Philosophy

August 2016

Purdue University

West Lafayette, Indiana

To my mother, father and brother, with love

ACKNOWLEDGEMENTS

The author would first like to thank his advisors, Prof. Kevin Trumble and Prof. Srinivasan Chandrasekar, for their excellent guidance and temperament, which allowed him to explore many interesting metallurgical processing phenomena. Furthermore, their general support and constant encouragement made the graduate experience enjoyable. The author also thanks his committee members, Prof. Rod Trice for first providing the initial phone conversation that motivated the author to attend Purdue and Prof. David Johnson, for assisting with several Fe-Si castings. The author also thanks Prof. Matthew Krane for supporting the author's confirmation at St. Thomas Aquinas.

The author acknowledges his colleagues and friends for support throughout graduate school. In particular, Logan, Michael, Dinakar, Kevin, Mert, Kristin, Kara, Travis, Derek, Alex, Kyle, Mitch, and Gamini.

The author also would like to thank his loving mother, father and brother – Gretchen, Frank and Ryan – and girlfriend Jessica for continued support throughout the graduate degree. Without them, this dissertation would not have been possible.

Finally, the author would like to thank God for the many blessings along the way. *The Lord is my rock, and my fortress, and my deliverer; my God, my strength, in whom I will trust; my buckler, and the horn of my salvation, and my high tower (Psalm 18:2, KJV).*

TABLE OF CONTENTS

Page

Page

LIST OF TABLES

LIST OF FIGURES

Figure Page

Figure Page

Figure Page

Figure Page

Figure Page

Figure Page

Figure Page

Figure Page

ABSTRACT

Kustas, Andrew Benjamin. Ph.D., Purdue University, August 2016. Shear-based Deformation Processing and Characterization of Electrical Steel Sheet. Major Professors: Kevin P. Trumble and Srinivasan Chandrasekar.

Processing of electrical steel (i.e., iron-silicon) alloys containing up to 6.5wt%Si into sheet is demonstrated by application of highly confined shear deformation in the form of metal cutting. Iron-silicon (Fe-Si) alloys, of major interest to electromagnetic applications, are characterized by poor workability. Through the interactive combination of simple shear, high strain rates, near-adiabatic heating and large hydrostatic pressure in the deformation zone, sheet and foil forms of bulk Fe-Si workpieces are created in a single deformation step.

A wide range of microstructures could be achieved in sheet through selection of different deformation parameters. Under ambient conditions (i.e., room temperature) and slower cutting velocities (1-2 m/s), a homogeneous, cold-worked structure resulted. With increased workpiece temperature and cutting velocity (≥4 m/s), a diffuse transition from homogeneous to localized material flow, in the form of periodic adiabatic shear bands, was observed. Suppression of these inhomogeneous flows is demonstrated by confining the deformation through a secondary cutting tool in a hybrid cutting-extrusion configuration called large strain extrusion machining (LSEM).

Crystallographic textures of the sheets are characterized by strong simple shear textures, defined by partial {110} and <111> fibers, inclined relative to the sheet length. The orientation (inclination) of these fibers is shown to be predictably controllable over a wide range through selection of the deformation path. A one-to-one correspondence is observed between the deformation path (determined by upper bound models) and measured texture orientations (pole figures). The simple shear textures developed during deformation are found to be retained following recrystallization and grain growth treatments and models are proposed to explain the observed texture evolution.

Bulk magnetic properties of the shear-textured sheets are assessed using a closed-loop hysteresisgraph (i.e., permeameter). Full quasi-static hysteresis loops are obtained and properties including: maximum relative permeability, coercivity and hysteresis loss are tabulated. These properties are analyzed as a function of sheet structure (i.e., texture) and alloy composition and compared directly to commercially rolled Fe-Si sheet (courtesy of AK Steel). A basic model is presented to describe the processing-texture-property relationships of the shear-textured sheets with implications.

CHAPTER 1. INTRODUCTION

1.1 Electrical Steel Sheet for Electromagnetic Applications

Rolled sheets of ferromagnetic materials serve as the magnetic cores for many important electromagnetic devices, with applications ranging from large power distribution transformers to small rotating electric motors.[1] In optimizing the efficiency of these devices, the electrical and magnetic properties of the sheets composing the magnetic core must be optimized, where high magnetic permeability ($\mu = B/H$), low coercivity (H_c), high saturation induction (B_s), low core loss and low cost are most important. Of the three ferromagnetic metals available, iron and its alloys are by far the most extensively used, representing an excess of 7 million metric tons annually with a total capital of more than 10 billion dollars.[2] While a wide range of iron alloys are available, by far the largest subset (~60%) currently used as magnetic cores are alloys of iron and silicon (Fe-Si). Known variously as Fe-Si, silicon steel, or electrical steel, sheets of these alloys have been an essential part of the global soft magnetic materials market. [3]

For over the past 100 years, extensive research has been conducted on the Fe-Si alloy system in an attempt to improve upon the existing magnetic and electrical properties to maximize devices efficiencies. Efforts have focused primarily on optimizing the alloy chemistry and microstructure through basic metallurgy practices.[4] The most significant

chemistry modification has been through the addition of silicon, which improves many intrinsic magnetic properties of iron. These improvements continue with increasing silicon content until ~6.5wt%Si (12.14at%Si), at which point the magnetic properties are generally considered optimized.[5] However, the addition of silicon also severely limits the workability of the alloy and consequentially makes thermomechanical processing difficult, even at high temperatures.[6–8] Therefore, commercial rolling of Fe-Si alloys has been restricted to 1-3 wt%Si (1.97-5.79at%Si), despite theoretically improved magnetic and electrical properties at higher silicon contents. This sharp limit has reduced the application potential for Fe-Si alloys since first being developed in the late 1800s.

In addition to the chemistry modifications, significant microstructural modifications have also been a major emphasis throughout the history of Fe-Si sheet development. The primary objective has been to create microstructures characterized by magnetically favorable crystallographic textures and large grain sizes. Crystallographic texture is known to heavily influence the magnetic properties of ferromagnetic materials.[9] This is a result of the fundamental magnetic anisotropy present in various ferromagnetic crystal structures, which depend upon the specific arrangement of atoms along different crystallographic directions. Consequentially, the ideal situation is to create sheet microstructures that take advantage of this anisotropy, ultimately optimizing the device efficiency. In the case for BCC ferromagnetic materials like Fe-Si, the goal is to develop a texture that possesses a distribution of the <001> easy magnetization directions in the plane of the sheet. Unfortunately, commercial rolling has been, to date, unsuccessful at producing truly idealized crystallographic textures in Fe-Si sheet. This, in combination with the severe Si

composition restrictions, limit the alloy sheet potential. This motivates the use of alternative thermomechanical processing methods to produce sheets from Fe-Si alloys that are more closely identified with the ideal composition and texture characteristics.

1.2 Problem Statement

Commercial rolling processes cannot access the ideal magnetic characteristics of Fe-Si sheets both in terms of composition and structure (i.e., texture). The goal of this thesis is to demonstrate the use of an innovative, shear-based thermomechanical processing method to produce sheet from Fe-Si alloys and overcome some of these limitations of rolling. Specific objectives include:

1. Examine the feasibility of processing continuous sheets from high silicon iron alloys at compositions beyond the 3.5wt% Si commercial limit.
2. Characterize the microstructures and crystallographic texture development in Fe-Si sheet processed by simple shear deformation and describe as a function of processing conditions.
3. Describe preliminary processing-structure-properties relationships of high silicon content Fe-Si alloys processed by simple shear and compare with the well-studied commercial sheets.

Recently, simple shear deformation through hybrid-cutting extrusion *via* large strain extrusion machining (LSEM) was used to develop continuous sheets from Mg and Ti alloys, which also suffer from severe workability issues during rolling.[10,11] Confinement of the shear deformation in combination with high deformation temperatures and hydrostatic

pressures in LSEM has shown to suppress deformation modes traditionally leading to sheet cracking during conventional flat sheet rolling. Furthermore, the deformation can be controlled to a much larger extent in the shear process. These attributes make LSEM an attractive thermomechanical processing alternative to the current rolling processes for producing continuous Fe-Si at unconventionally high Si compositions with unchartered textures.

To fully appreciate the simple shear deformation offered by machining-based processing, a series of experiments were conducted using both conventional (free) machining and LSEM to capture a wide range of microstructural variation. Deformation conditions were varied to assess different crystallographic textures, an essential feature of the Fe-Si sheet. Finally, magnetic properties were assessed and compared with commercial Fe-Si sheet. Models are presented to elucidate mechanisms governing texture evolution and processing-structure-property relationships.

CHAPTER 2. BACKGROUND

Chapter two is divided into five sections. Section 1 introduces basic elements of ferromagnetism, including the fundamental magnetization processes and methods of describing the magnetic behavior. Section 2 details a brief history of Fe-Si alloy development, primarily focusing on the earliest literature. Section 3 describes the basic ingot metallurgy considerations for developing efficient Fe-Si alloys. Section 4 discusses commercial Fe-Si sheet with respect to the main metallurgical features and the corresponding processing routes. Section 5 briefly details the workability of Fe-Si alloys.

2.1 Fundamentals of Ferromagnetic Materials

2.1.1 Magnetization Curves and Magnetic Properties

Materials naturally exhibit one of five types of magnetism, defined by 1) diamagnetism, 2) paramagnetism, 3) ferromagnetism, 4) ferrimagnetism and 5) antiferromagnetism.[12] Ferromagnetism, the mechanism by which alloys of iron (Fe) and silicon (Si) are magnetized, are among the strongest form that exists in nature and can produce extremely large magnetization forces. A metal is believed to exhibit a ferromagnetic behavior if atoms carry a magnetic moment and the moments can become strongly aligned in a particular direction.[12] An in-depth understanding of atomic-level ferromagnetism requires a quantum-mechanical description, which is beyond the scope of

the current document. Instead, the fundamentals of ferromagnetism are defined here from a bulk (macroscopic) view.

Perhaps the best way to describe magnetism in ferromagnetic materials is by first showing a basic virgin magnetization curve. The term virgin is used here to indicate that the material was fully demagnetized prior to magnetic testing. A series of such curves are shown in Figure 2-1 for the three ferromagnetic elements. Magnetization plots are constructed by plotting the measured material magnetization force (*M* – magnetization in units of emu/cm^3 or *B* – induction in units of Tesla) that results in response to an applied magnetic field (*H*) in units of Ampere/meter or Oersteds. All virgin magnetization curves begin at the origin (0,0) point of the *M*-*H* or *B*-*H* curves. As the applied *H* field increases, the material responds with a corresponding increase in the measured magnetization, *M* or *B*. This increase continues until some critical applied *H* field is reached, after which additional applied field no longer produces a greater magnetization in the material. Once achieved, the material is said to be saturated and the magnetization is denoted by a value of M_s or B_s. This value is a commonly reported quantity in literature and is referred to as the so-called saturation magnetization (M_s) or saturation induction (B_s). Its value is dependent solely on the material composition and is considered as a structure-insensitive property, meaning that changes in the material structure do not affect the value.[9,12] As show in Figure 2-1, pure Fe has the largest saturation of the three pure ferromagnetic elements, with an M_s = 1714 emu/cm^3 = 2.15 Tesla (T). As will be shown, compositional changes can drastically alter these values.

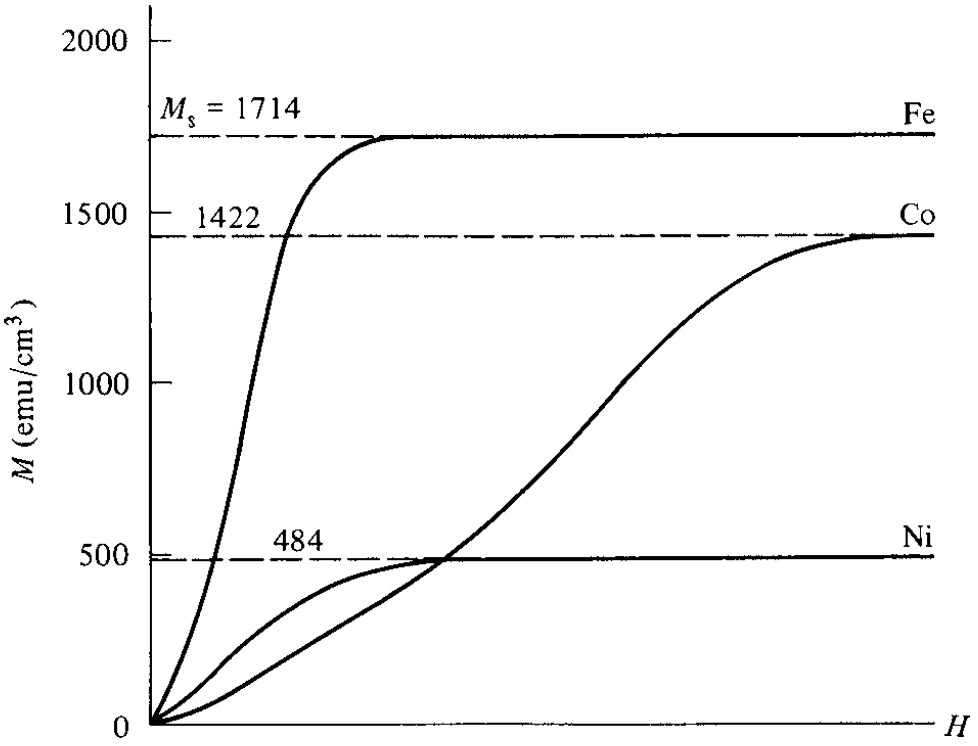

Figure 2-1 – Virgin magnetization curves for the three main ferromagnetic elements showing the saturation induction values (after [9] , used with permission of Wiley).

The overall shape of the magnetization curve is a function of both the material and the active microscale magnetization processes. Generally, the curve can be divided into three separate regions which have somewhat arbitrary cutoffs.[12] Region I, which includes the initial magnetization near the origin, is a completely reversible process and is the shortest segment along the curve. Region II, which includes an inflection point defining the maximum slope, is the beginning of an irreversible process and encompasses the decreasing portion of the curve – the so-called knee. After the knee, a separate Region III is defined which includes the material M_s or B_s value.

When the magnetization curve is plotted as induction B vs. H, the magnetic permeability μ can be calculated from the slope of the virgin curve as $\mu = B/H$. This property is important for many electromagnetic applications and is a type of measure for determining how large of a field must be applied to achieve a high induction in a given material. Fe-Si alloys, in particular, possess extremely high permeabilities, useful for motor applications.[13] Various kinds of permeability are available from the measured B-H curve, the most common of which are the initial, μ_o and the maximum μ_{max} permeabilities,.[9] Permeability is a property that is a function of both material composition and microstructure (i.e., grain size and crystallographic texture) and can therefore be modified during processing. Commonly, measured permeability values are normalized to the free space permeability, $\mu_o = 1.256 \times 10^{-6}$ Henry/meter, giving large dimensionless quantities. In this study, relative maximum permeability is reported in Chapter 7.

Once a material reaches saturation after completing the entire virgin magnetization curve, it retains that magnetizing force until the applied field is removed. Note, after a material has been magnetized beyond the stage I of a magnetization curve, it has been irreversibly magnetized. Consequentially, the return magnetization from a large H field to zero field no longer follows the same path during demagnetization and a so-called hysteresis loop develops. A full five quadrant hysteresis loop is shown in Figure 2-2. Five quadrants are shown because it also contains the virgin magnetization curve. Note the arrows indicate the direction of magnetization specifying how the curve is developed, i.e., first with a virgin curve up to $+H$ field, then a large $-H$ field and finally the same large $+H$ field.

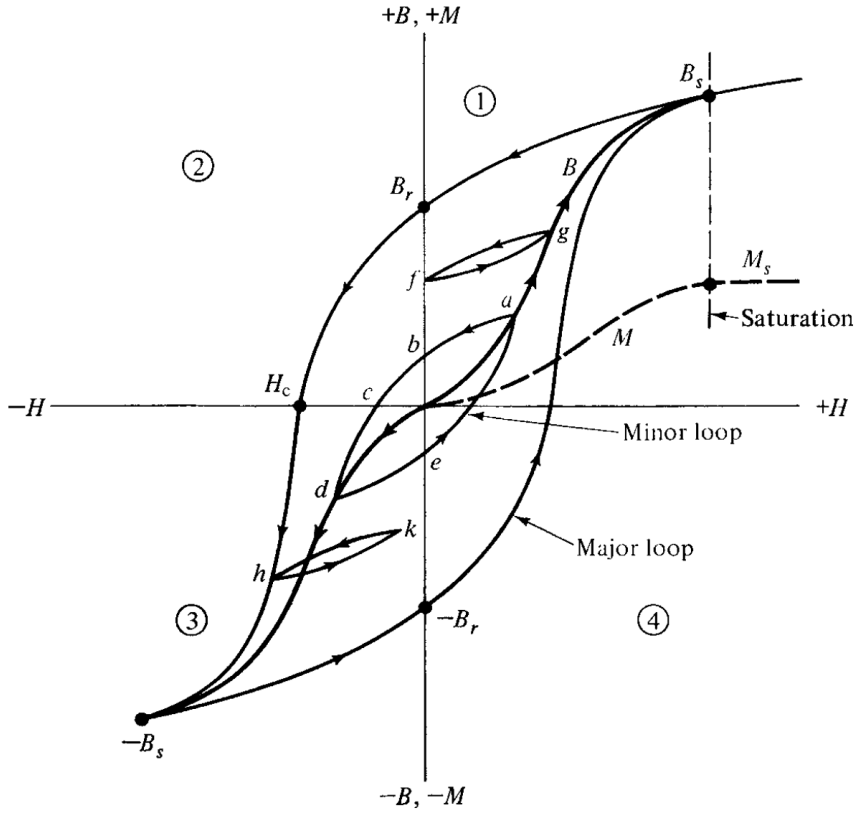

Figure 2-2 – Hysteresis loop that develops from irreversible magnetization processes showing saturation induction B_s, magnetic remanence B_r, and coercivity H_c for the major loop. Minor loops are also shown within the major (after [9], used with permission of Wiley).

Once saturation is achieved and the H field is returned to zero, there remains a remnant magnetization, B_r, in the material at some value less than the saturation induction. This remanence remains until an external magnetic field is applied in a direction opposite to the initial applied field, i.e., H becomes negative. At some point, the $–H$ field becomes large enough to bring the residual magnetization to zero, where the material is no longer magnetized. The field required to accomplish this is a property called coercivity, H_c.[9]

Coercivity gives a sense of how large a negative $-H$ field must be applied to "coerce" the material back to a demagnetized state, or a state in which the induction B or magnetization M is zero. Much like μ, this property is also a function of composition and microstructure. Magnetic materials that are easy to magnetize and then demagnetize require relatively small H values and are considered magnetically "soft", whereas necessarily larger H values are characteristic of "hard" ferromagnetic materials.[9] For Fe-Si alloys, these are considered as magnetically soft, with typical values of commercial sheet less than 100 A/m.

As the $-H$ continues to increase in magnitude, the material will reach the same saturation point when the large $+H$ field was initially applied. This process is then repeated if the field is again returned to a positive value and the full loop effectively completes one entire magnetization cycle. Note, strictly speaking, the loops are not perfectly symmetric along the $-H$ to $+H$ field but is often approximated as such.[9] The hysteresis loop encloses some specified area, which is contained within the $+H_c$ and $-H_c$ values and represents an energy of magnetization. Materials that are magnetically soft usually have relatively small areas whereas the magnetically hard materials possess significantly larger areas and therefore hysteresis loop energies. Integration of this loop area is a measure of the energy, termed as so-called hysteresis loss, W. This parameter is a type of efficiency measure and is often used as part of a total energy loss – the so called core loss – commonly reported for various ferromagnetic materials.[9] The total core loss also considers Eddy current losses that develop during AC magnetization. In this study, quasi-static magnetic properties are assessed. Therefore, hysteresis loss is characterized.

Hysteresis loops can be generated under a variety of applied field conditions, ranging from high negative and positive *H* fields to much smaller ones to develop so-called minor loops. Such loops are not considered in detail here. However, in addition to the field range, the magnetization frequency can also be varied. Loops can be generated under very slow frequencies (pseudo-DC or quasi-static hysteresis loops) up to thousands of cycles per second (kHz), depending on which most accurately characterizes the intended application. As an example, Fe-Si sheets in transformer cores are common characterized at frequencies of 50 and 60 Hz, which are the power grid frequencies for Europe and the United States, respectively.[1,13] The introduction of a magnetization frequency creates additional loss components to the total energy loss, or core loss. Core loss is complex and is a summation of many terms, the most important of which for Fe-Si sheets is the hysteresis and Eddy current losses. Under AC conditions, small Eddy-currents develop within thin laminates or sheets during magnetic cycling and effectively contribute to the total core loss. The contribution of the Eddy current losses can be estimated by measuring the total loss and subtracting the hysteresis loss component during slowly cyclic fields.[13]

Taken as a whole, key magnetic properties commonly discussed for ferromagnetic materials, like Fe-Si, include the saturation induction B_s, permeability μ, remanence B_r, coercivity H_c, and core loss (= hysteresis loss + Eddy current loss). Each of these are a function of the material, either through the microstructure, composition or combinations thereof.

2.1.2 Microscale Magnetization Processes in Ferromagnets

To gain some basic idea of how these material aspects effect the values and shape of a hysteresis loop, a brief introduction into the microscale magnetization processes is necessary. In doing so, the so-called molecular field theory (MFT), first described by Pierre Weiss in 1906, is briefly introduced.[9] The basic postulate of the theory is that a ferromagnetic material contains a series of discrete sections in which the atomic magnetic moments are aligned. These sections are so-called magnetic domains. These magnetic domains are separated by boundaries, called domain walls, and the direction of the various magnetic moments in each domain are arranged so as to minimize the total magnetostatic energy.[12] A schematic detailing an idealized domain structure during magnetization in a ferromagnetic material is shown in Figure 2-3.

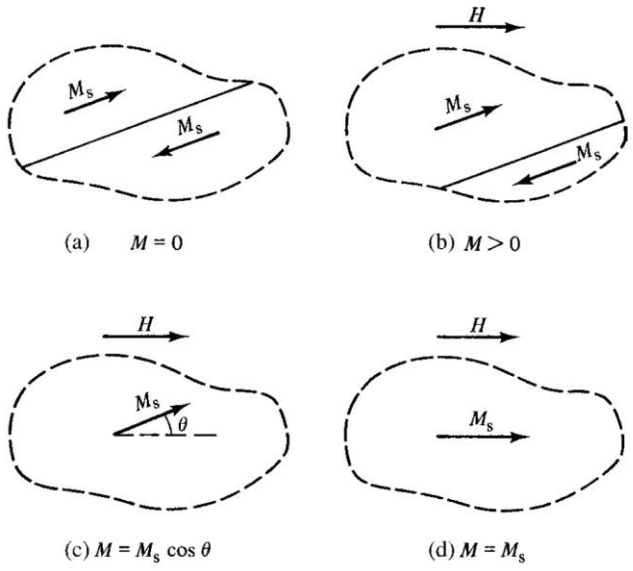

Figure 2-3 – Evolution of magnetic domain structure in a model ferromagnetic material as a function of applied field *H*. Full saturation occurs first by domain growth and later rotation into the direction of the applied field (after [9], used with permission of Wiley).

In a ferromagnetic material with no *H* field, the domains are at equilibrium. As a field is applied, particular domains tend to grow at the expense of others, analogous to the growth of grains during annealing and grain growth treatments, in an attempt to fully match the direction of the applied *H* field. This process continues until a single domain remains. If the magnetic moments of the single domain still do not align with the *H* field, it will rotate until the alignment process is complete. It is at this stage, a single domain with the atomic moments aligned parallel to the *H* field, that the material is said to be fully saturated. Although not perfectly precise, the linear and knee regions of the virgin magnetization curve represent the microscale processes of domain motion and rotation, respectively.[12]

The final magnetic properties of a material are then solely governed by the behavior of these magnetic domains. Domains in a soft ferromagnetic material, like Fe-Si, can expand and rotate more easily than those of a hard ferromagnet. As a general rule of thumb, structural aspects of metals that tend to interfere with the motion of the domains decrease the magnetic permeability and increase the coercivity and core loss (and hysteresis loss). Such obstacles include, but are not limited to, grain boundaries, secondary phases, impurities, precipitates, crystallographic textures and dislocations.[1,9,12] Most of these contributions on the properties of Fe-Si will be disclosed at various points throughout this document, however crystallographic textures are of particular importance and crystal anisotropy effects are briefly introduced.

2.1.3 Magnetic Anisotropy in BCC Crystals

In BCC systems, like Fe-Si, an intrinsic anisotropy is present and the magnetization behavior of such alloys is heavily influenced by the particular crystallographic texture. This is shown in the classic single crystal magnetization experiments in Figure 2-4 for the three main crystallographic directions. For the BCC iron alloys, magnetization along the <001> type directions is significantly easier than the <110> and <111> directions. Therefore, crystallographic texture in Fe-Si is a factor to consider in optimizing the properties. For BCC alloys like Fe, properties are considered optimized if a texture contains <001> directions along the applied field direction. This has, as of yet, not be obtained in commercial processing.

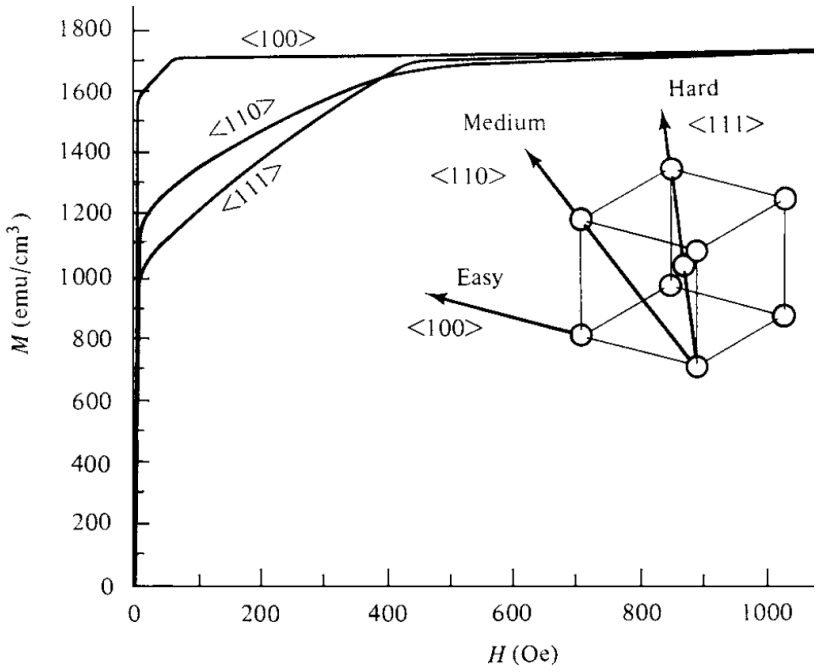

Figure 2-4 – Cubic anisotropy for BCC iron displaying the effects of different crystallographic directions on the magnetization response (after [9], used with permission of Wiley).

In summary, developing soft ferromagnetic alloys must avoid barriers that interfere with the magnetization processes to achieve acceptable properties. Controlling the composition and structure using processing metallurgy practices have been targeted at accomplishing this since Fe-Si alloys were first developed.

2.2 A Brief History of Iron-Silicon Development

Modern Fe-Si alloy development first began with the early works of the famous English metallurgist Sir Robert Hadfield in 1882, where a high carbon Fe alloy with 4wt%Si (7.65at%Si) and 8wt%Mn was created to explore the effects of various alloying additions on the properties of Fe.[4] While the initial results did not yield promising properties, it motivated the study of individual alloying additions on the properties of Fe. For the case of Si effects on Fe, the first series of investigations began in 1884 when Hadfield developed a series of Fe-Si alloys with both high and low carbon content. Interestingly, most of the initial alloys possessed unfavorable magnetic properties and instead exhibited unique mechanical properties compared to the pure irons. It was these properties that initially motivated a more detailed exploration of the Fe-Si alloys when, in 1889, Hadfield collaborated with colleague William Barrett to assess the magnetic properties of low-carbon Fe-Si alloys more extensively. The results were published in 1900 in their classical paper and revealed significantly improved magnetic properties for Fe-Si relative to the standard irons of the time.[14] Specifically, coercivity and remanence were measured to be one-half of the commercial irons and the magnetic permeability was significantly improved with only a minor reduction in the saturation induction.[4] These

findings led to immediate commercialization efforts to develop hot rolled Fe-Si alloy sheets, which began around 1905 for the United States and 1906 for England, respectively.[1,13]

Initial commercialization efforts focused on identifying critical compositional and structural effects on the properties of hot rolled Fe-Si sheet. One of the earliest reports was by Lloyd and Fisher in 1908, where improved magnetic aging response was observed for the low carbon Fe-Si sheets compared to other commercial iron materials, suggesting the importance of impurities on the magnetic response of Fe-Si.[4] These were supplemented by the notable work of Yensen in 1936, who showed reducing oxygen and carbon improved magnetic properties of Fe-Si.[15] During that same time, works of Gumlich and Vollhardt identified significant magnetic anisotropy in rolled Fe-Si sheets, suggesting crystallographic texture had an additional important influence on magnetic properties.[4] Ruder extended upon this work and revealed that recrystallization and grain growth could further improve select magnetic properties of the Fe-Si sheet, setting up the foundational work of Goss in 1935, who implemented a new cold rolling procedure for developing highly textured Fe-Si sheet, from which spurred extensive investigations into texture development effects on both hot and cold rolled Fe-Si.[16] It is important to note that hot and cold rolled Fe-Si constitute two distinct commercial sheet products sold today, broadly classified by respective crystallographic texture differences. These two products, so-called grain-oriented (GO) and non-grain-oriented (NGO) sheets are discussed in detail in Section 2.4.

In summary, initial experiments of Hadfield set the stage for continued development of Fe-Si alloys. Over the past century, sheets of Fe-Si have been developed with improved

magnetic and electrical properties as a result of a better understanding of compositional and structural effects.

2.3 Compositional Effects

From the early works of Hadfield and Barrett, Si was quickly considered as one of the essential alloying ingredients for developing improved magnetic properties in iron. Today, the effects of Si on Fe have been documented rigorously and include: 1) increased electrical resistivity to suppress eddy-current losses, 2) higher magnetic permeability, 3) reduced magnetic coercivity, 4) stabilization of the α-ferrite phase at higher temperatures, 5) improved sheet strength, 6) decreased sheet/strip density, 7) decreased magnetostrictive coefficients (i.e. low noise transformers), 8) decreased magnetocrystalline anisotropy and 9) improved corrosion resistance.[9,12] Some of these effects, along with select others, are summarized graphically in Figure 2-1 as a function of Si content (in wt%).[17] Clearly, several magnetic properties are steadily improved with increasing Si. In particular, note the sharp drop in energy (core) loss and H_c with small increases in the Si content. These aspects, in combination with the increasing μ_m, have motivated the development and study of high Si containing Fe alloys with up to 6.5wt%Si (12.14at%Si), which is considered the ideal composition in terms of minimizing total energy loss (see Figure 2-5).[5,17] However, the addition of Si also significantly reduces the intrinsic workability of the base Fe metal and causes sheet cracking during rolling. Reasons for the embrittlement are related to a modification in dislocation behavior of the pure Fe, which is discussed briefly in Section 2.5.[18,19] Therefore, due to the limited workability, commercial Fe-Si sheets are usually restricted to 0.5-3.5wt%Si (1-6.73at%Si).[20] To overcome these limitations in

workability, non-thermomechanical processing methods have been attempted to manufacture Fe-Si sheet with higher Si content at or near the ideal composition. These include casting[8,21], hot forging[6], sputter deposition[22], spray forming[23], direct powder rolling[24] and CVD siliconizing.[5] None have seen enough commercial success to replace the current rolled Fe-3wt%Si sheets, despite inherently improved properties predicted at higher Si contents. The commercial compositional ranges then provide significantly improved magnetic properties without endangering the workability beyond the capabilities of plane strain rolling deformation.

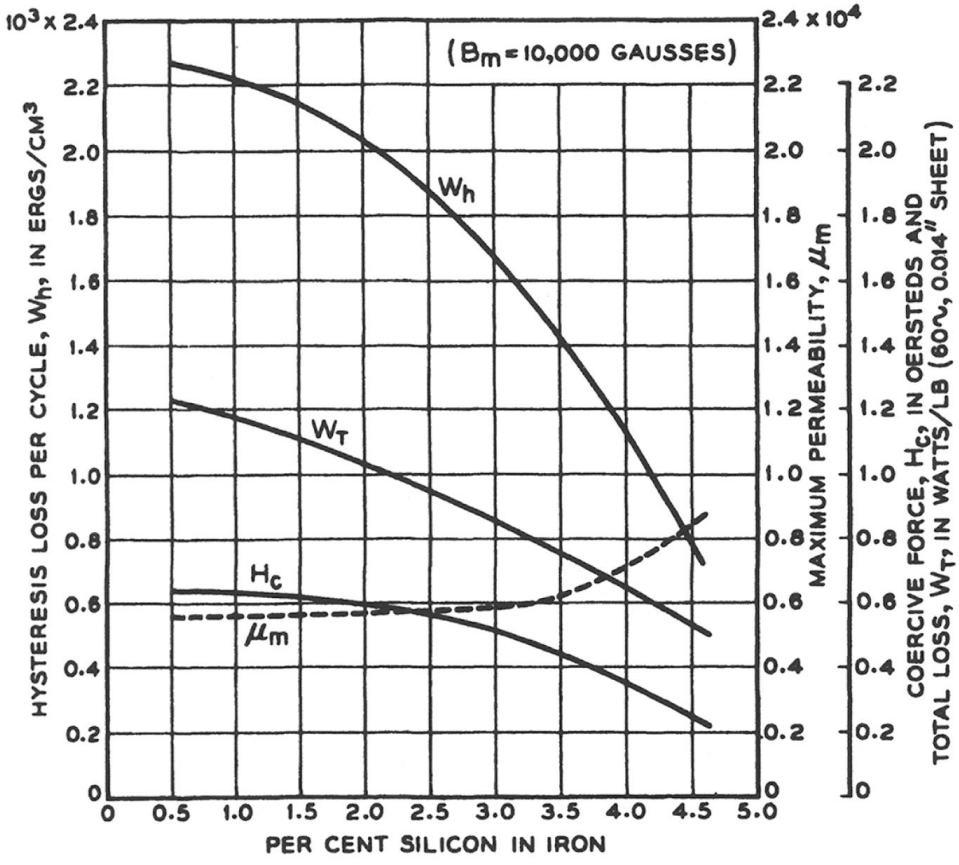

Figure 2-5 – Various magnetic properties as a function of Si content. Energy loss and coercivity decrease while permeability increase with increasing Si content. Note, some of the property improvements are also a result of using higher annealing temperatures (after [17], with permission of Wiley).

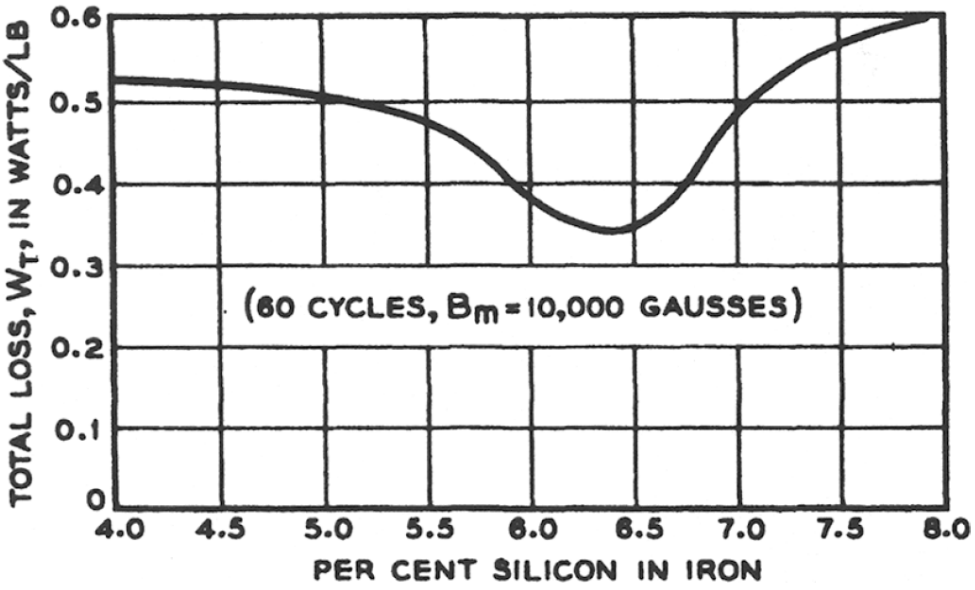

Figure 2-6 – Graph of total loss vs. silicon content (wt%), illustrating the minimum at 6.5wt%Si (12.14at%Si) (after [17], with permission of Wiley).

Silicon also has noteworthy effects on the microstructure of pure Fe. Most importantly, for electromagnetic applications, Si is known as an α-ferrite stabilizer and at 3wt%Si (5.79at%Si) allows for higher temperature processing (i.e., hot rolling, annealing) to be performed without an undesired phase change from the two phase γ-loop, see Figure 2-7.[25] Microstructurally speaking, avoiding the phase change during processing is particularly important for developing highly textured Fe-Si sheets, since phase changes are known to destroy texture development.[12] Additionally, the higher processing temperatures allow for a larger grain size to be developed in the final sheets while eliminating the possibility of retaining the non-magnetic γ phase, both of which render improved magnetic properties.

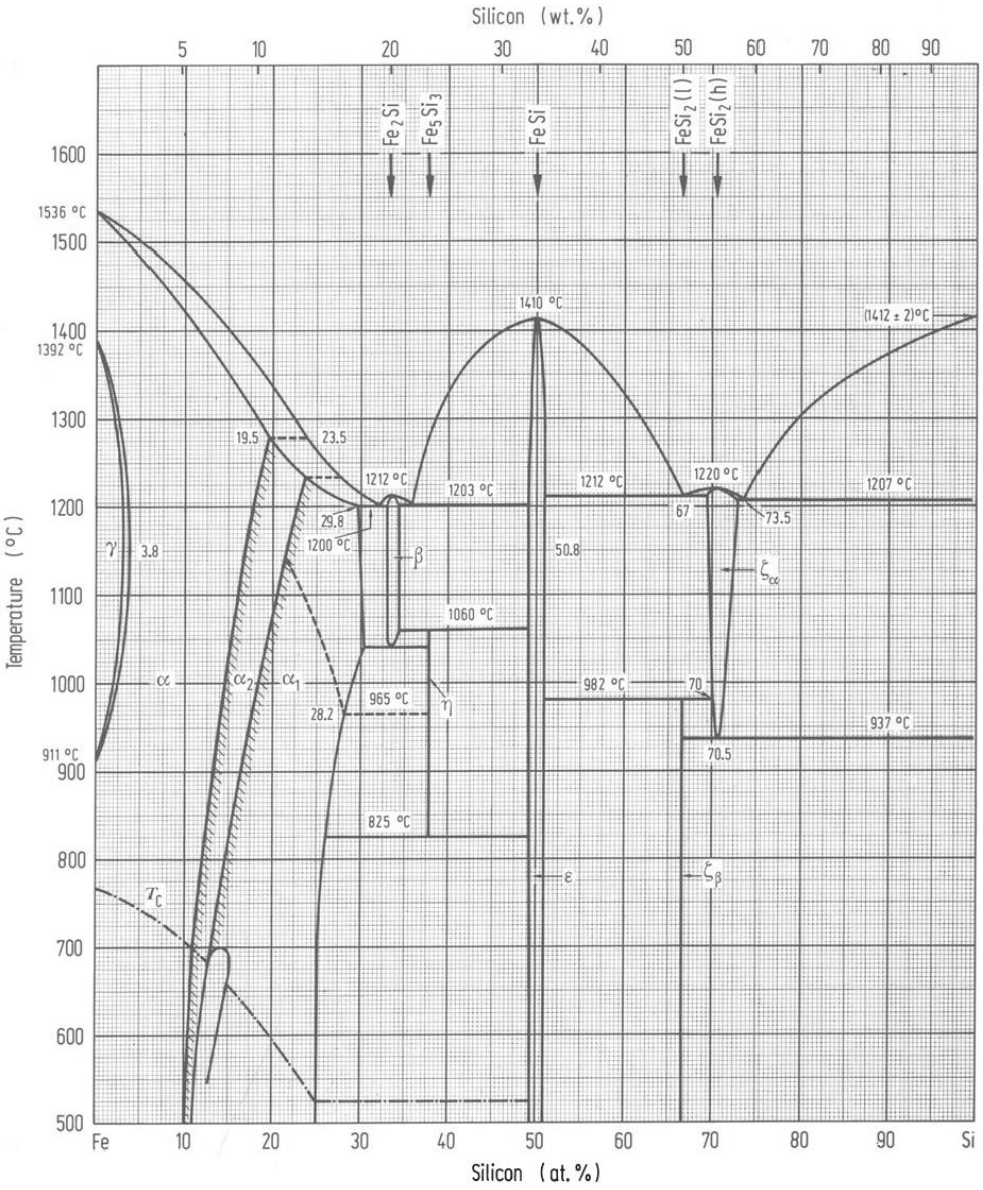

Figure 2-7 – Complete Fe-Si binary phase diagram. Note the evolution from a traditional BCC (α) structure to the B2 (α_2) and DO3 (α_3) structures with increasing Si content. When suitably low in C and with enough Si, the gamma loop can be avoided in Fe-Si alloys during high temperature processing and annealing. The onset of ordering greatly reduces workability in Fe-Si alloys (after [25], with permission of Springer).

In addition to Si, the basic ingot metallurgy must also consider the purity of the alloy, where the reduction of metallurgical impurities is essential for optimizing the final sheet

properties. Generally, both interstitial and substitutional impurities influence the magnetic properties of ferromagnetic materials. However, interstitial impurities have mostly been documented at having negative effects on magnetic properties, where the elastic strains in the alloy lattice from the interstitial element disturb the motion of magnetic domains, making the magnetization process more difficult. Properties such as permeability and coercivity are negatively impacted as a result. This is an important distinction from the substitutional solid-solution impurities like Si and Al, which are known to improve upon these same properties. Furthermore, some impurities can precipitate out and create so-called 'magnetic aging' issues, i.e., a deterioration of properties as a function of time. For Fe-Si alloys in particular, it is most critical to minimize the extent of carbon, sulfur, nitrogen and oxygen impurities.[1] Carbon is particularly important because, in addition to being an interstitial element, small amounts significantly increase the critical silicon composition required to maintain the desired single α phase microstructure at elevated temperatures due to a widening of the γ-loop.[26] Furthermore, C can cause precipitation of both Fe_3C particles and pearlite, the former of which effectively ages the alloy and reduces the long-term efficiency of the Fe-Si sheets.[1,27] Therefore, C both in and out of solution with Fe tends to reduce the magnetic performance.

Reduced magnetic properties can also occur with the aforementioned interstitial elements. In the case for sulfur, due to the limited solubility in iron (< 0.001 wt% at room temperature), sulfides can precipitate out and effectively block the motion of domain walls.[28] Similar oxide and nitride inclusions can also have negative effects at low concentrations.[28,29] Therefore, the goal is to develop metallurgically 'clean' Fe-Si

alloys for optimized properties. This is usually done through sophisticated annealing treatments in reducing atmospheres. Final sheet compositions from commercial manufactures typically contain <0.003wt%C and S.

2.4 Flat Rolled Sheet Products

By far the most commonly used form of the Fe-Si alloy today in electromagnetic applications is as flat rolled sheet. Two types of Fe-Si sheet are produced by commercial manufacturers and are classified based on the structure (crystallographic texture and grain size) and corresponding magnetic properties. The processing and attributes of each are summarized below with comparisons to the 'ideal' Fe-Si structure.

2.4.1 Non-Grain-Oriented Sheets

Early on, Fe-Si sheets were processed primarily by hot rolling.[4] Hot rolled sheets, which now receive some small amounts of cold rolling for improved surface quality, develop microstructures with nearly random crystallographic textures and are classified as non-grain-oriented (NGO) (Figure 2-8). While nearly random, the texture that does develop is not perfectly random and is characterized by some type of weak rolling texture, which in turn has been found to have some subtle effects on the magnetic properties. Optimum properties in NGO sheet have generally been observed by maximizing the volume fraction of the so-called η-fiber, defined by <100> crystallographic directions parallel to the normal direction (ND), while minimizing the γ-fiber, defined as the <111> directions parallel to the ND.[30–32] Commercially, this is accomplished by controlling both the rolling reductions and temperatures during processing. These sheets are then sold based on both

final thickness and core loss, which is mostly controlled by the composition and final microstructural state, with both semi and fully processed (i.e., annealed) conditions available. Due to the relatively weak texture, properties are also quite isotropic. Typical applications for the NGO sheets do not require the magnetic flux *H* to be applied in any specified direction, making NGO Fe-Si most useful in applications like rotating electric motors. Since NGO sheets are primarily hot rolled, products can have a slightly extended compositional range up to 4wt%Si (7.65at%Si) from the extended workability afforded by high rolling temperatures during hot rolling. Additionally, some versions of the NGO sheet include Al with Si to achieve a similar total reduction in core loss with slight improvements in overall workability. Generally, increased Si/Al content is beneficial for both permeability and core loss.[33]

2.4.2 Grain-Oriented Sheets

Substantial amounts of cold rolling were not introduced until the 1930s, however this processing modification has had remarkable effects on the Fe-Si sheet microstructure and properties. The persistent use of cold rolling, in combination with precise annealing treatments, introduces a well-aligned crystallographic texture in Fe-Si sheet consisting of the so-called Goss (or cube-on-edge) orientation. This orientation, named after Norman P. Goss who first described the processing methodology needed to achieve the texture in 1935, is defined by the {110} crystallographic planes aligned with the sheet surface and the <001> crystallographic directions aligned with the sheet length (parallel to the rolling direction, RD) (Figure 2-8).[16] Typical cold-rolled Fe-Si sheets can be processed to develop an extremely strong Goss texture and are sold as so-called grain-oriented (GO)

sheets. The principle advantage of having the Goss orientation comes from the high magnetic permeability unique to this texture. In particular, the easy magnetization <001> crystallographic direction, discussed in Section 1, is aligned with the RD. Consequentially, the GO sheets are utilized in transformer applications where the magnetic flux *H* is applied parallel to the RD of the sheets in the transformer core.

To achieve this strong Goss texture, a complex, multi-step rolling and annealing schedule is used, which involves hot rolling, cold rolling with intermediate annealing, decarburization and a final high temperature anneal. Specific details of GO sheet processing are typically kept proprietary, however; a general processing skeleton has been well established in the literature.[26] First, ingots are cast and subjected to several passes of hot rolling at high temperatures (> 1000°C). For each hot rolling pass, large reductions are used to significantly reduce the ingot thickness while simultaneously convert the cast microstructure to a wrought equiaxed grain morphology. Multiple rounds of hot rolling are performed until the final desired sheet thickness is reached (thickness ~ 2 mm). The resultant hot rolled plate possesses a coarse equiaxed grain microstructure. At this stage, texture analysis near the surface of the plate typically reveals the Goss orientation, which is believed to form as a result of constrained shear deformation during the hot rolling.[34]

Following hot rolling, the plate is pickled to remove any oxide that developed and is then further reduced by multiple cold rolling passes. Due to the limited workability of the Fe-Si, intermediate annealing is performed between each of the cold rolling rounds so as to avoid excessive work-hardening and prevent fracture. Each cold rolling round is restricted to below 85% reduction to avoid destruction of the critical Goss nuclei created

during hot rolling. Cold rolling is performed until a thin sheet remains with a nominal thickness of 0.3 mm. A decarburization treatment is then used to further reduce the carbon content for improved magnetic properties and reduce the width of the γ-loop.

The final step is a long (> 24 hrs.), high temperature (> 1100 °C) anneal in a reducing atmosphere that activates an abnormal grain growth (secondary recrystallization) mechanism, which is ultimately responsible for developing large grains (d > 1 mm) with a sharp final Goss orientation. Textures are so sharp that grains fall within 3° from the ideal Goss. The governing mechanisms behind this abnormal growth are still not fully understood and has been the subject of a longstanding scientific debate.[35–37] Further sheet processing may be performed to reduce any residual stresses from shearing and/or handling processes. The final commercial GO sheets are then characterized by a coarse grain microstructure with a well aligned, high permeability texture possessing a high degree of magnetic anisotropy. It is significant to note that compositions of the GO sheet are generally restricted to 3wt% Si due to the use of cold rolling.

2.5 Commercial Sheets vs. Ideal Fe-Si

While these two products have found important commercial applications, neither the NGO nor the GO sheets are considered ideal in terms of maximizing magnetic properties for Fe-Si. A “perfect” magnetic structure would take advantage of the easy <001> directions in a dispersed or isotropic distribution throughout the sheet. Theoretically, this is characteristic of cube-type textures, defined by {100}<uvw>. Such textures possess the

<001> directions in the plane of the sheet and therefore maximize permeability while minimizing core loss and coercivity for a given Fe-Si composition. [32,33,38,39]

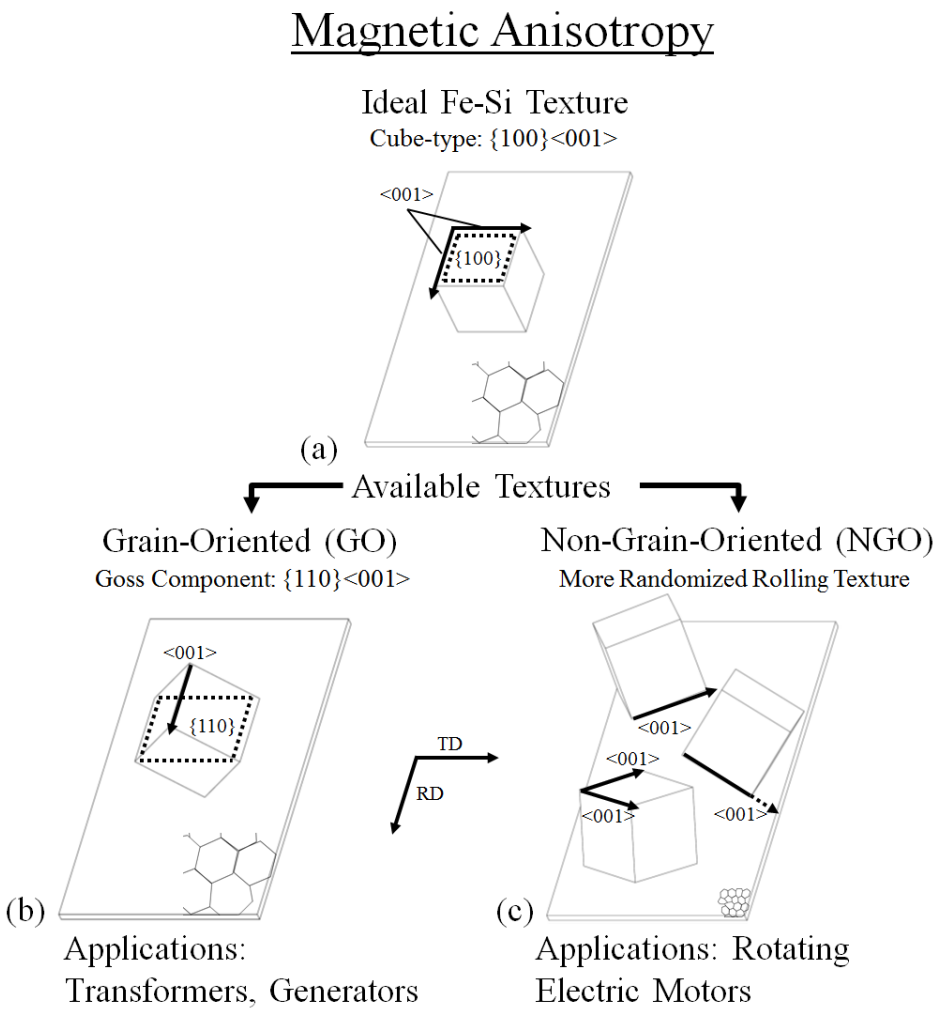

Figure 2-8 – Structural comparison of the truly 'ideal' Fe-Si sheet with the two available commercial sheets. The ideal form is characterized by a cube-type crystallographic texture, containing <001> directions in the sheet plane. GO sheets, characterized by the Goss texture, are nearly idealized along the RD, while the NGO sheets have a nearly random distribution of <001> directions.

Clearly differences are found between the commercial sheets and the ideal cube textures of Fe-Si sheet in terms of the orientation of the <001> directions. In case of the

NGO sheets, the weak rolling textures produce a nearly randomized orientation of the <001> directions both in and out of the sheet plane. Such a distribution of <001> directions is significantly less efficient than the ideal structure, but also produces significant isotropy. Furthermore, NGO sheets do not usually possess extremely large grain sizes ($d \sim 150\ \mu$m) because normal grain growth mechanisms are operative during annealing processes of fully processed sheets. Since grains are known to act as barriers to domain wall motion (Section 1), the ideal case would contain larger grains ($d \sim$ millimeters). Comparatively, the GO sheets possess a strong texture with one of the <001> directions along the sheet length, giving the ideal magnetic properties in that direction. Fundamentally, transformers take advantage of this unique orientation, however, even slight deviations in the texture orientation or in the alignment of the applied field can drastically reduce the performance. Consequentially, the GO sheets are significantly worse than the NGO for rotating motor applications. Furthermore, properties also plummet at the corners of transformer cores where the flux no longer lies parallel to the sheet length, causing increased energy loss locally. Additionally, due to the abnormal grain growth mechanisms that result in the Goss texture, grain sizes of the GO sheets are near ideal.

2.6 Workability Issues in Fe-Si

While the addition of Si improves several intrinsic magnetic properties of Fe, it also negatively affects the mechanical workability. Commercial rolled sheets are generally restricted to around 3.5wt%Si (6.73at%Si) as an upper bound, despite predicted improvements in magnetic properties at higher Si compositions up to the ideal 6.5wt%Si (12.14at%Si). Limitations in workability of Fe-Si alloys with higher Si contents have been

attributed to a transition in microstructural (atomic) ordering.[18,40] While disagreements exist regarding the specific nature of atomic ordering in Fe-Si, it is worth briefly discussing. At lower Si compositions (< 5wt%), the microstructure is believed to only possess short range order. However, even at the lower compositions, the addition of Si has been noted to significantly increase the critical twinning transition temperature, which is often associated with brittle facture.[41,42] Consequentially higher temperatures must be used to avoid the twinning deformation in favor of slip. At high Si compositions (>5wt%), the microstructure begins to develop long-range order, first with a B2 (α_2 on Figure 2-7) type structure and eventually a DO3 (α_1 on Figure 2-7) atomic arrangement. Deformation for the ordered Fe-Si alloys is governed by the motion of superlattice dislocations (both imperfect and perfect) followed by the nucleation of antiphase boundaries, which leads to severe workability reductions compared to traditional slip.[18] Efforts to minimize these effects at the high Si compositions have generally been restricted to using annealing treatments to alter the behavior of the ordering, but have largely been ineffective.[43] It is important to note that in the present, no effort was made to minimize or control the degree of microstructural ordering in the 6.5wt%Si casting. Experiments were conducted directly on the as-cast ingot.

In summary, the fundamentals of ferromagnetic materials were discussed with emphasis on Fe-Si alloys and the basic rules for improving magnetic properties were outlined in relation to the intrinsic magnetic domain structure. A brief history of Fe-Si development was given and notable historical achievements were described. Critical metallurgical aspects controlling the magnetic properties of Fe-Si were disclosed with respect to alloy composition, structure and processing. Details of the two NGO and GO Fe-

Si commercial sheets were discussed and compared with the theoretically ‘ideal’ Fe-Si sheet. Finally, workability issues were briefly mentioned. This background identified many limitations of commercial sheet rolling in developing optimized Fe-Si sheets for electromagnetic applications, both in terms of composition and structure. Subsequent chapters detail the use of simple shear deformation *via* machining to produce thin, continuous Fe-Si strips from higher Si contents and with greater texture and microstructure control when compared to rolling.

CHAPTER 3. FUNDAMENTALS OF MACHINING

This chapter is devoted to the mechanics of simple shear deformation through machining. As a model deformation technique, the discussion is centered around the hybrid-cutting extrusion process of large strain extrusion machining (LSEM). Analytical models detailing expressions to define deformation strain, temperature, hydrostatic pressure and strain path are presented. Note, rigorous derivation of the models have been presented in previous work and are left out here.[44,45] Finally, a brief comparison between the simple shear deformation of machining and plane-strain compression of rolling is given.

3.1 Simple Shear Deformation by Machining

The fundamentals of simple shear deformation *via* machining are well described by large strain extrusion machining (LSEM). Figure 3-1 shows the rotary configuration of LSEM in which a sharp, wedge-shaped cutting tool, engaging at a preset depth (t_o) with a workpiece (WP) rotating at constant surface velocity (V_o), produces a chip of pre-defined geometry. As material is removed, the top surface of the chip (free surface in conventional machining) is constrained by a second tool (constraint), that defines the chip geometry, in the present case a sheet of thickness t_c. The extent of constraint is defined *via* the chip thickness ratio, defined as $\lambda = t_c/t_o$, which is a controlled *a priori*. During cutting, sheet forms by intense, local shear deformation within a narrow deformation zone (of thickness,

$\Delta \sim 100$ μm). Due to the narrow width of the deformation zone, and the high surface velocities, high strain rates of $\sim 10^3$ s^{-1} are common during LSEM. Furthermore, confinement of deformation by application of the constraint suppresses the tendency to develop a segmented or flow-localized chip while promoting formation of continuous sheet with homogeneous microstructures.[46] This confinement, coupled with the strain rates, results in significant temperature rise in the sheet during its formation due to deformation-induced heating (near-adiabatic). Such temperature rises can have marked effects on the sheet microstructure due to dynamic recovery, dynamic recrystallization and adiabatic shear banding, similar to other high-rate deformation processes.[47,48]

The deformation path can also be varied, by controlling the tool rake angle (α) and λ, thereby enabling various shear textures in the sheet not achievable in rolling.[10,49,50] The λ and α parameters also affect the hydrostatic pressure in the deformation zone, a key parameter influencing workability in deformation processing. Overall, the process is best visualized as simultaneous cutting-extrusion, effectively transforming the conventional chip formation into a shear deformation process for producing sheet with fine-grained microstructures by utilizing large strains. The large strains and hydrostatic pressures, high deformation temperatures and deformation path control make LSEM an ideal thermomechanical processing method for producing sheet from metals of limited workability with high crystallographic anisotropy, such as Fe-Si.[51,52]

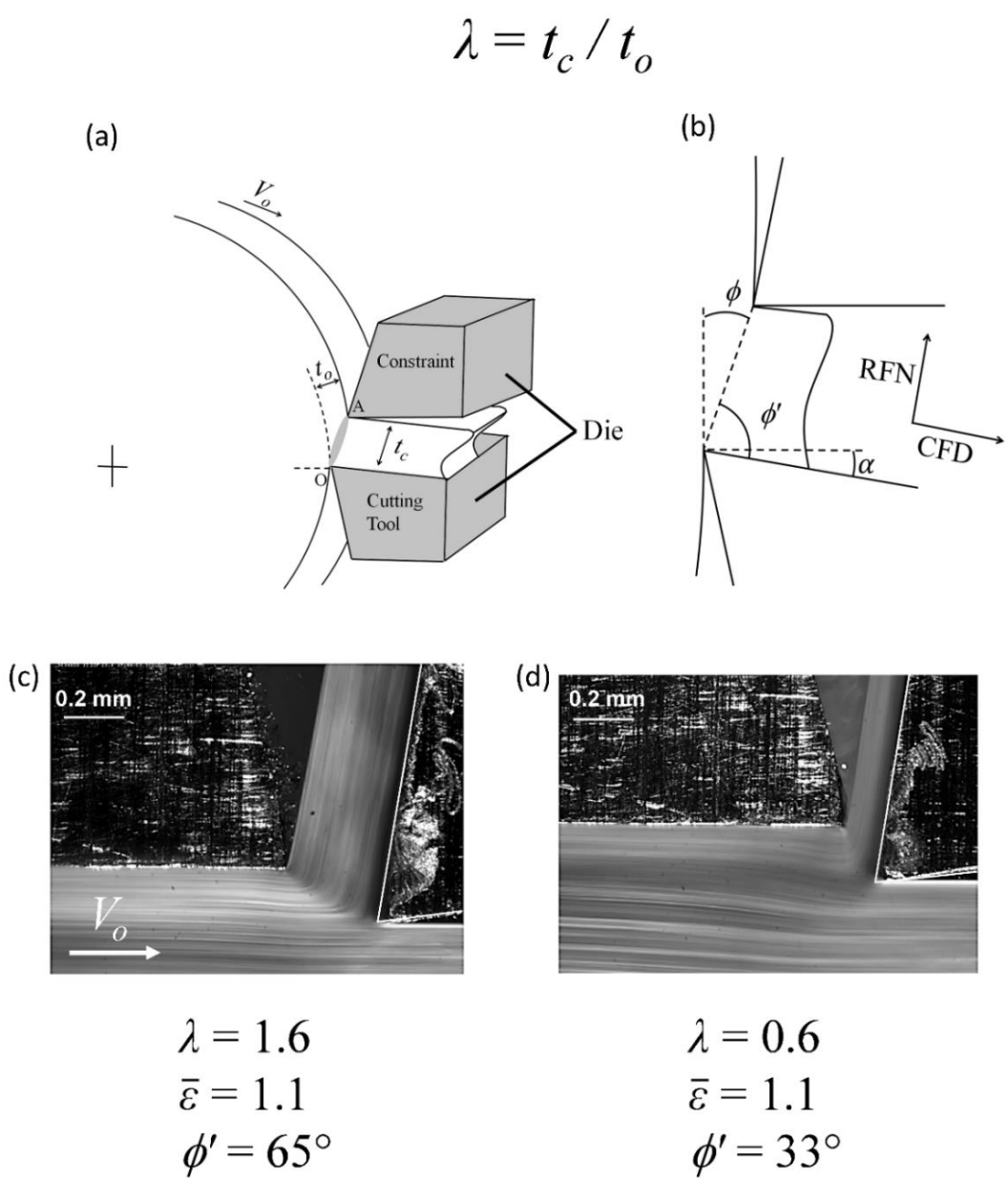

Figure 3-1 – Simple shear deformation by LSEM: (a) Schematic of rotary LSEM configuration with inset (b) showing relevant geometric parameters. (c) and (d) show material flow at λ of 1.6 and 0.6, respectively, obtained by averaging 200 consecutive images from a high-speed video recording; lead workpiece, α = 10°, and V_o = 0.4 mm/s.

3.1.1 Deformation Strain and Hydrostatic Pressure

Based on the idealization of the deformation zone as a single shear plane (Figure 3-1), the effective (von Mises) strain imposed in the sheet can be determined using upper bound analysis methods and is given by:-

$$\bar{\varepsilon} = \frac{1}{\sqrt{3}}\left(\frac{\lambda}{\cos\alpha} + \frac{1}{\lambda\cos\alpha} - 2\tan\alpha\right) \tag{3-1}$$

Large strains (> 1) can be imposed during machining by controlling both the λ and α parameters to produce sheet with deformation structures characterized by ultrafine grains (UFGs). In conventional machining, only α can be modified since chips produced develop λ values that coincide with the intrinsic material flow response to a given temperature and strain rate. Conversely, LSEM controls λ through the constraint to access larger ranges of deformation strain at correspondingly different deformation paths, both of which control microstructures and textures. Consequentially, LSEM is used to produce sheets with lower final thickness (t_c) than in conventional machining. Furthermore, the constraint allows for λ values to be lower than 1, which has marked effects on the hydrostatic pressure. The hydrostatic pressure can be determined from analysis of slip line fields along the deformation zone width. A maximum hydrostatic pressure (p) is reached at the entry of the deformation zone, the value of which is defined by:

$$\frac{\rho}{k} = 1 + 4\tan^{-1}\left(\frac{1}{2\theta}\right) \tag{3-2}$$

where k is the material shear strength and θ is a function of λ and α.[45] The hydrostatic pressure increases (monotonically) with decreasing λ, reaching a maximum value of ~ 4k

(k is the material shear strength) at λ = 0.5. In contrast, in plane strain rolling, the hydrostatic pressure is fixed at ~ k. Since hydrostatic pressures are known to enhance workability during metalworking, alloys of poor workability like Fe-Si are less susceptible to cracking and fracture in LSEM than in rolling. Strain and (normalized) hydrostatic pressure are plotted in Figure 3-2 against λ for α = 5°.

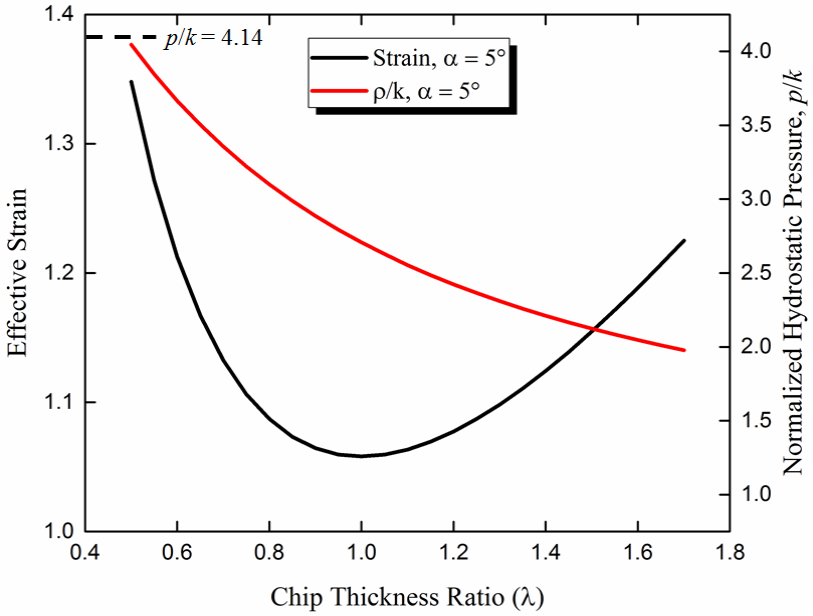

Figure 3-2 – Strain and (normalized) hydrostatic pressure plotted against the chip thickness ratio. Strain reaches a minimum at λ = 1 and increases with increasing or decreasing λ. Hydrostatic pressure, essential in extending the workability of metals, sharply increases with decreasing λ. Note, hydrostatic pressure in rolling is confined to k.

3.1.2 Deformation Path Control

Of particular importance to crystallographic texture development is the deformation path, which has been extensively characterized in machining and is determined by the strain rate tensor and strain.[50] Such measurements are gathered by tracking the

displacements of material elements traveling through the deformation zone. An example of this *in-situ* tracking is shown in Figure 3-3, where a series of images were gathered from linear cutting experiments and analyzed by tracking surface asperities using particle image velocimetry (PIV). Information about the strain rate tensor, strain fields and shear directions, characterizing the deformation, can be gathered for material traveling along pathline abcd.[54] Three λ values, ranging from totally unconstrained (free) to 1 (i.e., $t_o = t_c$), are shown to fully capture the λ range accessible for Fe-Si. In the example, the workpiece was lead and cutting tool with $\alpha = 10°$ was used. References axes are defined by CFD and RFN, with transverse direction (TD) out of the page. The top row shows high speed images of the material flow for the three deformation conditions with the corresponding strain rate fields for material traveling along pathline abcd. The velocity gradient and corresponding shear directions are also shown for point c for the respective pathlines. Of particular interest is the effect of λ on the shear direction. At a large unconstrained λ of 2.5, i.e., free (conventional) machining, deformation is well described by a single shear plane with a shear direction oriented at 79° relative to the CFD. As λ decreases, a secondary shear zone isolated near the material-tool interface becomes more significant and the shear direction exhibits a clockwise rotation about the TD towards the CFD. In the example, the smallest $\lambda = 1$ resulted in a shear direction of 47°. Such rotations of the shear direction continue as λ decreases with a steadily increasing contribution from the secondary shear zone.

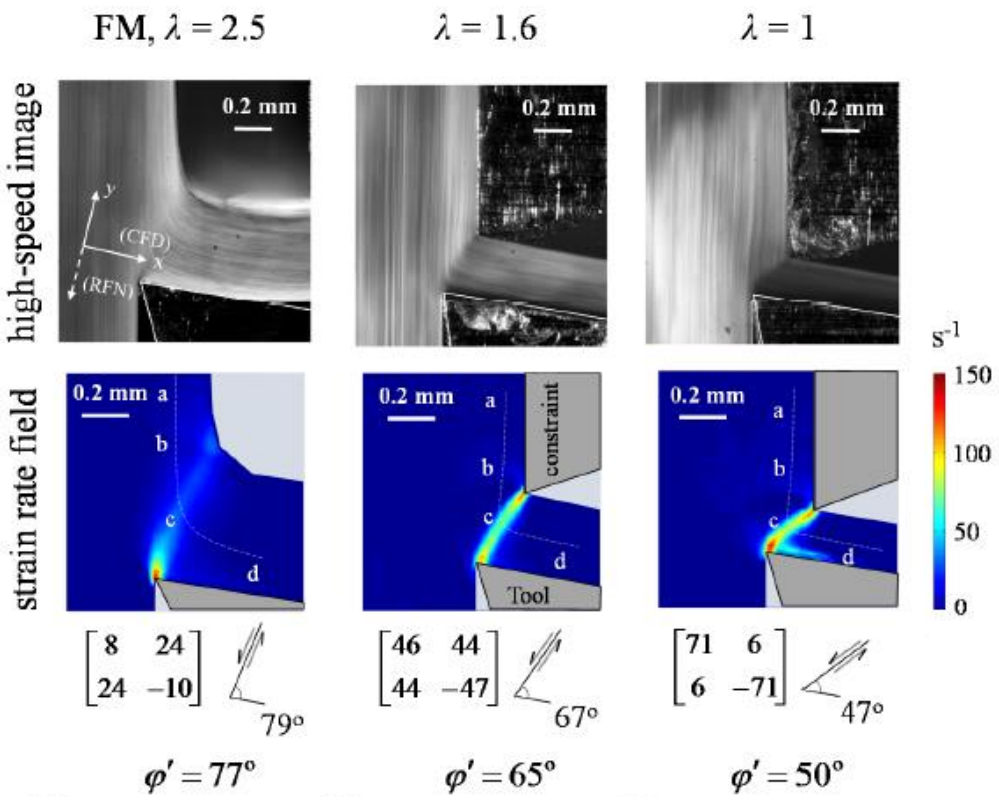

Figure 3-3 – PIV analysis of simple shear deformation through machining. The top row shows high speed images of material flow for the three deformation conditions. Resultant strain rate fields are shown in the bottom row detailing material flow along pathline abcd. Strain rate tensor and shear direction for point c of pathline abcd is also provided (after [54], with permission of Elsevier).

With suitably large λ values, PIV analysis has shown that analytical expressions, obtained from a single shear plane model, for both strain (Equation 3.1) and deformation path correspond closely with measurements. This agreement is robust until very small λ values (< 0.6) are used. Values of λ have been limited to ~1 at the lower bound in this study. Hence, expressions for $\bar{\varepsilon}$ and ϕ' are used in the present to analyze sheet microstructure and texture in Fe-Si, where ϕ' is described by the inclination (orientation) of the shear plane

(measured counterclockwise from the CFD) with respect to the sheet surface (Figure 3-1) by:

$$\phi' = 90° + \alpha - \phi \tag{3-3}$$

where $\phi = \tan^{-1}(\cos\alpha/(\lambda - \sin\alpha))$.[50] Since ϕ', like $\bar{\varepsilon}$, is also a function of both α and λ, the deformation conditions can be selected to produce varied shear plane angle orientations, and therefore deformation textures. Another example of this type of control is also provided in Figure 3-1, where, when λ is varied from 1.6 to 0.6, the measured ϕ' experiences a change of 32° while the strain in the sheet is nominally the same ($\bar{\varepsilon}$ = 1.1). The material flow during the shear is revealed by high-speed imaging, see bottom row of Figure 3-1.[54] Sheet can then be created under similar strains, but with widely different shear plane orientations and therefore textures. Alternatively, a range of strains can also be imposed by varying λ, and to a lesser extent also by α. At small λ, the sheet thickness can be made even smaller than t_o, unlike in conventional (free) machining.

3.1.3 Temperature

Due to the high strain rates and large strains localized within the narrow deformation zone, large deformation temperatures can be achieved during cutting. The total deformation zone temperature (T) can be estimated using a heat-source analysis based on a shear plane model for the deformation as:[50]

$$T = u_s \frac{(1-\Gamma)}{\rho c} + T_o \tag{3-4}$$

where T_o is initial WP temperature, u_s is the shear energy per unit volume dissipated at the shear plane during chip formation (determined by the ratio of the cutting force to the strip cross-sectional area), ρ is the density, c is the specific heat capacity and Γ is the fraction of heat generated at the shear plane that enters the WP. The expression for Γ has been published previously[44,53,55]; it is a function of the chip geometry, thermophysical properties of the material, the cutting velocity (V_o) and λ. Equation 3.4 is used to estimate T in the present (using thermophysical property data for pure iron) for interpreting thermoplastic phenomena. Some of the experiments also involve pre-heating of the WP, i.e., varying T_o. Previously, observations have shown that deformation temperatures increase with increasing V_o (at constant λ and α) and decreasing λ (at constant V_o).[55] Further increases are also possible when the workpiece is preheated prior to deformation (T_o > 25°C). An example plot showing the dependence of T on V_o for LSEM Fe-Si are shown in Figure 3-4. Note, the deformation temperature was found to increase by ~ 110° (370°C to 480°C) by increasing V_o from 1 m/s to 5 m/s, in agreement with previous work on Mg. Temperatures as large as 830°C were obtained in the study through combinations of V_o and T_o, which have drastic effects on the microstructure.

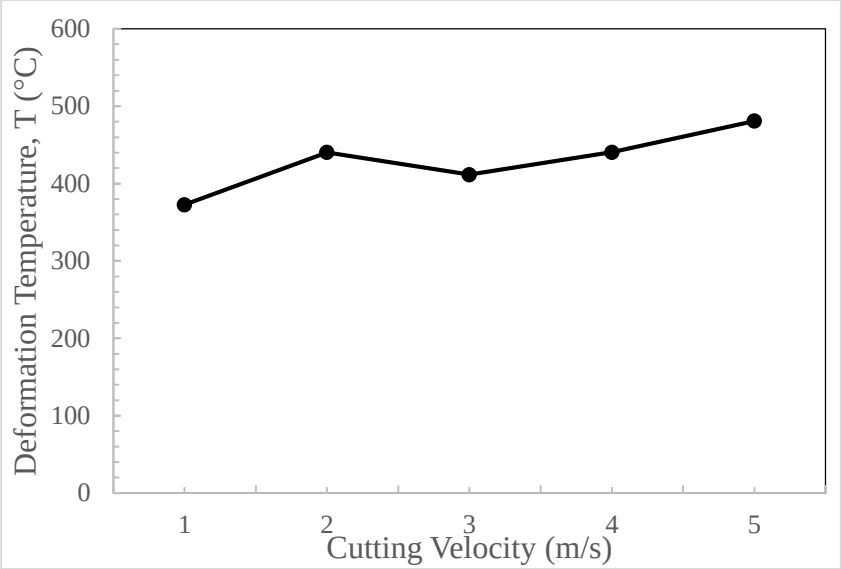

Figure 3-4 – Deformation temperature, T, as a function of cutting velocity, V_o. In agreement with previous work in Mg, deformation temperature generally increases with higher cutting velocity. Here, $\lambda = 1.2$, $T_o = 25°C$ and $\alpha = 5°$.

Taken as a whole, simple shear deformation through machining allows for significant deformation control to produce sheets from uniquely large strains and hydrostatic pressures, varied deformation paths, and high deformation temperatures. A systematic evaluation of these deformation parameters are explored on select Fe-Si alloys to characterize the metallurgical response in terms of microstructure, texture and magnetic properties.

CHAPTER 4. EXPERIMENTAL

4.1 Workpiece Materials

Sheet samples for texture and microstructure analysis were produced by combinations of unconstrained (free) and constrained (LSEM) machining from two Fe-Si alloys. One was a nominal Fe-4 wt%Si (7.65at%Si) plate (wt.%: 3.83Si, 0.32Mn, 0.028C, 0.018P, 0.015S, 0.006Al, balance Fe) supplied by Scientific Alloys, Inc., Westerly, RI in the form of a hot-rolled plate. The as-received hot-rolled plate was 0.67 cm thick with a coarse, equiaxed grain size of d ~ 1 mm (Fig. 2a). The large initial grain size and the higher than usual Si content should be expected to reduce the workability of this alloy relative to the conventional (3 wt% Si) electrical sheet steel. Hence, it is not surprising that in free machining the chip from this Fe-4 wt% Si exhibits inhomogeneous, shear flow localized deformation.

To address this localization issue, a section of the hot-rolled plate was subjected to a warm-rolling at T_o ~ 573 K (300°C) reduction of 60%, followed by annealing at 973 K (700°C) for 30 min in air in a box furnace. This processing resulted in a WP structure (Fig. 2b) with a fine, equiaxed grain size of ~ 20 μm and nominal hardness of 230 HV. The fine grain size allowed for several grains to be encompassed in the machining deformation zone (i.e., t_o), resulting in more homogeneous deformation and reduced flow localization (Fig. 2d). Hence, the 4 wt%Si WP used in the various cutting experiments was a 10-cm diameter

disk of thickness 0.25 cm, cut out from the fine-grained plate. The sheet width produced by machining under plane-strain conditions was thus equal to the disk thickness.

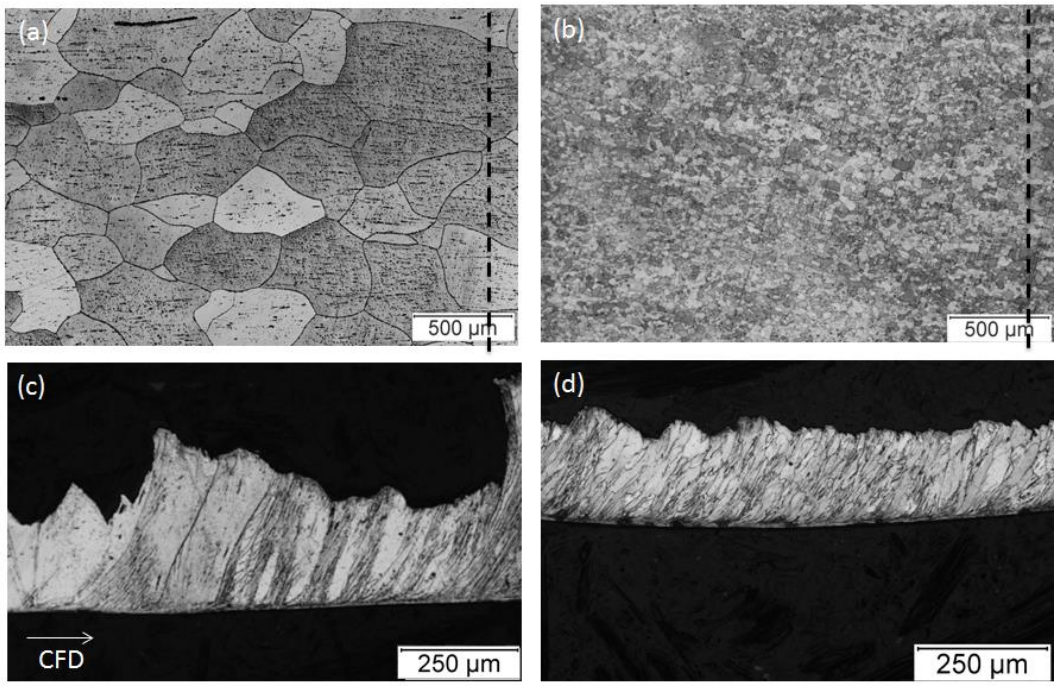

Figure 4-1 – Optical micrographs showing the starting workpiece microstructure of (a) coarse-grained Fe-4 wt% Si plate produced by hot rolling (as-received) and (b) fine-grained plate produced by warm rolling and annealing. (c) and (d) show the thickness cross-section of the chips (t_o = 0.13 mm, α = 0°, and V_o = 2 m/s) produced from the corresponding workpiece materials. The black dotted lines represents t_o (i.e., depth of material removed in each pass).

The second WP material was at the ideal Fe-6.5wt%Si (12.14at%Si) composition in an as-cast form. The ingot was cast in the form of a cylinder using a vacuum induction melter backfilled with Ar-5% H_2 at 1 atm. Various castings were produced from electrolytic Fe and interstitial free (IF) steel with semiconductor Si, which were melted in an alumina crucible poured into a copper mold (cavity 3 cm diameter x 7.5 cm tall) set atop a water-chilled platform within the furnace. The resulting ingot exhibited a coarse,

equiaxed grain structure with limited microporosity. The ingot was then turned down to 2.5 cm diameter.

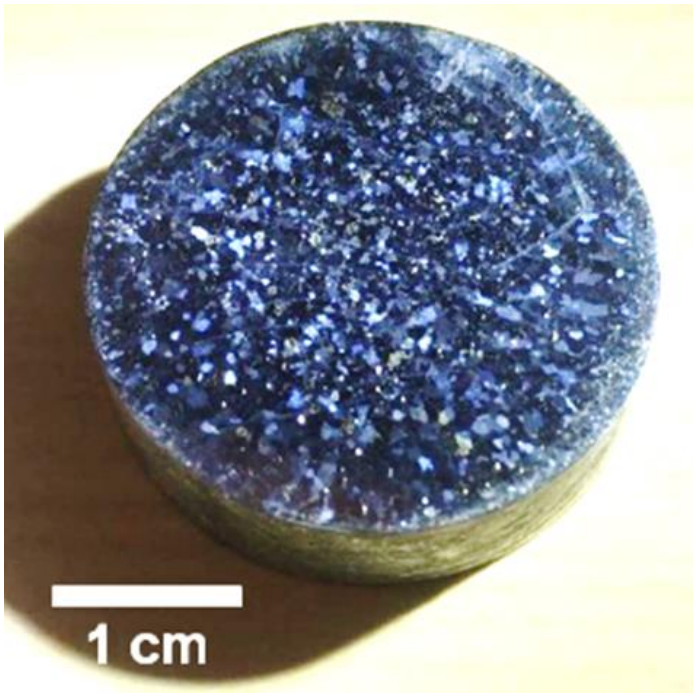

Figure 4-2 – As-cast Fe-6.5wt%Si ingot cross-section. A coarse (d ~ 500 μm), equiaxed grain size developed during solidification. No macro pores were found in the casting and only very minor microporosity.

4.2 Deformation Conditions

A series of experiments was carried out on both high-Si alloys to produce sheet by simple shear (Fig. 1) under different ranges of conditions – λ (0.7 – 2), α (0° – 20°), T_o (298K (25°C) – 573K (300°C)) and V_o (0.25 m/s – 5 m/s) – in order to analyze texture and microstructure development. The deformation path was varied by adjusting λ and α. Plane-strain deformation was ensured by keeping the sheet width at least 10 times t_o. Cemented

WC inserts were used as the cutting and constraining tools. The strain imposed in the deformation zone was estimated using Eq. (3.1) and it is this strain that is reported.

4.3 Microstructural Characterization

Texture and microstructure in the sheet samples were characterized in as-deformed and recrystallized conditions. Microstructure analysis involved optical microscopy of the sheet thickness cross-section, with axes defined by the rake face normal (RFN, thickness) and chip flow direction (CFD, length), see Fig. 1. The samples were mounted and ground with 320 to 1200 grit SiC abrasive paper, followed by final polishing with 0.05 μm alumina and 0.02 μm colloidal silica. 5% Nital (4 wt% Si alloy) and 25% hydrochloric acid (6.5 wt% Si) solutions were used as etchants (20-60 seconds with mechanical agitation) to reveal the microstructures. The structure was characterized in terms of grain size, flow patterns and defects.

Texture data from the sheet thickness cross-section were obtained using a field-emission scanning electron microscope (FEI XL40 Schottky FEG) and EDAX OIM software (Mahwah, NJ). Various EBSD scan sizes were used to encompass many grains during a single scan. Multiple scans were performed for each sample and then merged through the software to provide a large-area picture of sample texture. Data from the scans were only considered acceptable if points achieved confidence index values (CI) greater than 0.1, ensuring a minimum statistical certainty of 95% or higher for individual orientation pixels. Several hundred pixel points were sampled for each grain to obtain accurate grain orientations. No data cleanup, other than the CI filtering, was performed prior to generating pole figures and orientation distribution functions (ODF).

4.4 Texture Evolution Analysis

In an effort to explain the observed recrystallization texture evolution, incremental isothermal recrystallization experiments were conducted on the Fe-Si sheet specimens. For the study, two machining conditions, one LSEM and one conventional machining, were selected and the results were compared with a rolled condition. Slow speed machining conditions were used to minimize inhomogeneous recrystallization from shear flow localization. Thin rectangular samples were sectioned from each deformation condition and annealed in an open air box furnace at 600°C for different times. Samples were then removed from the furnace and air quenched (cooled). The rolled condition was deformed to a nominal strain typical of machining. Analysis of the fraction recrystallized was performed using Vickers (micro) hardness measurements along the bulk of the samples. For statistical analysis, 20 indents were performed on each annealing condition. Hardness data were used to generate JMAK plots from which Avrami exponents were extracted. Differences in the recrystallization behavior were then identified from both optical micrographs and the JMAK recrystallization parameters. Possible recrystallization differences are explained with respect to processing differences.

4.5 Magnetic Property Measurements

Magnetic properties were acquired courtesy of Magnet-Physics Inc. in Fishers, IN. Quasi-static hysteresis loops of single sheet specimens were measured using a closed-loop magnetic analysis from an IEC 60404-4 standard permeameter (Remagraph®C). Samples were lightly clamped into the measuring yoke and the polarization, *J* was measured using J-compensated surrounding coils. Magnetic properties, including maximum relative

permeability, coercivity, hysteresis loss and maximum induction were tabulated from the measured hysteresis loops. Sheet specimens with a minimum cross-sectional area of 0.3 mm^2 and lengths of 92 mm were analyzed. Prior to measurement, specimens were annealed at 700°C for 30-60 minutes using an open air box furnace. Oxide scale was removed from the sheet surfaces using fine 600-800 grit SiC paper followed by a final pickling in a 1:5 nitric acid-ethanol solution for 3-5 minutes with light mechanical agitation. The pickling further removed oxide while reducing residual stored energy from deformation of the mechanical polishing. Commercial NGO and GO standards were also assessed, courtesy of AK Steel (Middletown, OH). Sections of bulk commercial sheets were gathered using a paper cutter and were given a manufacturer recommended stress relief anneal in a box furnace at 800°C for 5 min. Sample properties were gathered along the longitudinal direction, corresponding to the chip flow and rolling direction, respectively. Hysteresis loops were measured using an applied field, H of ±65kA/m at room temperature. The applied field was obtained using a C-shaped potential coil directly attached to the specimen surface. It is important to note that because the H field had finite limits, rather than quantifying a true induction saturation, a maximum induction is instead reported.

CHAPTER 5. RESULTS – MICROSTRUCTURE AND TEXTURE EVOLUTION

This chapter focuses on the microstructure and crystallographic texture evolution of the Fe-Si alloys following simple shear deformation *via* machining. Three main sections are discussed. Section 1 introduces the workability issues in Fe-Si alloys following conventional rolling deformation. Mechanical performance and deformation modes are discussed in detail to set the stage for comparisons with machining deformation. Section 2 presents processing-microstructure relationships in machined Fe-Si, highlighting both conventional and LSEM processes. Processing-microstructure maps are used to describe different metallurgical phenomena. The third section describes experimental crystallographic texture evolution, beginning with idealized simple shear textures in BCC crystals and concluding with measured deformation, recrystallization and grain growth textures. The fourth and final section provides a theoretical framework for the 'ideal' simple shear textures for electromagnetic applications.

5.1 Workability Issues in Rolling

As described throughout Chapter 2, Fe-Si alloys possess limited workability, which becomes pronounced with increasing Si content. To evaluate the workability of the alloys used here, a series of rolling experiments were conducted on the two Fe-Si compositions at various preheat temperatures. Preheating was achieved by placing the samples in an open air furnace prior to flat rolling. Once the desired temperature was reached, the sample was

removed and quickly subjected to a single rolling pass. Following the deformation, the sample was quickly placed back into the furnace to regain the desired temperature. Thermocouple measurements before and after deformation revealed that temperature drops were low, at most ~ 75°C for the highest rolling temperatures. Therefore, the rolling can be considered as pseudo-warm rolling process with negligible temperature drop, despite the rolls being cold. Reductions during each rolling pass were held constant at 10%. Single rolling passes were conducted until failure was observed, defined in the present context as through-thickness cracks that originate in the center of the sample or propagate from an edge into at least 1/3 of the sheet width. Fine edge cracking alone was not considered sheet failure, despite occurring in nearly all experiments. The results are summarized in Figure 5-1 where effective strain/rolling reduction at failure is plotted as a function of preheat temperature (both as-measured and homologous). For reference, strains to failure were considered large when $\bar{\varepsilon} \geq 1$ (dotted line on plot), corresponding to typical strains used in machining of the two alloys.

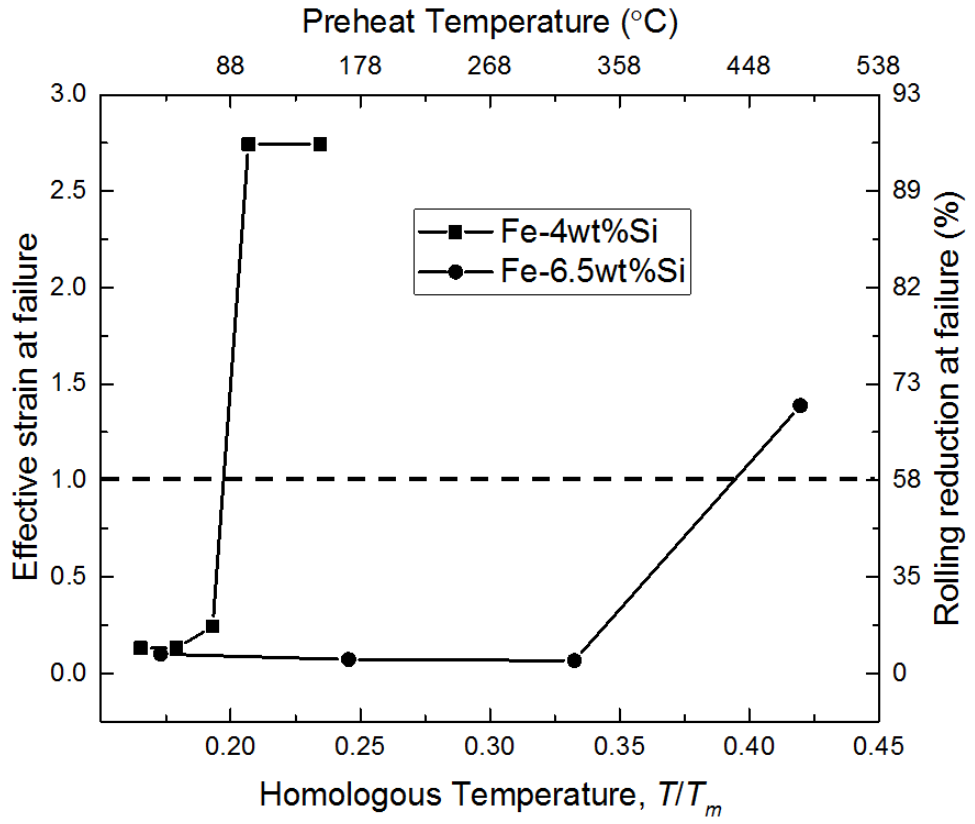

Figure 5-1 – Plot of effective strain and rolling reduction at failure as a function of workpiece preheat temperature (both as-measured and homologous) prior to rolling. Both alloys were essentially brittle when rolled under ambient conditions. The Fe-4wt%Si alloy exhibited a relatively narrow transition from ductile to brittle behavior at significantly lower temperatures than the 6.5wt%Si alloy.

The plot reveals information about the intrinsic workability of these Fe-Si alloys. First, neither composition could accommodate any measurable plastic deformation when rolled under ambient conditions, i.e., T_o = 25°C. Failure would occur suddenly after one or two rolling passes in a catastrophic manner with several cracks propagating throughout the entirety of the sample (see Figure 5-2). Catastrophic failure would continue in both alloys until a critical preheat temperature was reached. In the case for the Fe-4wt%Si alloy, an extremely sharp transition was observed over a 25°C range (from 75°C to 100°C) – near

T/T_m = 0.2 – after which the alloy could accommodate very large strains to failure. A similar transition was exhibited by the cast Fe-6.5wt%Si alloy but at a significantly higher temperature. In fact, at preheats close to half of the homologous temperature (T/T_m = 0.42), the alloy could only accommodate ~1/2 the strain to failure of the 4wt%Si composition ($\bar{\varepsilon}$ = 1.4 at failure).

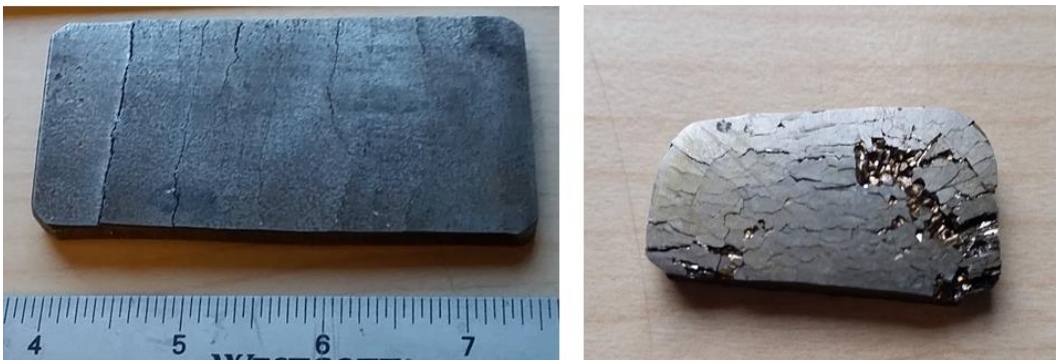

Figure 5-2 – Failed samples after 1 pass of cold rolling: (a) Fe-4wt%Si, (b) Fe-6.5wt%Si. Severe cracking is evident with cracks traversing the entire width of the specimens.

Analysis of the deformation microstructures, both at low and high temperatures, revealed some interesting results (Figure 5-3). At lower temperatures, the 4wt%Si and 6.5wt%Si samples were characterized by significant deformation twinning throughout the large grain structures. Room temperature twinning of Fe-Si is not commonly reported, however most investigations look at low strain rate tensile tests. The (relatively) higher strain rates in rolling (~ $10^2 s^{-1}$), in combination with the coarse grain size, may have promoted twinning as a deformation mode. Furthermore, higher Si compositions in Fe are known to increase the critical twinning temperature, up to ~5wt%Si.[19] Of particular interest is the appearance of twins in the Fe-6.5wt%Si alloy. Most literature has proposed

that the transition from short to long range atomic ordering at Si compositions above 5wt% suppress twinning modes in favor of complex superlattice dislocation motion.[19,40] However, a recent report noted significant deformation twinning in cast Fe-6.5wt%Si following plane strain compression even at temperatures as high as 400°C.[56,57] Therefore, perhaps the intrinsic aspects of the casting (i.e., large grain size, texture) promoted deformation twinning. In either case, transgranular fracture occurred almost immediately following the application of rolling deformation at low temperatures. Lack of plasticity and early fracture have often been associated with deformation twinning in Fe-Si and similar BCC structures.[58] However, no attempt is made here to identify the precise relationship between crack nucleation and propagation with twin formation, i.e., if twins formed cracks or cracks formed twins. Rather, it is imperative to simply state transgranular fracture occurred suddenly and the deformation structure showed evidence of significant twinning.

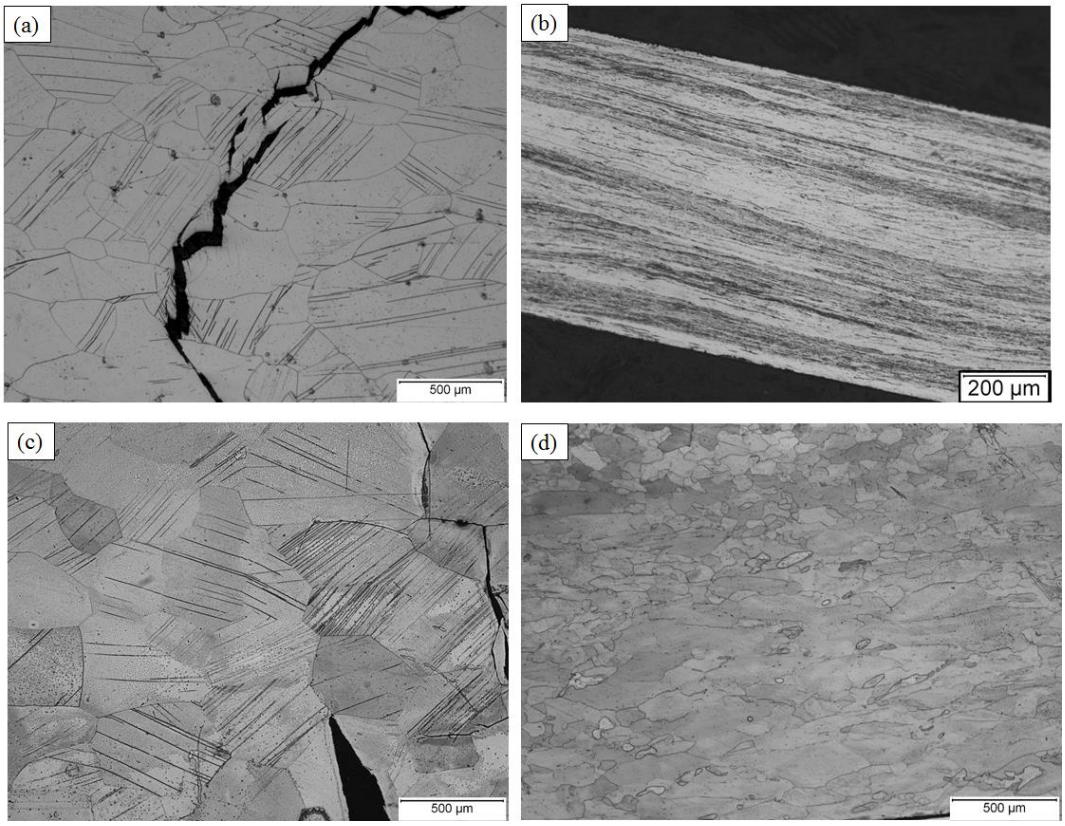

Figure 5-3 – Micrographs of sheet after failure during rolling. (a) and (b) are Fe-4wt%Si under ambient conditions and T_o = 100°C (T/T_m = 0.2). (c) and (d) are cast Fe-6.5wt%Si under ambient temperature and T_o = 450°C (T/T_m = 0.4). Microstructures of sheet without preheating possess a significant amount of twinning and cracks appear to be mostly transgranular. At elevated temperatures, twinning no longer appears to be the dominant deformation mode. For the 6.5wt%Si alloy, evidence of dynamic recrystallization is seen near the sheet surfaces.

At higher rolling preheat temperatures – T/T_m = 0.2 for Fe-4wt%Si and 0.4 for Fe-6.5wt%Si – twinning no longer appeared to be a dominant deformation mode and structures were significantly more homogeneous. Additionally, deformation could be accommodated in a plastic manner for both alloys up to large strains at failure. In the case for the Fe-4wt%Si alloy, temperatures were high enough at $0.2T_m$ to have slip as the primary deformation mode. Samples appeared to have classical cold-worked rolling structures with

elongated grains parallel to the rolling direction. This is suggestive of traditional slip as the primary deformation mode. Strains up to the limit of the rolling mill could be accommodated in a plastic manner, although significant side cracking was evident toward the upper end of the imposed strain.

For Fe-6.5wt%Si, the deformation microstructure at high temperatures revealed some interesting results. While a majority of grains in the thickness showed elongation in the RD, some regions revealed significantly finer equiaxed grains. These regions, primarily confined to the surfaces of the sample, are evidence of dynamic recrystallization. This is particularly interesting because to the authors knowledge, no other studies have shown dynamic recrystallization in cast Fe-6.5wt%Si following rolling deformation. Furthermore, despite recrystallization, sheet cracking still occurred.

In summary, rolling experiments were carried out on the Fe-Si alloys used in this study. Brittle fracture occurred, primarily manifesting as transgranular cracks, when rolling under ambient temperatures. Analysis of the deformation structures revealed significant twinning, which was not present when rolled at higher temperatures. Large strains ($\bar{\varepsilon} > 1$) could be imposed during deformation at higher temperatures without fracture of significant inhomogeneous deformation. The implications of these experiments suggest that Fe-Si alloys are indeed characterized by limited rolling workability at low temperatures. Large hydrostatic pressures in combination with high deformation temperatures of machining are advantageous to study simple shear deformation for these alloys.

5.2 Microstructure Evolution of Machined Fe-4wt%Si

The microstructures of the Fe-Si alloys were found to be a strong function of the processing conditions (strain rate and temperature) and the deformation characteristics (i.e., free machining vs. LSEM). Each of these effects are summarized.

5.2.1 Strain Rate and Temperature Effects in Conventional Machining

Temperature effects were identified in the rolling experiments to significantly influence the overall workability of the Fe-Si alloys. In machining, temperature and strain rate can be controlled over a much larger range than in conventional flat rolling. Therefore, to isolate effects of strain rate and temperature on the microstructural evolution of conventionally machined Fe-4wt%Si, a series of cutting experiments were performed under different V_o and T_o conditions for a given $\alpha = 0°$. V_o was varied from 2 m/s to 5 m/s and T_o from ambient (25°C) to 580°C. It is important to note that while deformation strain cannot be held perfectly constant during conventional cutting – the natural 'free' λ is a function of temperature and strain rate for a given material – the variability in λ and consequentially $\bar{\varepsilon}$ was significantly small. Specifically, these values were maintained within a 20% deviation throughout all experiments. Therefore, any strain effects driving metallurgical processes could be considered small compared to the processing effects. Results of the experiments are summarized in a processing-microstructure map presented in Figure 5-4, plotted as deformation temperature as a function of cutting velocity.

Three distinct microstructural regions were identified from the set of experiments, which are separated by diffuse boundaries (red-dotted lines in Figure 5-4) on the

processing-microstructure map. Note, these boundaries were merely constructed based solely on the presented experimental data points of the plot. Therefore, the shape and position of the boundaries should not be regarded as physical. Rather, they serve to qualitatively categorize the various metallurgical phenomena observed from experiments. The first region considered is located in the lower left corner of Figure 5-4 connecting samples (d) and (g) and is defined by relatively low V_o and T values. A single deformation condition, (a), is shown within this region and was characterized by a homogeneous deformation structure with metallurgical features (i.e., grains) aligned at an angle similar to the direction of shear. This so-called flow line structure exhibited grains with similar degrees of refinement throughout the chip body, which is generally credited to the lower V_o and T_o parameters. Furthermore, grains were elongated at an angle with respect to the direction of the material flow (CFD). Temperatures for this condition were unable to cause recrystallization and the sample condition (a) is considered fully cold-worked. However, it is significant to note that the adiabatic heating component of the total deformation temperature during machining was sufficient to avoid twinning. Consequentially, workpiece preheating was not required to produce continuous strips in machining.

With increased V_o, the deformation structures of machined samples underwent an observable transformation wherein the material flow was no longer homogeneous. This is well captured by samples (e)-(g) of Figure 5-4. Narrow regions within the chip microstructure were significantly more refined than other less-deformed adjacent regions. These highly refined regions possessed extremely narrow widths and are considered the initial signs of periodic adiabatic shear flow localization (i.e., shear bands). Shear bands are regions characterized by severely localized shear deformation wherein the local

material is subjected to massive shear strains, significantly larger than that imposed macroscopically in the bulk. The formation of shear bands, for adiabatic deformation processes such as machining, is generally believed to be related to the thermal softening behavior and thermal diffusivity of the deforming alloy.[44] A given material then is generally considered more susceptible to material localization if the flow stress is heavily a function of the deformation temperature and the thermal diffusivity is significantly small. With these attributes, high temperatures that occur during deformation will tend to cause local softening and, if the thermal diffusivity of the material is low, the heat of deformation will remain in the material and lead to continued softening. Therefore, deformation processes that introduce significantly high temperatures in an adiabatic manner (i.e., machining) will promote shear banding in some alloys. Since the thermal diffusivity of iron is significantly low (~ 20 * 10^{-6} m^2/s), and the flow stress of Fe-Si is known to drastically decrease with increasing deformation temperature, it is perhaps not surprising that adiabatic shear band formation was observed in this study.[59] It is important to note that adiabatic shear bands presented here are much less severe than those in previous studies on machining of Mg. In fact, specimens produced using classical machining were continuous ribbons under for all experiments. This is distinctly different than the behavior of Mg alloys under conventional 'low pressure' machining, which comes in the form of discrete discontinuous chips.[53] However, there is a clear onset of initial shear band formation in Fe-4wt%Si at $V_o \geq 4$ m/s in, as evidenced by both the periodicity of the 'saw-tooth' pattern on the free surface of machined chips and severely localized microstructural refinement.

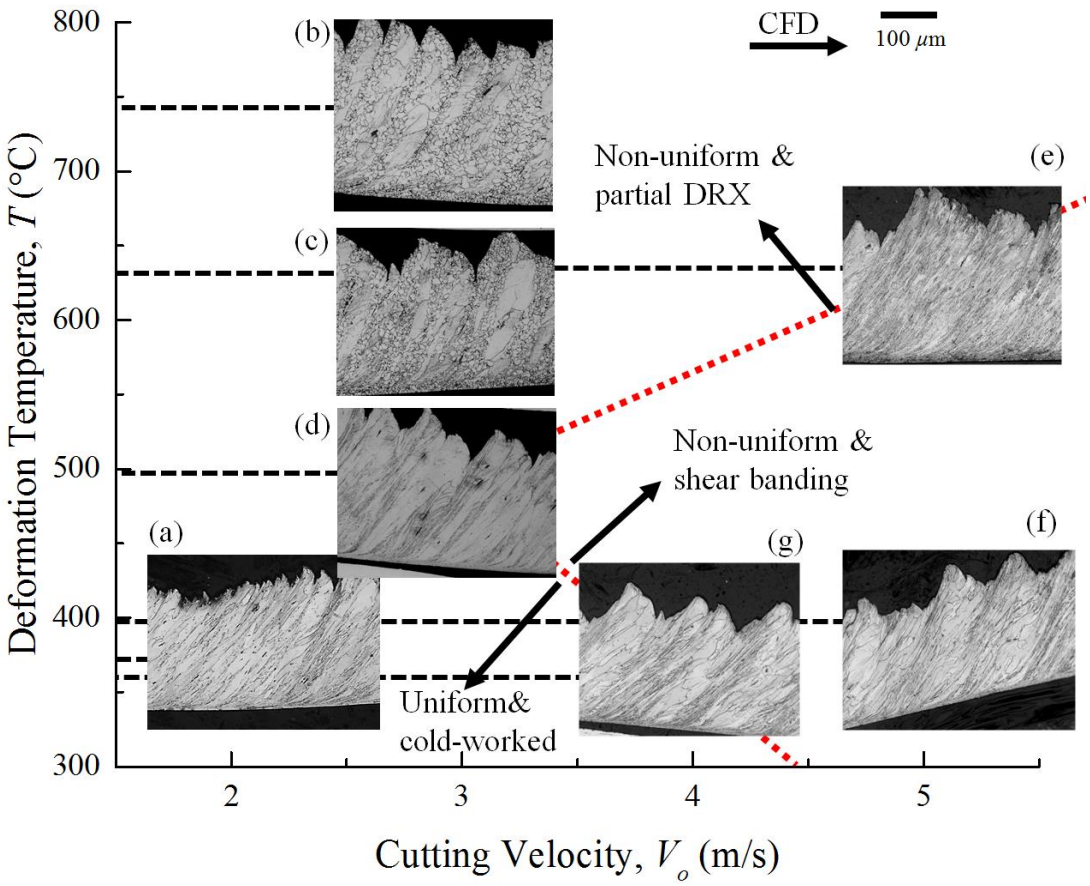

Figure 5-4 – Processing-microstructure map for Fe-4wt%Si following conventional machining at α = 0°. Deformation strain varied less than 20% between samples, providing a close measure of truly isolated effects of temperature and cutting velocity on microstructure evolution.

Since adiabatic shear banding is believed to be driven primarily by thermal events, it is also perhaps not surprising to see that the high temperature region, samples (b) and (c), on the processing map showed more pronounced flow localization than the lower temperature counterpart. Higher temperatures were accomplished by preheating the workpiece prior to deformation. With increasing temperature, the periodicity of the adiabatic shear bands increased and recrystallized grains appeared while the surrounding matrix remained in an as-deformed condition. The nature of the shear bands – the locally

high strains and temperatures – in combination with the preheating temperatures were sufficient to cause recrystallization *in-situ* (i.e., dynamic recrystallization, DRX). A higher magnification image of a partially recrystallized specimen is shown in Figure 5-5. Note also that recrystallization occurred along the bottom surface of the chip specimen, which is attributed to combined higher strains and temperatures from secondary shear deformation from material sliding at the material-cutting tool interface during cutting.

The essential takeaway from these experiments is that the high temperatures and hydrostatic pressures of machining suppress deformation modes in Fe-Si that would otherwise result in low plastic strains to failure. Consequentially, the fundamental aspects of simple shear deformation *via* machining are encouraging for developing continuous Fe-Si sheet.

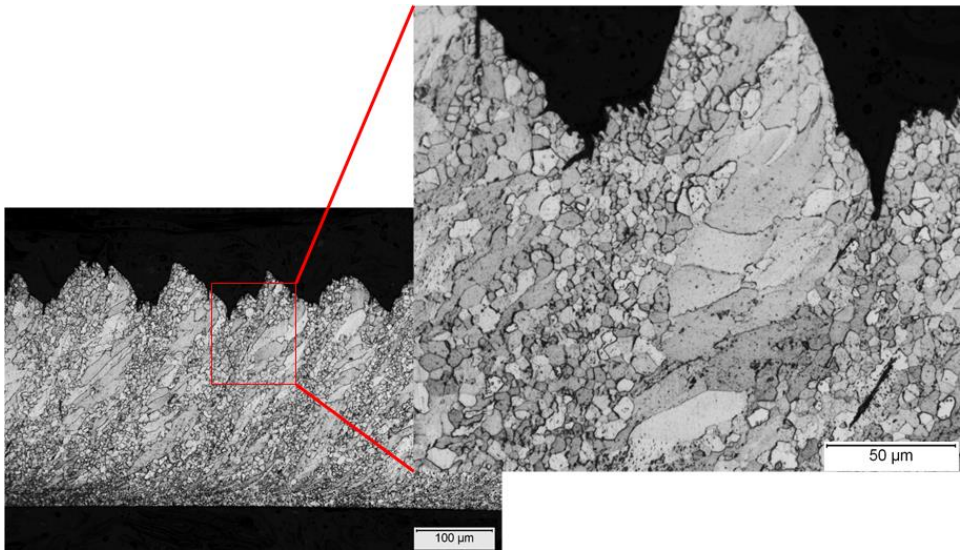

Figure 5-5 – Higher magnification image of a high temperature deformation condition. The high deformation temperatures, in combination with the thermal softening and low thermal diffusivity of Fe-Si, led to dynamic recrystallization (DRX) of the adiabatic shear bands. DRX also occurred along the bottom chip surface, which was in contact with the cutting tool rake face during deformation.

5.2.2 Strain Rate and Temperature Effects in LSEM

While the deformation experiments in conventional machining shed light on the behavior of Fe-4wt%Si following simple shear deformation, issues with flow localization and the low quality, serrated free surfaces on specimens are not ideal sheet characteristics for electromagnetic applications. As a method to combat these, the highly confined simple shear deformation of LSEM was used to also systematically evaluate the microstructural evolution in Fe-4wt%Si. As with conventional machining, a processing-microstructure map is also used to describe LSEM specimens. An effort was made to maintain the same V_o and T_o deformation parameters used in the conventional machining experiments to identify the key advantages of LSEM. However, because LSEM necessarily requires λ to be smaller than conventional cutting, $\bar{\varepsilon}$ values were slightly lower than those in conventional cutting. In some materials however, λ values can be selected ($\lambda < 1$) so as to impose nearly identical deformation strains as those imposed in conventional machining. For reference, a typical continuous strip and microstructure from the Fe-4wt%Si plate at low V_o = 1 m/s is shown in Figure 5-6. Note, at this low condition, a homogeneous cold-worked structure was observed. A homogeneous flow-line type microstructure was developed in the sheet with the flow lines aligned in the direction of maximum tensile strain imposed during the deformation; this direction is inclined at an angle to the shear plane, the angle being related to the imposed strain.

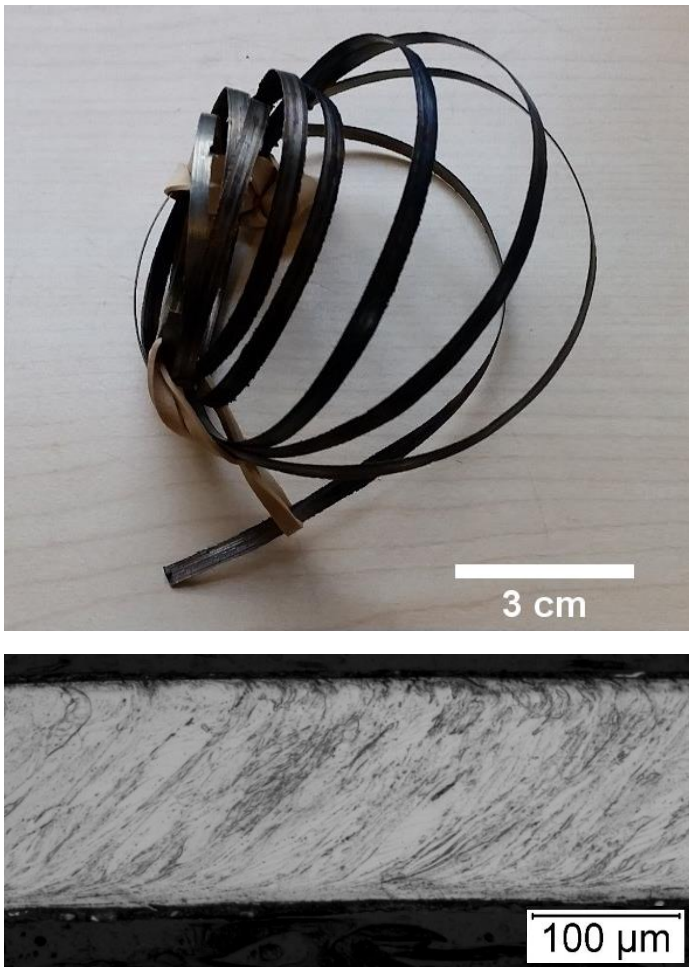

Figure 5-6 – Long (1.80 m), thin (460 μm) Fe-4 wt% Si alloy strip (top) produced by the shear deformation (λ = 1.7, V_o = 1 m/s, and α = 5°). Optical micrograph (bottom) shows a uniformly deformed microstructure in strip.

The LSEM equivalent processing-microstructure (deformation temperature T vs. cutting velocity V_o) map for Fe-4wt%Si is summarized in Figure 5-7. As with the conventional machining experiments, drastic changes in the microstructure of Fe-Si strips were observed in the processing-microstructure space. At lower T, notably throughout the entire range of V_o, LSEM resulted in uniform microstructures characterized by the classical flow line type deformation structures. This is significant because, despite slightly higher

deformation temperatures in LSEM compared to the conventional machining equivalents at the same V_o, adiabatic shear banding was not observed. Additionally, even at the equivalently lowest V_o, partial dynamic recrystallization was observed along the top and bottom surfaces of LSEM specimens. This is additional testimony to the higher deformation temperatures that result from the application of a constraint. Annealed grains in these regions were extremely fine (grain size, d, < 1 μm). Selective recrystallization of the strip surfaces resulted from additional shear deformation due to material sliding at tool-material interfaces during cutting and further heating from friction. As will be shown, the thickness of these zones can be controlled to some extent during LSEM.

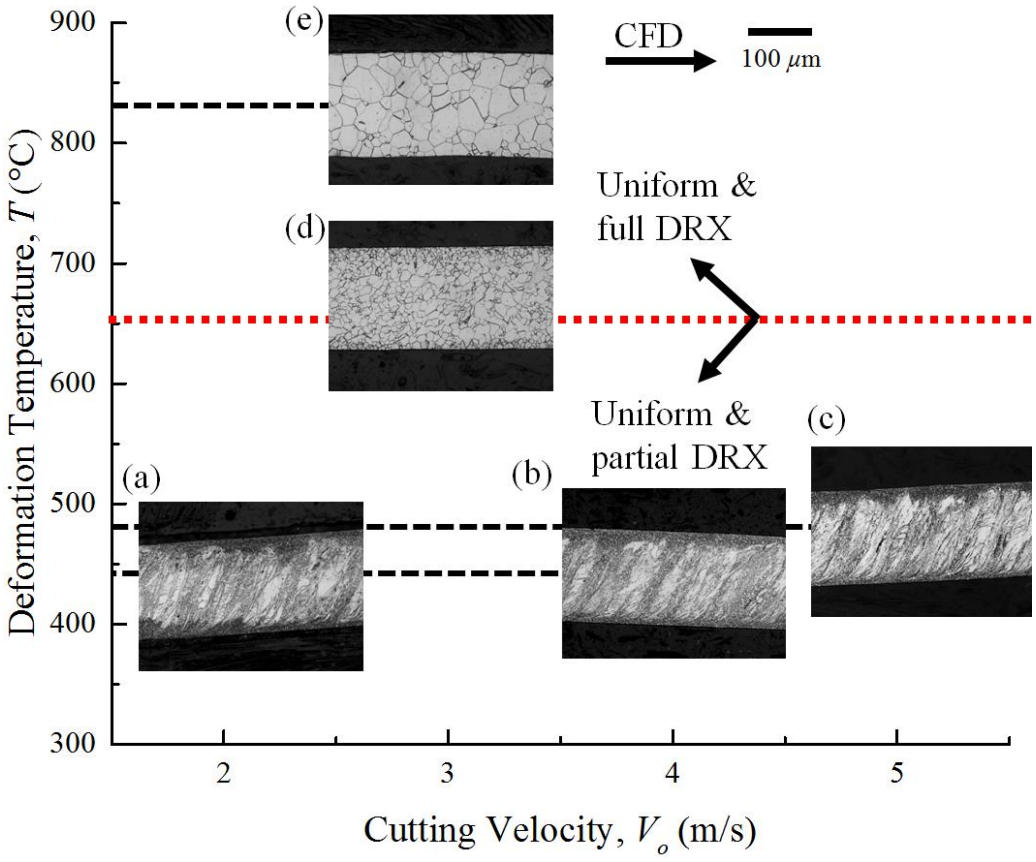

Figure 5-7 – Processing-microstructure map for LSEM Fe-4wt%Si. Conditions presented were designed to mimic those used in conventional cutting to effectively highlight the

differences in the two processes. Application of a constraint during metal cutting confines the deformation zone and prevents free surface slip, leading to a suppression of adiabatic shear bands. Furthermore, the deformation is intensified in the deformation zone during LSEM under the same nominal T_o and V_o conditions, creating higher deformation temperatures and causing homogeneous DRX.

Suppression of flow localization events, such as adiabatic shear flow localization, through the application of a constraint during metal cutting has been noted previously.[46] While the general material characteristics required for shear banding have been outlined, the metallurgical processes leading to its formation have not been discussed. Characterization of these processes have been utilized from similar PIV analysis techniques presented earlier for describing the deformation path (Section 3.1.2). Generally, two main events occur during the formation of shear bands.[46] The first is a rapid development of a so-called planar 'weak path' in the developing chip ahead of the cutting tool tip, which proceeds shear flow localization. With continued deformation and a suitably developed planar 'weak path', localized shear occurs in the forming chip along this path. Material on either side of the localized shear region move effectively as rigid bodies, reducing the load carrying area of the material. The reduced load carrying area has been thought to contribute to the thermal softening of the developing chip within the deformation zone, creating a compounding effect with the adiabatic nature of machining. The result is massive localized deformation, similar to so-called stack-of-cards shear, and results in a chip extrudate with a 'saw tooth' type appearance on the free surface – as documented in Figure 5-4. Suppression of these processes, through the application of the constraint in LSEM, is believed to result by restricting the macroscale shear displacements that are normally unconstrained in conventional machining.

Of critical importance to successfully suppress the macroscale shear displacements of shear banding then is the degree of constraint – directly determined *a priori* by the λ parameter. The minimum λ value necessary for suppressing shear localization must account for the height deviations in the free chip surface from the macroscale shear displacements that develop during conventional cutting. An example demonstrating this criterion is shown in Figure 5-8. In this case, higher deformation temperatures promoted further developed shear bands, where the low-end macroscale shear displacements were $\lambda \sim 1.5$ with high-end displacements exceeding $\lambda \sim 2.5$. Therefore, the LSEM parameters were selected with λ sufficiently smaller than 1.5 for fully constraining the material during deformation.

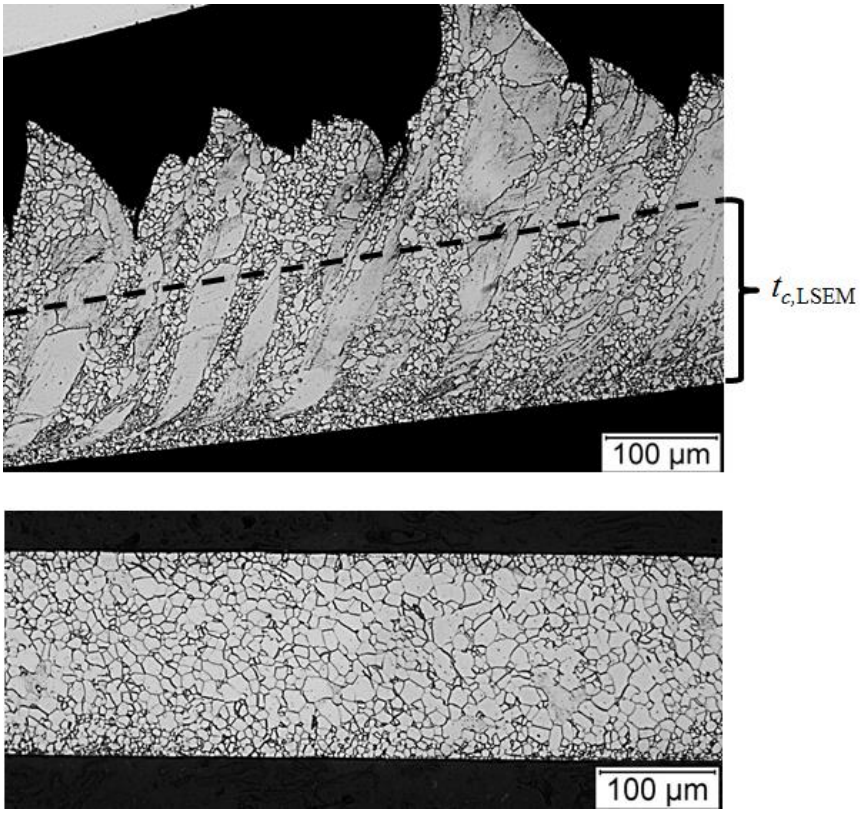

Figure 5-8 – Full suppression of flow localization *via* the constraint in LSEM must be small enough to account for the varied free surface height of a conventionally machined chip, which results from the macroscale shear displacements defining the shear bands. In this case, the final thickness of the LSEM strip was small enough to include the 'peaks' and 'valleys' of the unconstrained chip processed at the same T_o and V_o.

Additionally, similar to the conventional machining conditions, slightly higher total processing temperatures for LSEM produced specimens with fully annealed structures from dynamic recrystallization. However, confinement of the deformation from the constraint prevented the natural tendency for shear localization. Moreover, the annealed grain size was controllable depending on the value of T_o used prior to deformation. For instance, when T_o = 300°C (T = 650°C), the nominal grain size (d) was 8 μm. Increasing T_o to 550°C (T = 830°C), the average grain size increased to 25 μm (see Figure 5-9). Similar increases in the stable grain size during dynamic recrystallization with increasing deformation temperature have been noted in other systems. [60,61]

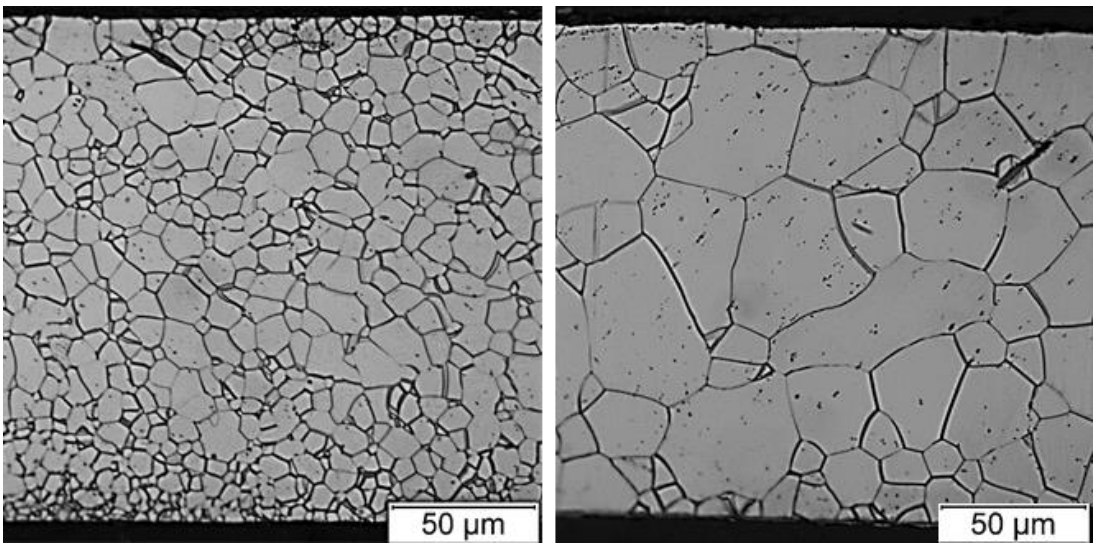

Figure 5-9 – Grain size increased in dynamically recrystallized samples from higher deformation temperatures during LSEM: (a) T_o = 300°C (d = 8 μm), (b) T_o = 550°C (d = 25 μm).

5.2.3 Inhomogeneity at Low V_o

Deformation structures presented thus far have been from processing conditions characterized by high cutting velocities, i.e., $V_o \geq 2$ m/s. Higher deformation temperatures and cutting velocities tend to promote inhomogeneous deformation through adiabatic shear flow localization. However, inhomogeneites can also occur when cutting velocities are sufficiently small (i.e., $V_o < 2$ m/s). To explore this, two LSEM experiments were conducted at $V_o = 0.25$ m/s. Results are shown in Figure 5-10.

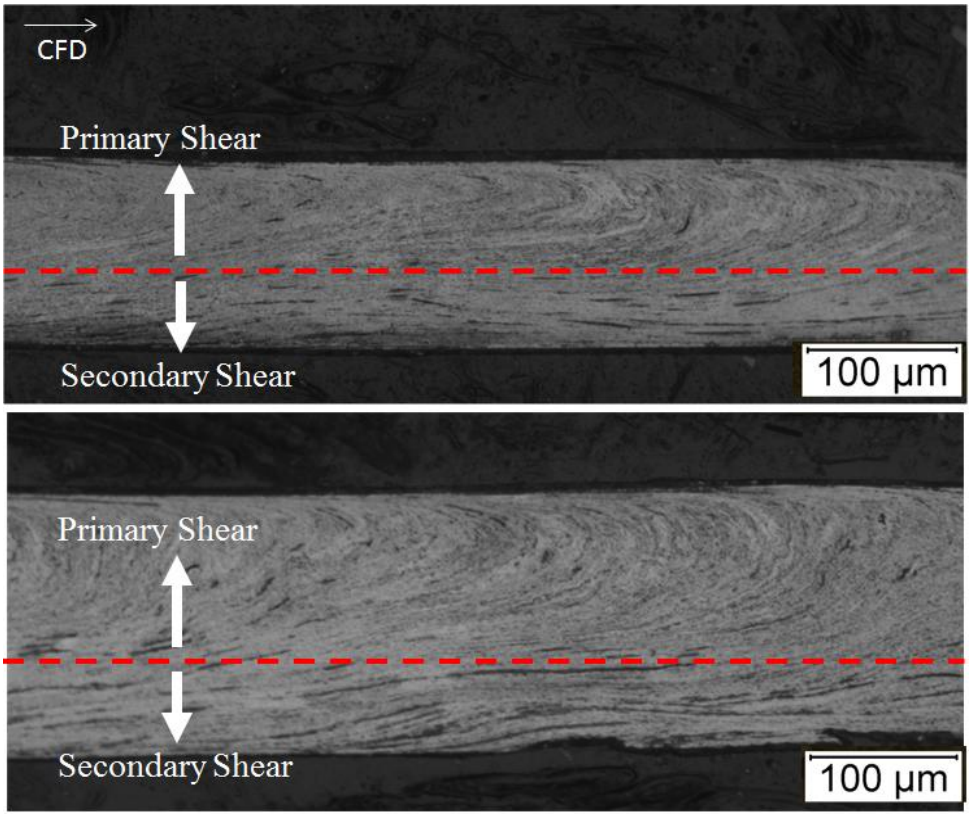

Figure 5-10 – LSEM strips produced at low cutting velocities, $V_o = 0.25$ m/s, showing inhomogeneity in the shear deformation: (a) $\lambda = 1$, $\alpha = 5°$, (b) $\lambda = 1.5$, $\alpha = 5°$. Larger secondary shear zones in strip samples resulted due to significant friction at the cutting tool-material interface during low speed cutting.

Flow-line structures in the slow V_o LSEM conditions exhibited local inhomogeneity with two distinct microstructural regions in the strip through-thickness. One region, located from the red dotted line to the top (constraint) strip surface in Figure 5-10, showed flow lines typical of machining deformation structures at high V_o. Grains were highly refined (sheared) and inclined relative to CFD, as expected from the simple shear deformation. Similarly, the bottom region, red dotted line to bottom (rake) strip surface, also possessed highly refined flow lines, however the orientation of these flow lines was nearly parallel to the strip length (i.e., CFD). While the deformation was still simple shear in nature, the orientation represents a clockwise rotation of the original (parent) simple shear deformation inherited from the deformation zone in LSEM. This rotation, also more pronounced in low V_o conventional machining, is particularly significant in LSEM, consuming ~1/3 of the total strip thicknesses (t_c).

Such microstructural inhomogeneity resulted from secondary shear deformation at the cutting tool-material interface. Low cutting velocities are known to increase the coefficient of friction at the tool-material interface during traditional metal cutting, therefore it is perhaps not surprising to see an increased microstructural region dominated by sliding friction.[62] Furthermore, the application of a constraint in LSEM – when set at λ values lower than those produced in conventional cutting – is expected to accentuate the normal forces at the cutting tool rake face during deformation, thereby also increasing the magnitude of the friction force during deformation. While a large secondary shear zone in strip microstructures might be considered undesired, it has interesting effects in local (micro) crystallographic texture, which will be discussed later in the chapter.

5.2.4 Microstructures in Fe-6.5wt%Si

Systematic characterization of the Fe-4wt%Si alloy revealed a wide range of microstructures that developed from various metallurgical processes active in the alloy under the high temperatures and rates of simple shear deformation by machining. Of particular interest, due to the optimized magnetic properties (Section 2.3), is the Fe-6.5wt%Si. This composition is particularly known for limited workability, as was shown in the rolling experiments, where the intrinsic composition effects on the workability, in combination with the as-cast starting microstructure, showed extreme difficulty in rolling. Consequentially, some machining experiments were conducted on the cast alloy with a goal of observing similar microstructural regions to the Fe-4wt%Si alloy. Three experiments were conducted and the results are summarized in Figure 5-11.

The first condition (a) represents a conventional machining specimen obtained at V_o = 25°C with no preheating. Microstructural analysis indicated that, despite the lower V_o value, severe shear flow localization occurred. Since large grain sizes in combination with the as cast structure limit workability, it is perhaps not surprising to see flow localization occurring at lower V_o then the Fe-4wt%Si alloy. Interestingly, even at the low V_o and T_o conditions, specimens were continuous following machining without fracture and deformation twinning. This is particularly striking since rolling preheat temperatures of ~0.45T_m were required to avoid cracking of the cast ingot.

Through the application of the constraint *via* LSEM, sample conditions (b) and (c) in Figure 5-11, continuous sheets were also produced with varying degrees of dynamic recrystallization. Specifically, with a ‘low’ degree of constraint and lower T_o, partial

dynamic recrystallization was observed, similar to some the Fe-4wt%Si specimens. With increased constraining and T_o, full dynamic recrystallization was observed in the Fe-6.5wt%Si strip.

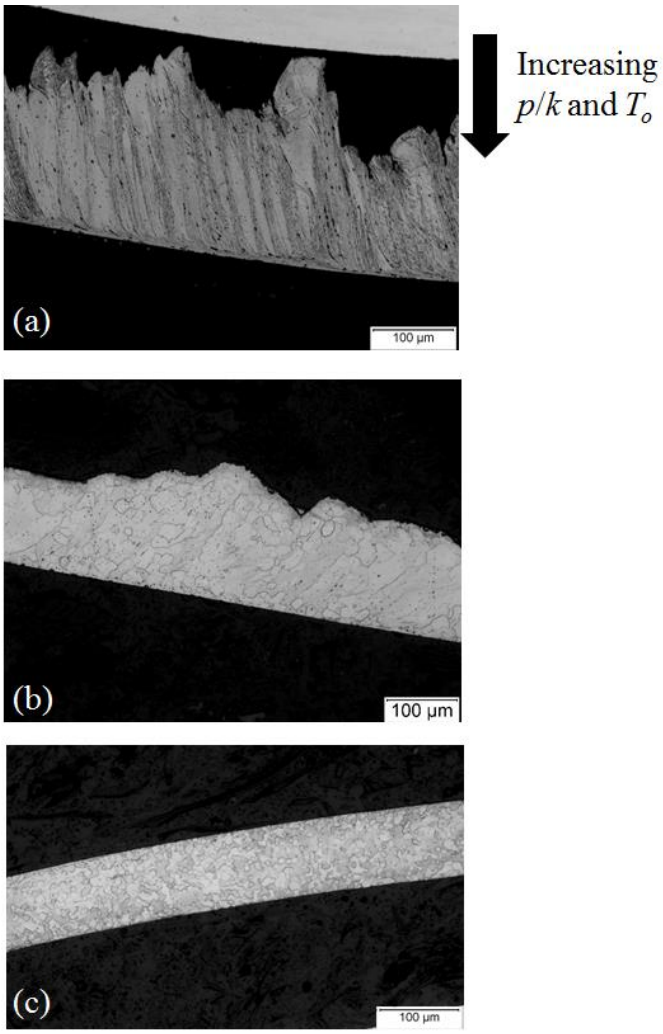

Figure 5-11 – Three experimental conditions on the as-cast Fe-6.5wt%Si ingot: (a) conventional machining, V_o = 2 m/s, T_o = 25°C, (b) λ = 1.5, V_o = 3 m/s, T_o = 400°C, (c) λ = 0.95, V_o = 3 m/s, T_o = 500°C. A cutting tool with α = 5° was used for all experiments. As expected and first described in the Fe-4wt%Si experiments, increased p/k and T_o resulted in a transition from a shear flow localized structure to a fully recrystallized strip. Note, samples were produced from a coarse grain cast ingot.

Processing of the ideal Fe-6.5wt%Si alloy in continuous sheet form is particularly impactful for electromagnetic applications to fully optimized performance. Of particular interest here was the ability to produce continuous strip samples from the cast alloy for all three deformation conditions – even without preheating – using simple shear deformation *via* machining. This is significantly different than the case for rolling, which required especially high T_o values to eventually reach similar strains without cracking. Two main possible considerations must be discussed to explain the stark differences in the workability behavior of the Fe-6.5wt%Si alloy following the two different deformation processes. First, the mechanics of simple shear deformation *via* machining produce significantly high adiabatic heating and hydrostatic pressures in a narrow deformation zone (width $\Delta \sim 100$ μm). This is compared to the relatively diffuse deformation zone of rolling mill (width, $\Delta \sim 10$ mm for the present case) and the lower temperatures and hydrostatic pressures. Even in the conventional unconstrained machining condition, which imposed the smallest hydrostatic pressure with p values $\sim 2k$, is nearly a two-fold increase compared to plane strain flat sheet rolling ($p \sim k$).

The second consideration worth discussing is related to the as-cast ingot structure. To develop the Fe-6.5wt%Si alloy, high purity Fe and Si materials were used as the initial charge for a casting. To avoid significant contamination from atmospheric species, the casting was performed under vacuum with a backfilled atmosphere consisting of Ar-5%H_2 gas. However, even under such conditions, as-cast defects (i.e., segregation, voids, impurities) are important to consider. During rolling, half-sections of the entire cast ingot diameter were subjected to the deformation. Consequentially, any existing cast defects that might have developed during solidification were subjected to the deformation of rolling.

This is unlike machining, which essentially removed thin layers of the outer most regions of the cast ingot workpiece. Therefore, examination of the cast structure, with respect to common casting defects, is crucial. Both cast voids and segregation are considered.

Following extensive microstructural analysis, the as-cast ingot did not possess any notable microshrinkage voids anywhere in the ingot cross-section (see Figure 4-2). Rather, a significantly large shrinkage pipe occurred near the top of the solidifying ingot. While this would clearly develop workability issues in the rolling and machining of the cast ingot, this section was removed prior to any deformation. Therefore, the small diameter of the casting, the narrow freezing range of the alloy and sub-atmospheric inert reducing gases utilized during solidification eliminated any significant microshrinkage porosity. Furthermore, elemental analysis of the ingot cross-section revealed that the small diameter of the ingot resulted in negligible macrosegregation (not shown), which is common in large-scale production castings. Consequentially, it is suggested that the high temperatures and hydrostatic pressures, intrinsic to the simple shear deformation of machining, were the necessary processing attributes that allowed for continuous sheets to be produced from the Fe-6.5wt%Si ingot.

In summary, machining deformation resulted in a wide range of microstructures for the two Fe-Si alloys. At low V_o and T, microstructures were generally homogeneous in conventional machining of Fe-4wt%Si, with heavily sheared grains oriented in a direction similar to the shear direction in machining. With increasing V_o and T, microstructures exhibited shear localized flow in the form of adiabatic shear bands, which were accentuated at higher T values along with the onset of partial dynamic recrystallization in the bands.

Through the application of a constraint during metal cutting (LSEM), adiabatic shear bands were suppressed and homogeneous structures were developed throughout all deformation conditions. With suitably high *T* values, structures experienced full dynamic recrystallization with varying grain size as a function of deformation temperature. Similar transitions from adiabatic shear bands to fully homogeneous, dynamically recrystallized structures were also achievable in cast Fe-6.5wt%Si. The synergetic combination of high temperatures and hydrostatic pressures, intrinsic to machining, allowed large strains to be imposed in the low workability Fe-Si alloys without fracture.

5.3 Crystallographic Texture

Ideal crystallographic textures produced in simple shear deformation are first discussed as an introduction. Then, measured textures are presented from a range of samples produced using both conventional machining and LSEM. Texture measurements were gathered from low temperature (cold-worked structures) and high temperature (dynamically recrystallized structures) deformation conditions as well as post processed annealed and grain growth structures. Experimental textures are related to the deformation parameters. Finally, a theoretical analysis of the simple shear textures of machining is provided with respect to optimizing magnetic properties.

5.3.1 Ideal Simple Shear Textures

As briefly mentioned in Section 3.1 and in ref. [55], machining is modeled as a simple shear deformation process. In BCC, the ideal simple shear textures are best described by two main partial crystallographic fibers, denoted by {110}<uvw> and

{hkl}<111>. [63,64] The former represents an alignment of the {110} crystallographic planes with the macroscopic shear plane, while the latter is characterized by <111> crystallographic directions aligned with the macroscopic shear direction, respectively. Similar texture notation schemes have been used to describe FCC and HCP simple shear textures. Illustration of these ideal BCC simple shear fibers is shown on a (110) pole figure, with reference axes defined by y – shear plane normal and x – shear direction. Below the pole figure is a table listing some prominent ideal texture components along the two partial fibers. It is important to note that, with respect to the sample axes, the crystallographic textures are inclined. Consequentially, the ideal miller indices notations describing the texture components are only correct along the macroscopic shear plane axes. For texture components in reference axes defined by the deforming material (e.g., rolling direction/extrusion direction and surface normal), the ideal miller indices must be rotated by the appropriate inclination angle. In the present, the general interest is the overall texture character. Therefore, most of the analysis does not emphasize texture component volume fraction and miller indices descriptions. However, some important texture components for magnetic applications will be discussed.

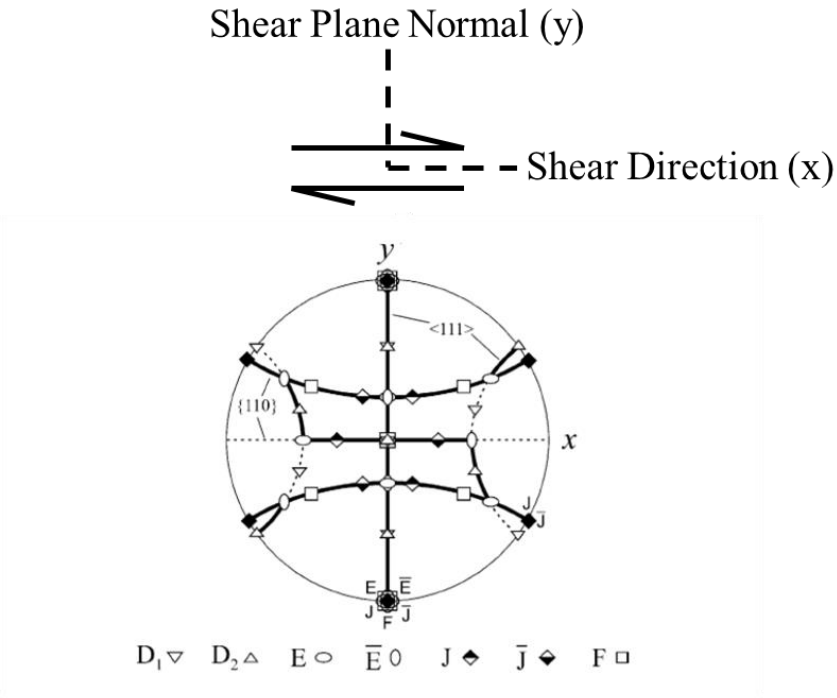

Table 2
Main ideal orientations in simple shear deformation of bcc materials

Notation	$\{h\,k\,l\}\langle u\,v\,w\rangle$	Euler angles (°)[a]		
		φ_1	ϕ	φ_2
D_1	$(\bar{1}\,\bar{1}\,2)[1\,1\,1]$	54.74/234.74	45	0/90
		144.74	90	45
D_2	$(1\,1\,\bar{2})[1\,1\,1]$	125.26	45	0/90
		35.26/215.26	90	45
E	$(\bar{1}\,\bar{1}\,0)[\bar{1}\,\bar{1}\,1]$	90	35.26	45
$\bar{E}$	$(1\,\bar{1}\,0)[\bar{1}\,1\,1]$	270	35.26	45
J	$(\bar{1}\,\bar{1}\,0)[\bar{1}\,\bar{1}\,2]$	90/210	54.74	45
$\bar{J}$	$(\bar{1}\,\bar{1}\,0)[\bar{1}\,1\,\bar{2}]$	30/150/270	54.74	45
F	$\{1\,1\,0\}\langle 0\,0\,1\rangle$	0/180	45	0/90
		90/270	90	45

[a] Given in the $\varphi_2 = 0°$, 45° and 90° sections with $\varphi_1 = 0$–270° only.

Figure 5-12 – Ideal simple shear crystallographic texture fibers in BCC metals. Textures are defined by partial {110} and <111> fibers with respect to the shear plane normal and shear direction axes. A table of ideal texture components in the simple shear fibers is also shown (after [64], with permission of Elsevier).

5.3.2 Low and High Temperature Deformation Textures

A typical as-deformed EBSD inverse pole figure color map and representative pole figures is shown in Figure 5-13. The axes used for pole figures were the rake face normal (RFN) and chip flow direction (CFD), which provided a convenient way to analyze the texture fibers. Black regions in the inverse pole figure color map indicated areas that were severely deformed and consequentially produced low signal. Therefore, these regions were not included in the texture analysis. Additionally, blurred grain boundaries were present, expected from microstructures containing high dislocation density.

The texture is represented using the (100), (101) and (111) pole figures, obtained from the sheet thickness cross-section (RFN-CFD plane). As expected, it is predominantly characterized by two partial {110} and <111> fibers, highlighted by the dotted lines in the (101) pole figure for reference. The ideal {110} fiber results from an alignment of the (110) plane in a direction parallel to the shear plane; this fiber also reflects orthotropic symmetry around the plane normal. Similarly, the ideal <111> fiber arises from [111] aligning along the shear direction, with orthotropic symmetry around this direction. Note, these partial fibers are inclined relative to the sample axes. This inclination can be measured directly on the pole figure and compared with the orientation of shear plane for the given machining parameters. For the selected deformation condition, the measured textures were inclined, counterclockwise with respect to the CFD, at an angle of 78°, which is close to the theoretical value expected from the shear plane model ($\phi' = 81°$). Given the relatively large strain imposed in the sheet ($\bar{\varepsilon} = 1$), this close alignment of the fibers with the theoretical shear orientation should perhaps be expected.

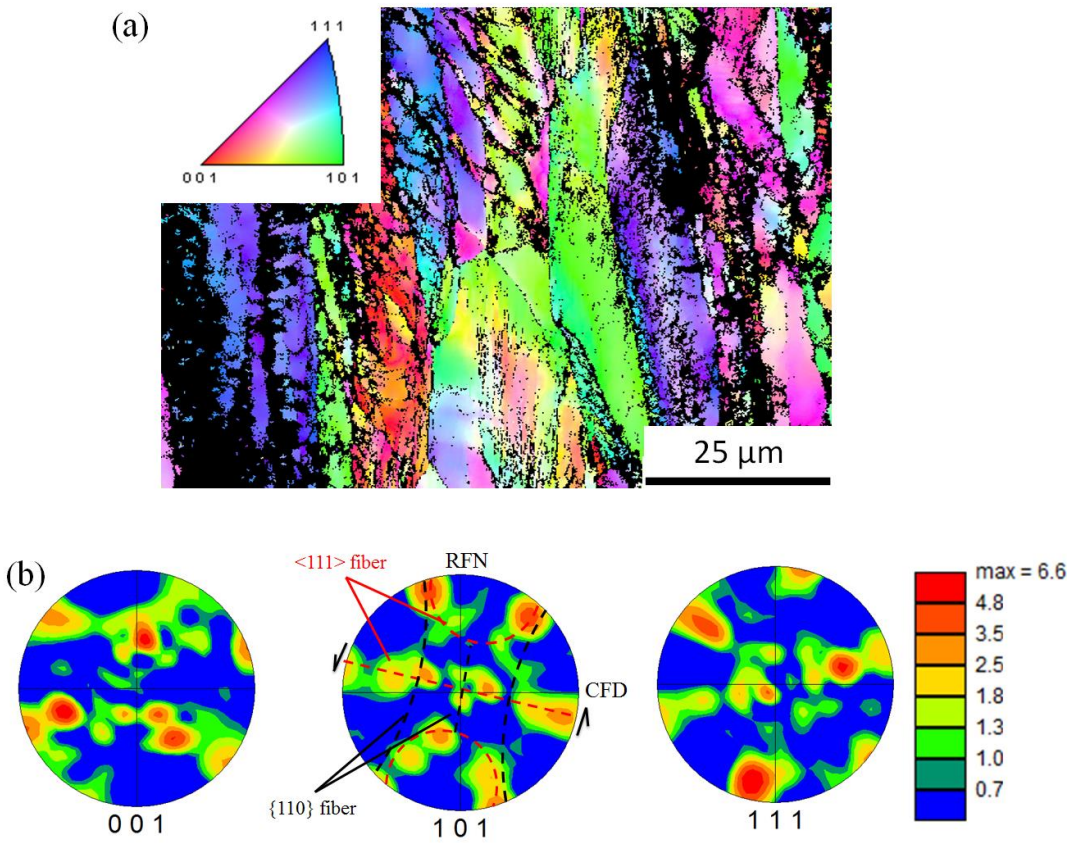

Figure 5-13 – Deformation texture in typical cold-worked machining of Fe-4wt%Si. (a) an inverse pole figure color map showing the heavily sheared as-deformed structure. (b) the three main (100), (101) and (111) pole figures used to describe the texture of BCC Fe-Si. Reference axes are defined by chip flow direction (CFD) and rake face normal (RFN).

As mentioned in the microstructure section of the results (Section 5.2.2), high deformation temperatures developed fully annealed structures from dynamic recrystallization. Interestingly, the texture character in the dynamically recrystallized sheet (Figure 5-14) were found to be essentially the same as those in the sheet produced without pre-heating of the sample at the same cutting condition, i.e., the deformation texture. A slight decrease in texture intensity, given by multiples of a random distribution (MRD), were measured in the dynamically annealed state when compared to the as-deformed state.

In the case for the high temperature deformation condition (λ = 1.7, V_o = 3 m/s), the angle by which the fibers were rotated was 76°, also consistent with the shear plane orientation (ϕ' = 80°) for the process condition. Consequentially, a sense of the texture evolution as a function of deformation conditions could be assessed following static recrystallization treatments. Texture measurements in the following then relate the recrystallized (annealed) textures with the corresponding processing conditions. It is also clear from Figure 5-13 and Figure 5-14 that the (101) pole figure captures the essential details of the shear texture in this BCC system; henceforth, only this pole figure is used to describe the texture.

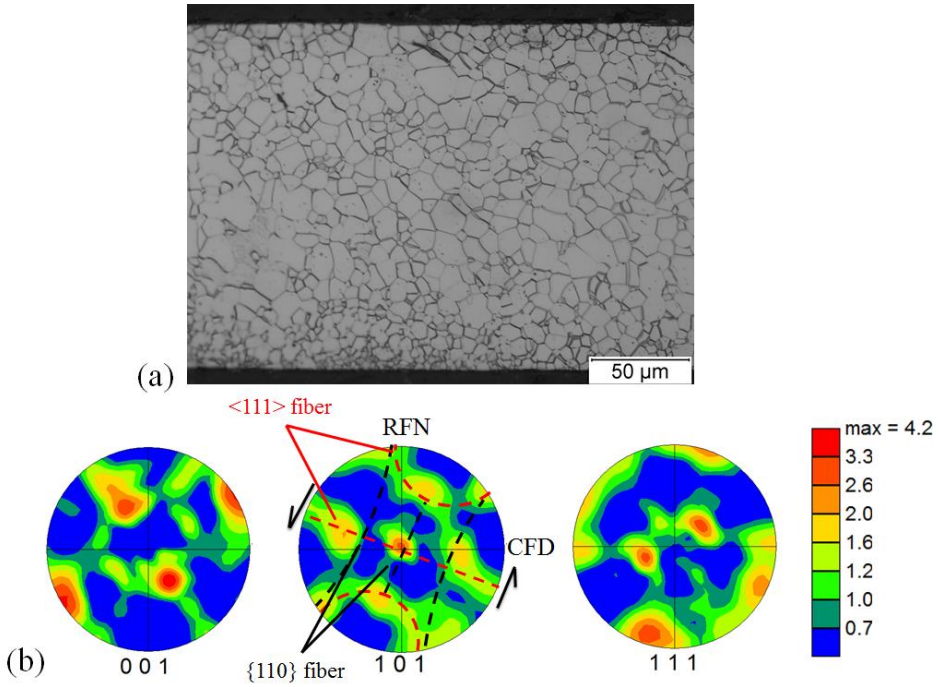

Figure 5-14 – Dynamic recrystallization during the simple shear at high temperature. (a) A microstructure representative of the dynamically recrystallized sheet. (b) The three (100), (101) and (111) pole figures for the recrystallized sheet (λ = 1.7, α = 5°, V_o = 3 m/s, and T_o = 300°C) showing the shear texture resembling the deformation texture shown in Fig. 4.

5.3.3 Recrystallization Textures

The simple shear (deformation) texture in the sheet also was observed to be retained even after static recrystallization at 700°C. The principal change during the static recrystallization was a sharpening of the shear texture components (higher pole figure intensities). This equivalence between the deformation and recrystallization textures provides an avenue for studying the effect of the shear deformation path on sheet texture, as shown in Figure 5-15. For this series of experiments, ϕ' was varied in the range of 41°-76^o by adjusting λ and α, and the texture was measured after static recrystallization. A close correspondence between the measured texture fiber orientations and ϕ' of the shear plane can be seen in the plot in Figure 5-15, demonstrating the feasibility of engineering crystallographic texture in the sheet through direct control of the simple shear deformation. Similar one-to-one correspondence between texture and deformation path in simple shear has also been noted in HCP Mg AZ31B.[10] Taken as a whole, recrystallization (both dynamic and static) texture evolution in Fe-Si is largely determined by the strain path underlying sheet formation, and is negligibly influenced by any post-process (recrystallization) annealing.

Similar texture retention following recrystallization has also been noted in Mg AZ31B alloy sheet produced by LSEM, suggesting that this process deformation texture in HCP and BCC metals may, in a more general sense, be quite resilient to recrystallization. While similar deformation texture retention following annealing has been noted also in other large-strain deformation studies[65–68], its observation in Fe-Si is particularly striking, since this system is known to undergo sharp transformations in the texture during

recrystallization, especially at high temperatures.[35] The observed texture behavior may be explained by discussing, more generally, the effects of intense plastic deformation. It is well known that large deformation strains promote the formation of structures characterized by a high density of high-angle grain boundaries.[69] These boundaries are formed by fragmentation of original coarse grains or through gradual increase in misorientations of the sub-grain structure upon incremental deformation. These phenomena constitute the basis for producing bulk ultrafine-grained (UFG) materials. In comparison to most conventional deformation processes (i.e., rolling), the large-strain deformation conditions in this study are characterized by much higher strain rates, on the order of 10^4 /sec. The deformation-induced heating effects, which are pronounced at these high strain rates, will therefore promote the formation of thermodynamically more stable UFG substructures predominantly characterized by high-angle boundaries. When such UFG structures are subjected to annealing, a homogeneous coarsening of the structure likely occurs through grain-boundary migration, as opposed to discrete nucleation events, typical of classical discontinuous static recrystallization (dSRX). This coarsening may be expected to continue until a stable equiaxed structure is achieved – a microstructural evolution referred to as continuous static recrystallization (cSRX). Thus, the cSRX mechanism necessarily results in the retention of the deformation texture, unlike dSRX.[70,71] Additional support for cSRX in the present case has been acquired from incremental annealing experiments (presented in the next section), which showed a much reduced incubation period for recrystallization and limited inhomogeneous nucleation. Similarly, when deformation temperatures were imposed wherein the dynamically

recrystallized texture was the same as the deformation texture, it is likely that continuous dynamic recrystallization (cDRX) is operative.

It was also noted that the Fe-Si disk surface experienced negligible subsurface deformation during the LSEM. As a result, the residual WP texture was essentially unchanged after each cutting pass used to produce sheet. This is in contrast to Mg alloys, wherein significant subsurface deformation occurred in the WP following each cutting pass.[10] In the latter case, the initial WP texture is substantially altered prior to entering the deformation zone; and these texture changes have to be considered in analysis of the final sheet microstructure.

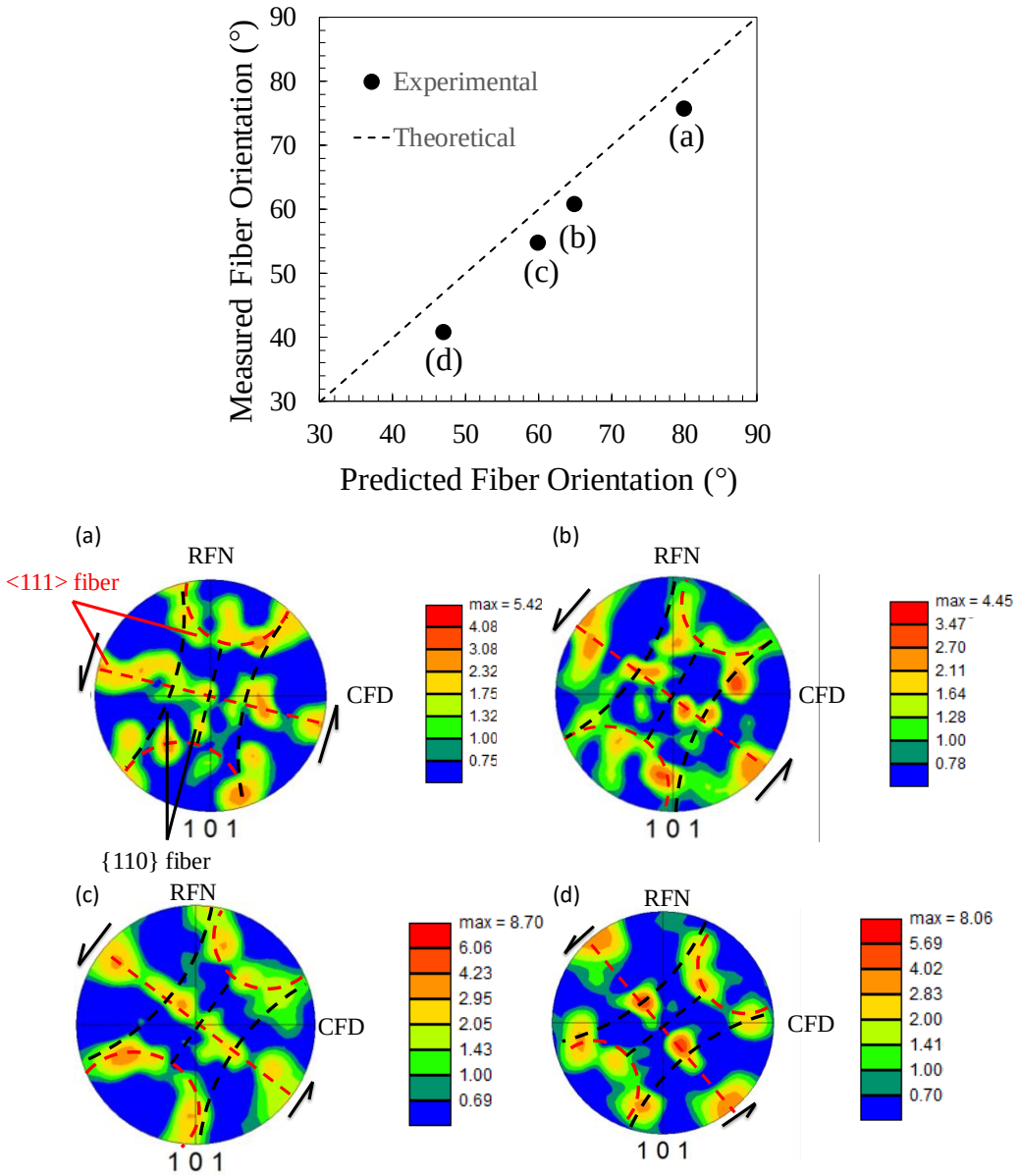

Figure 5-15 - Recrystallization (post-deformation) textures for the Fe-Si strips. The plot shows measured fiber orientations, from (101) pole figures (a-d) below, produced under various deformation conditions (λ = 1 – 2, α = 0° – 20°, V_o = 0.25 m/s – 2 m/s). The measured fiber orientations correspond closely with the (expected) orientations.

5.3.4 Texture Inhomogeneity

The texture presented thus far have corresponded to deformation conditions – large λ and high V_o – wherein the bulk of the sheet is deformed by simple shear imposed at the shear plane (primary deformation), and secondary shear effects are negligible. As was described in Section 5.2.3, when sufficient low V_o and small λ are used to produce strips, significant microstructural inhomogeneity can result. Since the strain path largely controls the textures, particularly in the present case wherein textures are retained almost exactly as predicted in the shear plane model, local texture variation in regions of the strip characterized mostly by sliding should be expected. Even in conventional machining, secondary deformation in the form of sliding is also present (Figure 5-16). Local texture measurements of an annealed condition (λ = 2, α = 20°, V_o = 2 m/s) revealed a clockwise rotation of the partial fibers, similar to the local as-deformed microstructure (not shown). The degree of inclination rotated clockwise toward the CFD from 78° in the bulk to 39° in the secondary shear zone. This rotation might be expected given the orientation of the sliding friction, which is parallel to the CFD.

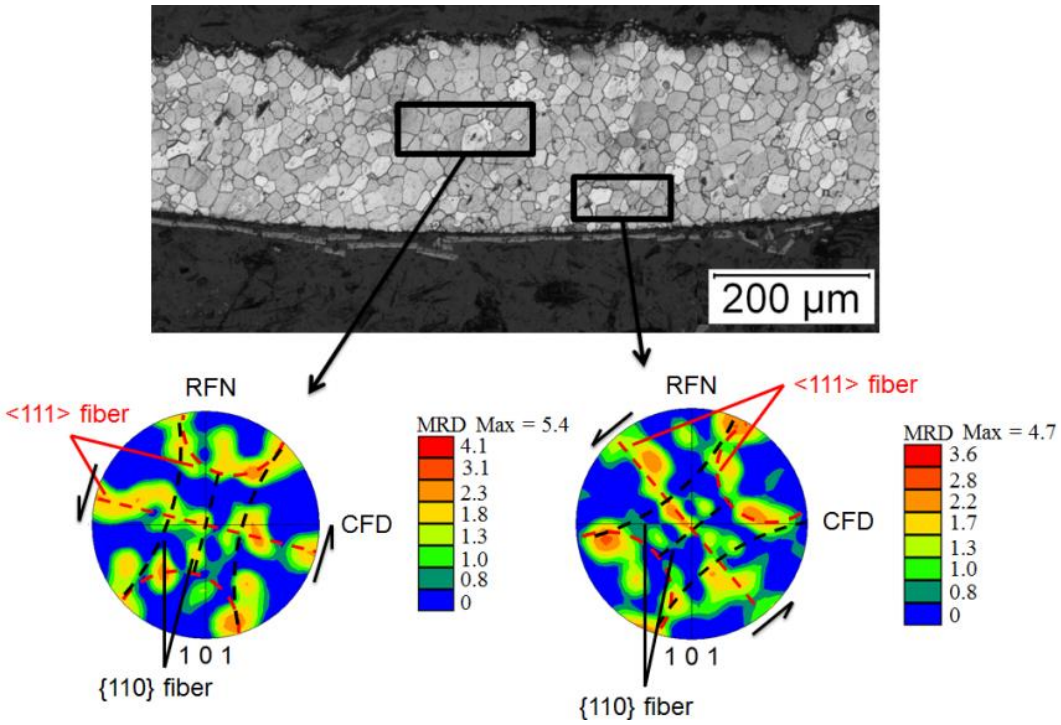

Figure 5-16 - Pole figures from the bulk (left) and secondary shear zone (right) for annealed Fe-4wt%Si following conventional machining. Textures indicate the simple shear fibers are retained following annealing.

With decreased λ and V_o, the secondary shear zone effects were significantly larger (Figure 5-10). Local texture analysis of one such sample revealed by two distinct fiber orientations, both corresponding to simple shear. In the region of the sheet far from the tool-sheet contact surface, the fibers are oriented at an angle of 41° with respect to the CFD. This texture was due primarily to the deformation occurring at the shear plane, with the fibers closely aligning with ϕ' of 47°. In the tool-sheet contact region, the fibers were aligned essentially parallel to the CFD, resulting from extreme secondary shear at the contact. Such secondary shear effects at near-surface regions are generally unavoidable in any bulk metal forming operation (e.g., rolling, extrusion) that involves die-workpiece frictional contacts. In LSEM, however, the relative extents of the secondary and primary

deformation textures can be controlled by appropriate selection of λ and V_o. As already noted, at large λ and high V_o, the primary deformation texture is described effectively by ϕ' (Figure 5-14 and Figure 5-15), and is dominant in the sheet. At the other limit, small λ and low V_o, the secondary shear deformation texture (corresponding to $\phi' = 0°$) can be expected to prevail over a large fraction of the sheet thickness. Thus by careful selection of λ and V_o, it should be feasible to effect a gradation in the sheet texture, complementing the uniformly textured sheet.

It is important to note that even in regions of sheet with significant secondary shear deformation, the deformation texture was found to be retained following annealing. A detailed examination of these regions revealed several fine grains (d ~ 15 μm) within 10° of the ideal Goss orientation. However, the intensity of these Goss-type grains was quite small, being only slightly greater than the intensity of a random texture. This is in agreement with observations from industrial practices, that Goss grains are rare in rolled sheet subjected to low-temperature annealing, conditions that induce recrystallization without significant grain growth.[72] The occurrence of Goss-type grains in the secondary shear zone is, however, significant because of possible implications for their subsequent grain growth during high-temperature annealing (if controllable).

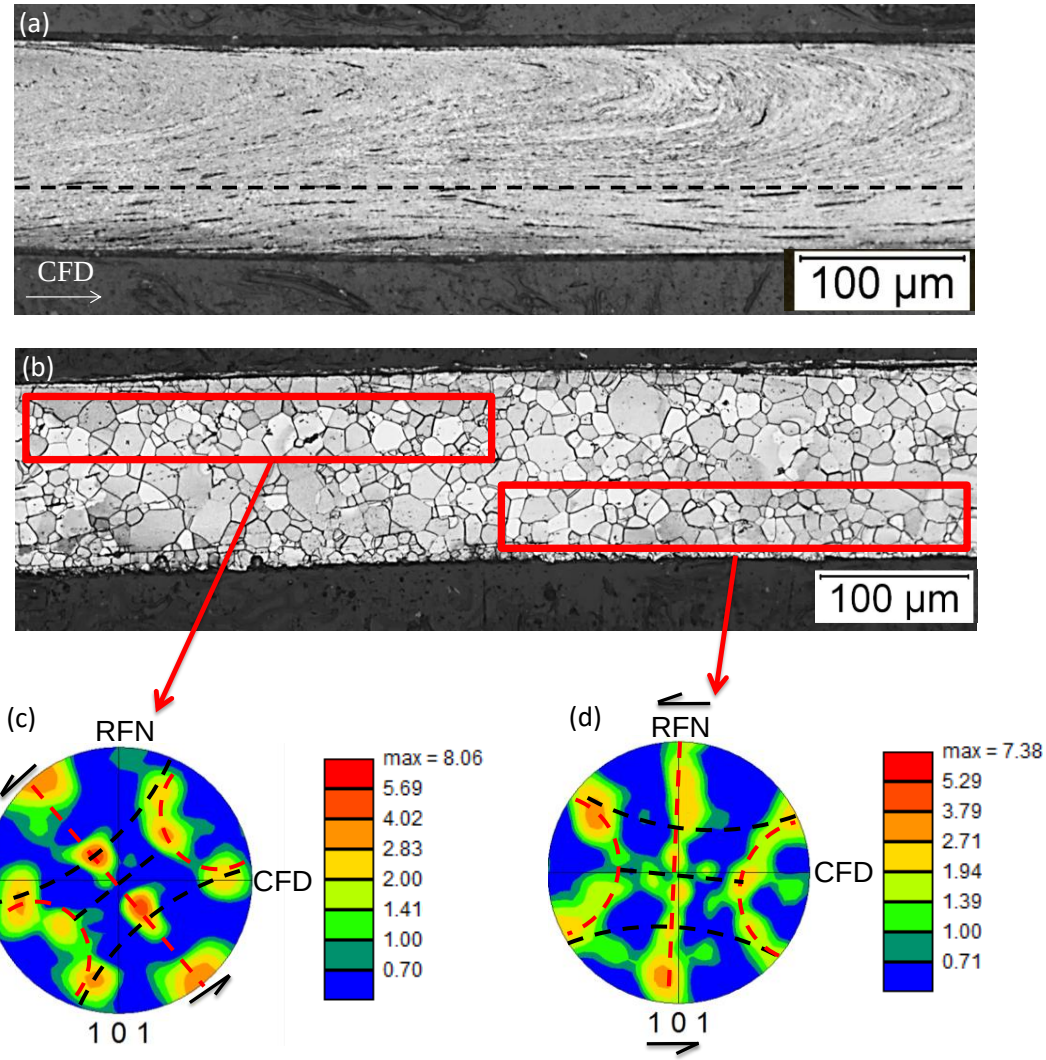

Figure 5-17 – Sheet structures showing evidence of secondary shear due to sliding at the tool-sheet (bottom) interface (α = 5°, λ = 1, V_o = 0.25 m/s). (a) and (b) are micrographs of as-deformed and annealed sheets, respectively. The dotted line in (a) represents, approximately, the boundary of the secondary shear zone. (c) and (d) show (101) pole figures of the local texture (red boxes) from the annealed condition.

5.3.5 Range of Texture Control

The retention and sharpening of the deformation texture following recrystallization suggest opportunities for controlling the texture and resulting sheet metal properties by varying the deformation conditions, combined with an annealing treatment. The texture in

the Fe-Si sheet can be well predicted from the deformation path, based on the assumption of simple shear along plane OA (Figure 3-1). The path is determined by λ and α, especially at higher V_o, where secondary shear effects at the tool-sheet interface are not pronounced. Since a range of λ and α can be accessed, a variety of simple shear textures can be achieved in the sheet. This measured range of inclination for the annealed texture fiber orientations in the present study was between 41° and 76° (Figure 5-15). It is also seen that the texture evolves as a result of the imposed strain path in such a way as to finally result in close alignment of {110} planes and <111> directions with the shear plane and shear direction, respectively.[49] Similar texture predictions based on the deformation path have also been validated for Mg AZ31B.[10]

In this correlation of the primary deformation with texture, it is important to consider extreme orientations of the accessible deformation paths (Figure 5-18). At one end, deformation conditions ($\lambda >> 1$, $\alpha > 0°$) can be selected to rotate the shear fibers counterclockwise such that the <111> fiber becomes nearly perpendicular to the sheet normal (i.e., RFN) while the {110} fiber lies nearly parallel to the transverse direction (TD). This deformation path includes, among others, a cube-on-corner and 90° rotated Goss ({110} // RFN and <001> // TD). The other extreme ($\lambda << 1$, $\alpha < 0°$) corresponds to smaller inclination angles of the shear plane and an increased secondary shear zone, leading to the development of Goss and 90° rotated Goss components. This control of crystallographic orientation presents opportunities to tailor magnetic properties, discussed in more detail as it relates to ideal magnetic textures. For example, it is deleterious to have the <111> hard magnetization orientation in the plane of the Fe-Si sheet. The LSEM shear deformation

can, however, produce sheet with a controlled <111> fiber orientation in Fe-Si that could be beneficial for targeting a broader class of applications.

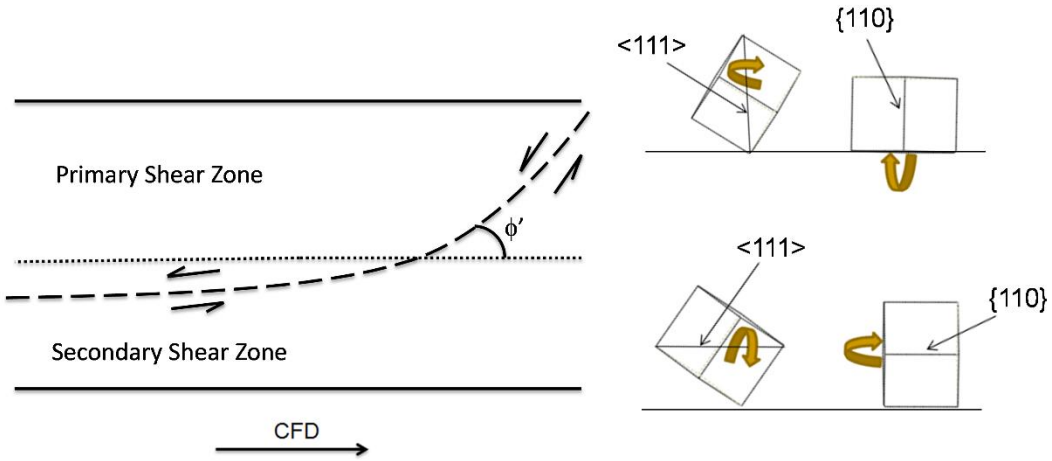

Figure 5-18 – Schematic (left) of the fiber orientations (equivalent to ϕ') in the primary and secondary shear zones viewed from the through thickness of the sheet. The extreme orientations possible in these zones are shown on the right, in terms of the <111> and {110} fiber orientations.

5.3.6 Textures in Fe-6.5wt%Si

In addition to texture control in the Fe-4wt%Si alloy, some analysis was also conducted on the Fe-6.5wt%Si strips produced from the cast ingot. For characterization, the homogeneous dynamically recrystallized strip structure was selected (T_o = 500 °C, λ = 0.95, V_o = 3 m/s, t_c = 95 μm). The observations suggest that it is feasible to produce continuous sheet, of thickness similar to that used in electrical sheet steel applications, from even Fe-6.5 wt% Si alloys by suitable design of the initial cast material microstructure and deformation parameters. The more general applicability of this process/material design

approach is supported by observations from sheet processing of Mg AZ31B[10], Ti-6Al-4V[11], and cast 5052 aluminum (unpublished).

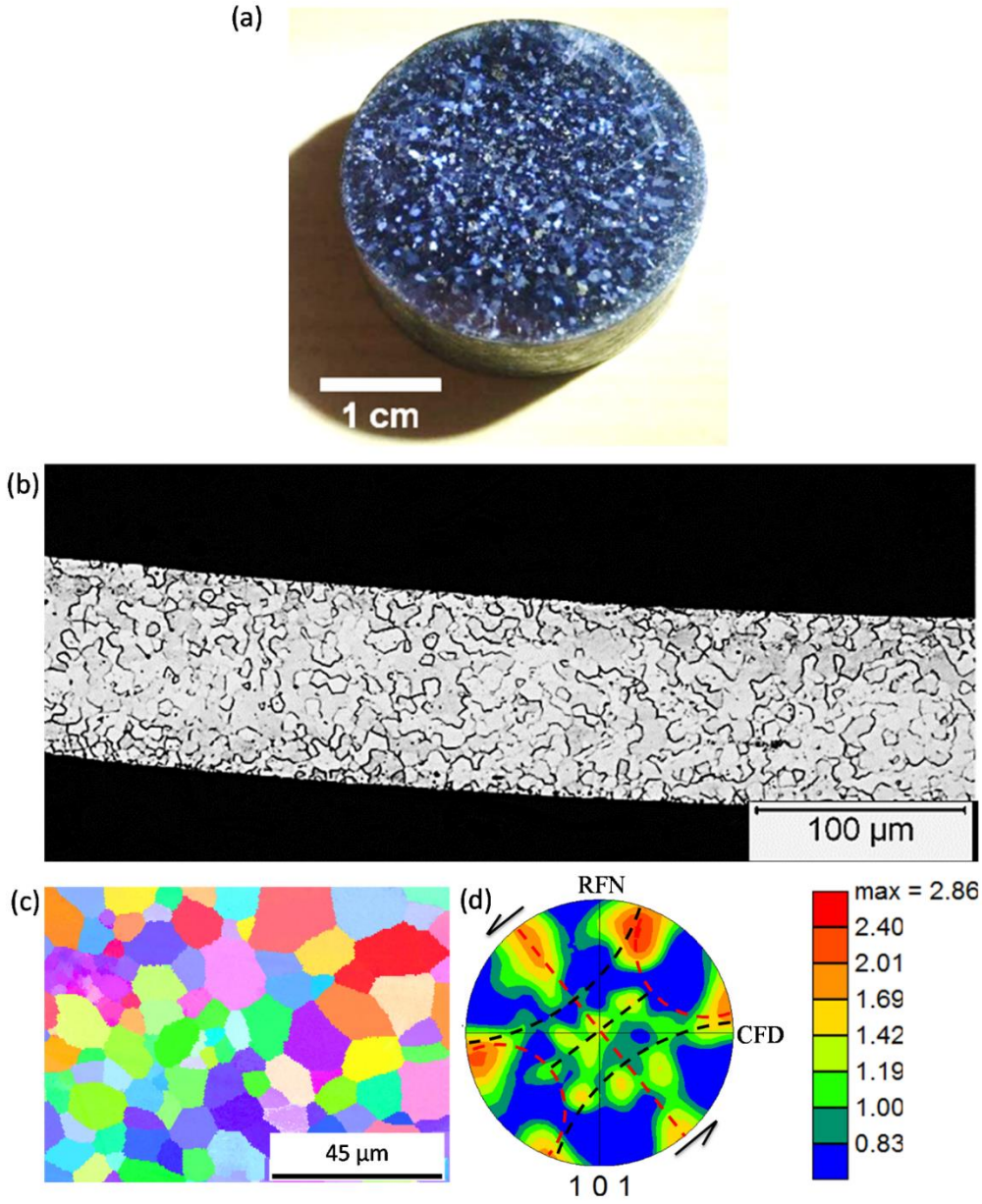

Figure 5-19 – Cast Fe-6.5 wt% Si alloy ingot cross-section (a). Optical micrograph (b) of thin (t_c = 95 µm) continuous strip produced from the ingot (λ = 0.95, α = 5°, V_o = 3 m/s, and T_o = 500 °C), and corresponding inverse pole figure map (c), showing a dynamically recrystallized microstructure with shear texture, as revealed by the (101) pole figure (d).

As with the Fe-4 wt% Si WP, sheet produced from the Fe-6.5 wt% Si ingot had a shear texture (Figure 5-19), with fibers rotated by 38° (counter-clockwise) from CFD, which again matched well with ϕ' of 46° for this deformation condition. Since similar shear-textured sheet could be produced from both rolled and as-cast (initial) WP textures, it implies that starting microstructure and texture do not significantly influence the texture in the machining of Fe-Si sheet.

5.3.7 Grain Growth Textures

As mentioned in Section 5.3.4, the large secondary shear zone of the low V_o and λ LSEM condition contained several fine Goss oriented grains within 10° of the ideal orientation. Since abnormal grain growth of Goss grains are known to be critical in developing sharply textured sheets for transformer applications, a high temperature grain growth treatment at 1000 °C for 5 h was conducted on the 4 wt% Si alloy sheet. This treatment is similar to that used to develop the Goss texture in commercial rolled sheet, where the initial stages of secondary recrystallization have been documented at temperatures as low as 850°C.[73] Following this high temperature treatment, substantial grain growth was observed, resulting in only 1-2 grains in the sheet thickness (t_c = 120 μm). However, unlike in rolled sheet, the grain growth was very homogenous with no signs of abnormal grain growth (Figure 5-20). Moreover, the texture after grain growth was reminiscent of the texture exhibited by the secondary sheared regions following recrystallization, as shown in Figure 5-20a. This observation indicates preferential growth of grains within the regions subjected to secondary shear, compared to those subjected to only primary shear deformation. This result is illustrated by the texture measurements in

Figure 5-20, where sections of the ODF (ϕ_2 = 45°) are presented for both the recrystallization (Figure 5-20a and Figure 5-20b) and grain growth (Figure 5-20c) treatments. It should be noted that the ODFs are presented with reference axes CFD and transverse direction (TD). The ODF of the sample that has undergone grain growth (Figure 5-20c) shows the same high-intensity diffraction peaks as those in the secondary shear regions (Figure 5-20b). Such a texture could only develop if grains in the regions subjected to secondary shear grew more rapidly than those subjected to only primary shear deformation, as illustrated schematically in Figure 5-20d.

The mechanism of preferential growth of grains in the secondary shear region is, as of yet, not fully understood. However, the grain growth behavior is likely related to the differences in the local grain boundary character of the two regions. Since the material subjected to additional secondary shear experiences much greater total strains, annealed grains (following recrystallization) may have developed more mobile grain boundaries than in the bulk, consequentially growing more rapidly during the high temperature grain growth treatment. Furthermore, grain size is known to influence texture development (by grain growth). However, there was no statistically significant difference in the grain size between the primary (11.7 μm ± 0.8) and secondary (11.0 μm ± 0.6) shear zones after the annealing.

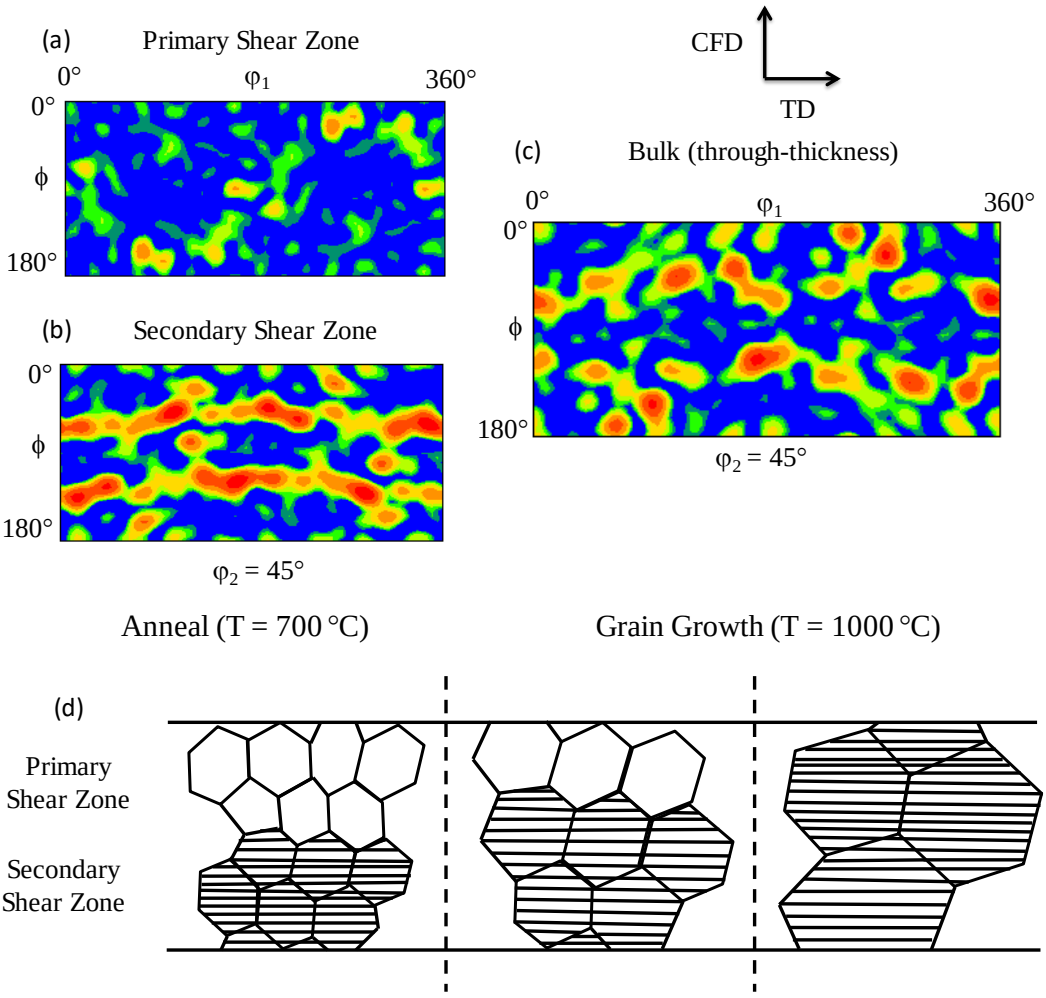

Figure 5-20 – ODFs of the primary (a) and secondary (b) shear regions of the sheet produced at slow speed (α = 5°, λ = 1, V_o = 0.25 m/s) after recrystallization annealing at 700 °C. ODF of the bulk section after high-temperature grain growth at 1000 °C, shown in (c), exhibits texture nearly identical to that of the secondary shear zone before grain growth (b). A preferential growth of grains in the secondary shear zone, suggested for this texture evolution, is illustrated schematically in (d).

5.3.8 Optimized Simple Shear Textures for Magnetic Applications

Since texture is one of the main structural contributors to optimizing magnetic properties, considering the ideal textures in simple shear deformation is important. As

mentioned previously, two types of textures are available in commercially rolled sheets. Historically, the first type of sheet texture was obtained through hot rolling deformation and is characterized by a weak (nearly random) rolling texture. These so-called non-grain-oriented (NGO) sheets, by virtue the nearly isotropic texture, has a correspondingly randomized orientation of the easy <001> magnetization directions unrestricted to the rolling plane. Therefore, applications need not consider the direction of the applied field, making NGO sheets useful in rotating electrical motor applications. However, due to the randomized <001> directions, this texture is fundamentally more difficult to saturate when compared to the ideal cube texture. When cold rolling is added, sheets develop a strong Goss texture with a well aligned <001> easy magnetization direction along the sheet length (RD). Consequentially, these grain-oriented (GO) sheets possess a more idealized magnetization situation along the length direction, where the properties essentially achieve those of the cube texture. However, when the applied field is aligned at directions that deviate from the sheet length (i.e., corners of transformer cores), the magnetic properties suffer greatly because the <001> directions are greatly misaligned with respect to the applied field. These sheets are therefore restricted to applications that take advantage of a directional applied field (e.g., transformer cores).

Both of these textures, while suitable for different applications, are fundamentally different than the tiled shear textures of machining. As described throughout the previous sections, simple shear deformation, and more precisely LSEM, demonstrated significant crystallographic texture control in a predictable manner for the two Fe-Si alloy compositions. Of interest is in controlling the textures to develop continuous sheets of Fe-Si with optimized magnetic properties. As was disclosed, the ideal crystallographic

orientation for maximized magnetic properties in Fe-Si is a texture which has a nearly isotropic distribution of the <001> crystallographic directions within the plane of the sheet. In simple shear deformation, Fe-Si textures are described by partial <111> and {110} crystallographic fibers that are inclined relative the CFD (sheet length). Generally, neither of the fibers will produce the ideal crystallographic cube texture. However, consideration of the <001> orientations with respect to an applied *H* field direction is nonetheless important. A three-dimensional unit cell model has been constructed to show the general texture character for Fe-Si following simple shear deformation (Figure 5-21).

It is important to note that the simple shear texture model shown is for one particular position along the <111> and {110} fibers. In actuality, the unit cells are rotated about the <111> direction (<111>-fiber) and the {110} plane ({110}-fiber), respectively. Therefore, description of the three <001> direction orientations is complex and furthermore based on relative strengths (intensities) of the two fibers. However, a general theoretical discussion is worthwhile as it relates to the known orientations of select <001> directions. Shown in the model are two views of the simple shear texture fibers, both from an isometric and through-thickness viewpoint. On each of the unit cells, two <001> easy magnetization directions are superimposed. Clearly, the unit cells are inclined relative to the sample axes and the degree of inclination is determined by the deformation parameters, i.e., Equation 3.3. The essential feature of this type of texture is that the <001> directions are also inclined relative to the CFD. If a field is applied along this direction, then it is expected that these inclinations would require additional applied field to accomplish full saturation compared to the well-textured GO sheets and ideal cube textures.

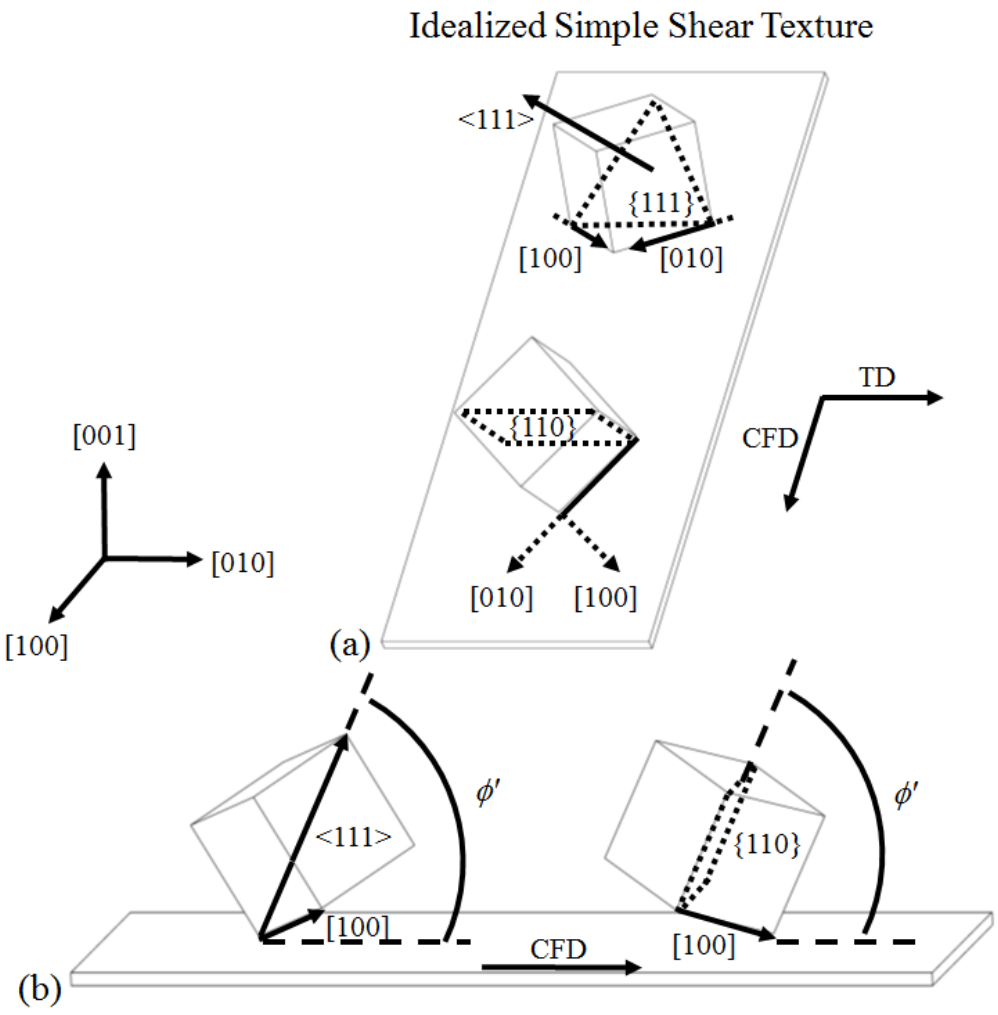

Figure 5-21 – Unit cell model for the simple shear textures developed by machining. Unit cells shown here illustrate the orientation of the <001> directions, which are inclined out of the plane of the sheet. Note, this is one specific location along the texture fibers, as the full texture is described by rotating the unit cells about the <111> and {110}, respectively.

The amount of applied field required to saturate a given texture is a function of the orientation of the <001> easy magnetization directions with respect to the applied *H* field the direction. As an example, consider an applied field parallel to the CFD. For the given texture orientation in Figure 5-21, which is defined by having two <001> directions oriented symmetrically at 45° angles from the CFD direction, the orientation of the <001>

directions with respect to the field direction have been calculated. The results are plotted for the three <001> directions (defined by the reference axes in Figure 5-21) as a function of the shear plane angle in Figure 5-22. Note, this orientation is a specific location along the texture fiber and a full description of the necessary <001> orientation angles would require consideration of the full fibers, i.e., full rotations about the <111> and {110}.

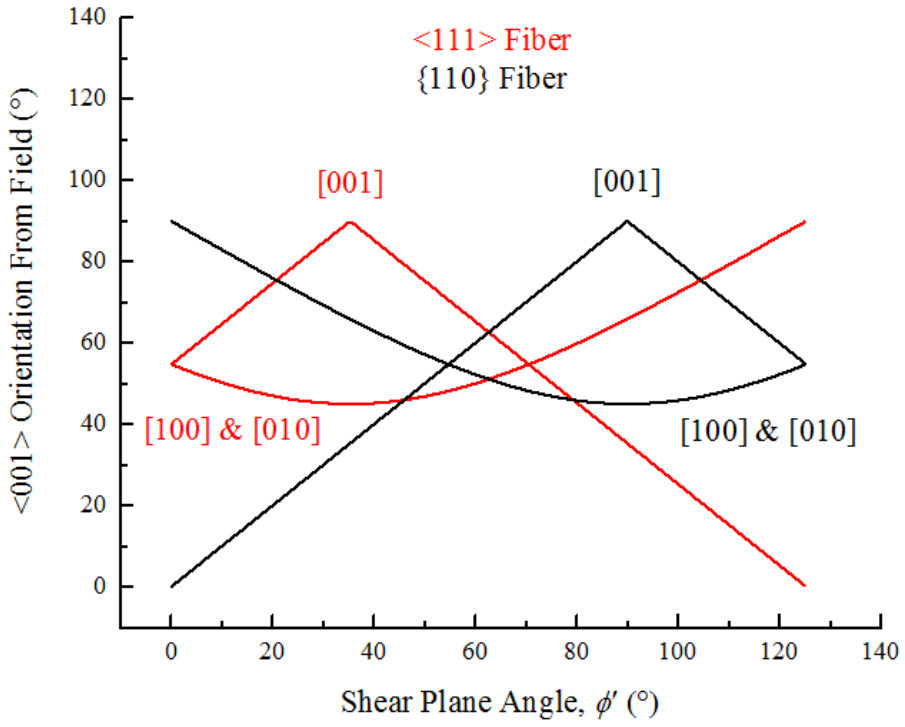

Figure 5-22 – Plot showing the orientation of the <001> directions with respect to the applied *H* field along the sheet length as a function of the shear plane angle. Note, this represents one specific orientation along the fibers. A full description would consider rotation about the respective <111> and {110} for the two fibers. The orientation of the <001> directions is a function of both the particular fiber and shear plane angle.

From Figure 5-22, the orientation of the <001> directions with respect to the field direction is shown to vary significantly as a function of the shear plane angle for the two simple shear fibers. Consequentially, improving properties in shear textured Fe-Si must consider both the relative volume fractions of the {110} and <111> fibers and the shear

plane orientation. Of particular interest is the <001> orientation angles as the shear plane angle approaches 0°, i.e., a secondary shear fiber orientation. The unique [001] direction of the {110} fiber would then also be 0°, which is a result of an ending Goss orientation (see Section 5.3.5). Interestingly, at this low shear plane angle, the {110} fiber in fact possesses a Goss orientation that rotates about the (110) plane (about the surface normal), leaving a distribution of [001] directions in the plane of the sheet. While this is not the same as a true cube-type texture, it does indicate that there exists a shear plane orientation such that the {110} fiber contains a series of [001] directions in the plane of the sheet – a potential 'Goss fiber'. Furthermore, high temperature annealing treatments were found to induce preferential grain growth of regions with a significant secondary shear texture. It is interesting to hypothesize the resultant magnetic properties of a strip with a simple shear texture having a 0° inclination with a large volume fraction of orientations from the {110} fiber. Perhaps sheets could be produced with nearly ideal magnetic properties for rotating electrical motors by virtue of a Goss fiber texture, rather than a strong cube texture.

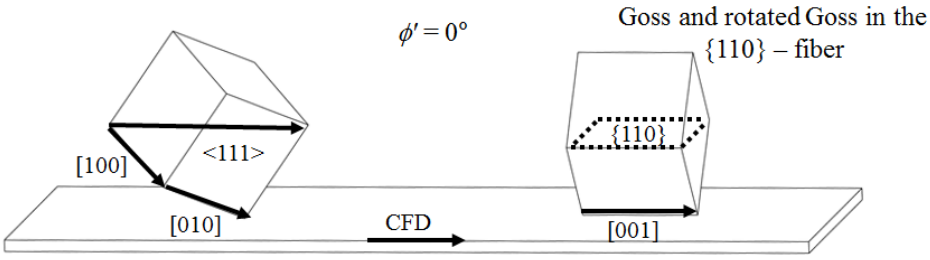

Figure 5-23 – Side view of unit cell orientations for a shear plane angle, ϕ', of 0°: (left) the <111> fiber, (right) the {110} fiber. Note, the texture components are fibers rotated about the <111> and {110}. At this shear plane angle, a rotated Goss fiber could theoretically result in the {110} fiber to create a distribution of <001> directions in the plane of the sheet. Such a texture might hold promise for improving properties.

5.3.9 Summary

Continuous strips from Fe-Si alloys were produced using single step simple shear deformation. Through processing-microstructure maps, combinations of V_o and T, could be utilized to develop a range of microstructures, varying from those of homogeneous and severely shear localized structures of conventional machining to the homogeneous structures of LSEM with a dynamically annealed grains. These same attributes, in combination with high hydrostatic pressures, showed to produce similar microstructures in continuous strips from cast Fe-6.5wt%Si. Additionally, a range of crystallographic textures could be developed in a predictable and controlled manner, which were found to be retained following recrystallization and grain growth treatments. A theoretical analysis of the simple shear texture was provided and particular texture orientations for magnetic applications were proposed. In the next chapter, an analysis of the recrystallization kinetics for machined and rolled Fe-Si is provided to elucidate the texture retention noted above.

CHAPTER 6. TEXTURE EVOLUTION

This chapter is devoted to the study of the recrystallization (post-deformation) mechanisms believed to contribute to the observed retention of the deformation textures in Fe-4wt%Si following simple shear deformation. Two main sections are discussed. The first provides a brief background on recrystallization theories and kinetics. Section 2 details the experimental results of isothermal annealing experiments for machined and rolled Fe-4wt%Si. Evolution of the microstructure is shown and the recrystallization kinetics, as measured through micro (Vickers) hardness evolution, is related to classical JMAK recrystallization kinetics.

6.1 Recrystallization Theories

6.1.1 Overview of Annealing Processes

Recovery and recrystallization are competing thermodynamic processes that, together, are responsible for removing stored energy in a metal following metalworking to achieve equilibrium microstructures.[74] While both are thermodynamically driven to decrease the free energy in a cold-worked metal or alloy, each is unique both in terms of the kinetics and corresponding microstructural changes. Schematically, the annealing processes involved are summarized in Figure 6-1 for classical (discontinuous) recrystallization. Recovery (Figure 6-1b), which precedes recrystallization, is considered a homogeneous (continuous) process characterized as a so-called Gibbs II transformations,

where atomic-level changes occur uniformly in the deformed material microstructure to reduce the material free energy. Distinctly, this happens without the motion of grain boundaries, most commonly through the removal of both point defects and dislocations.[74] In plastic deformation, the annihilation of point defects is negligible and recovery mostly concerns the behavior of dislocations, which undergo mutual annihilation or rearrangement into lower energy configurations through glide, cross slip or climb.[74] A common example of such low energy structures is that of low angle subgrains. These low angle subgrains, created by the rearrangement of dislocations, possess orientations less than 10° from one another. Since the motion of dislocations occurs on the atomic level, in-direct measurements are often required to identify the degree of recovery (e.g., mechanical and electrical property measurements) and the microstructural changes involved are considered uniform, occurring throughout the entirety of the parent material at the same rate. The microscale nature of the recovery processes usually results in a retention of the intrinsic elongated grain structures that were developed during deformation (Figure 6-1b).

Under most deformation strains (> 5%), recovery alone is insufficient to remove the stored plastic energy and therefore recrystallization occurs. Unlike recovery, recrystallization is significantly more discontinuous, being classified as a Gibbs I type transformation, notably for the non-uniformity and large magnitude of microstructural changes. Recrystallization is defined as the emergence of new high angle grains (misorientations > 15° between grains) which have formed to remove the remaining stored plastic energy in a cold worked metal following recovery (Figure 6-1c). Drastic microstructural changes then occur in the metal *via* unstrained (lower energy) material consuming the original (parent) material in the as-deformed state. This occurs until the

deformation microstructure is entirely consumed by the lower-energy annealed structure (Figure 6-1d). This is distinctly different than (normal) grain growth, a process in which high angle grains grow nearly homogeneously to reduce the total grain boundary free energy.

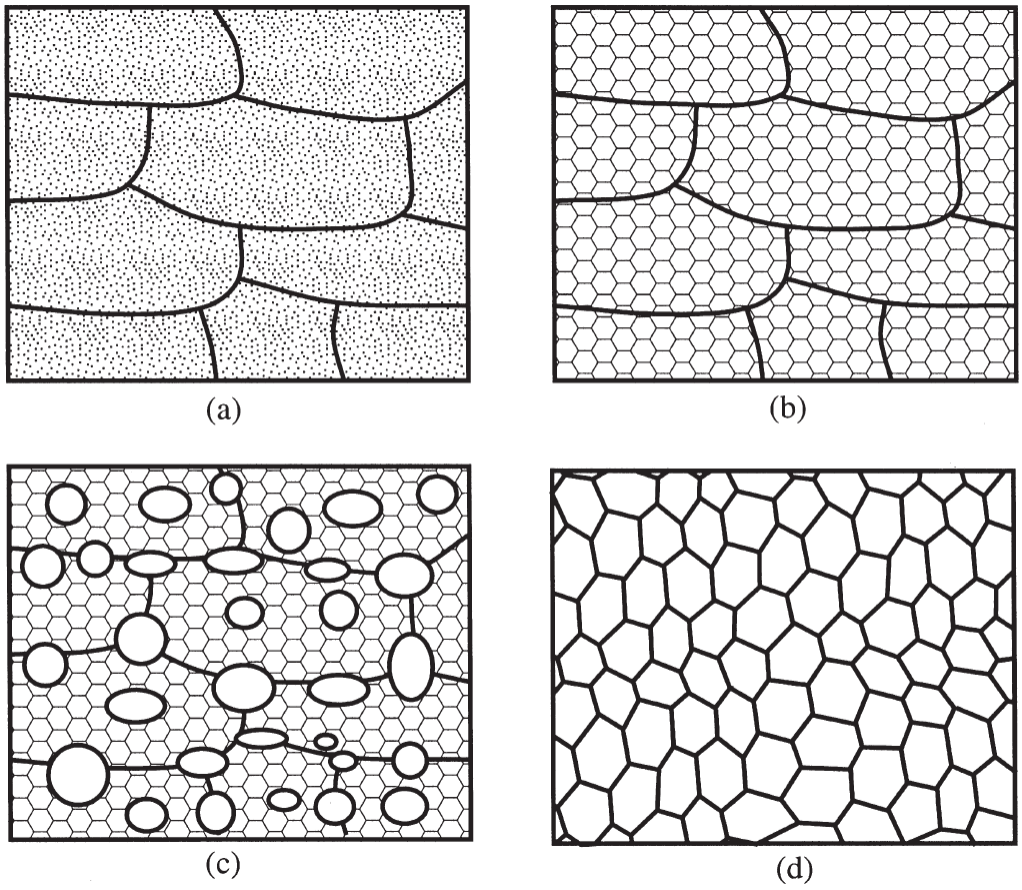

Figure 6-1 – Schematic of microstructural evolution during annealing of a deformed material: (a) as-deformed state, (b) recovery, (c) partial (discontinuous) recrystallization, (d) fully annealed state (after [75], with permission of Elsevier).

Conventional theory suggests that recrystallization processes remove the stored energy in two distinct mechanisms of nucleation and (subsequent) growth. In this theory,

grains first nucleate in the deformation structure with high angle grain boundaries and then grow into (consume) nearby regions of high stored energy through grain boundary migration.[74,75] In this definition, it has been found that nucleation is not an atomic level event as in the case for nucleation of solid from a liquid melt during solidification processes. Rather nucleation in recrystallization occurs from the local growth of unstrained (recovered) material in the deformation structure. These local nuclei develop and grow as high angle grain boundary regions in an otherwise recovered substructure (e.g., low angle subgrains). Growth continues largely unabated until the boundary of the growing nuclei (grain) encounters another. While the nuclei develop in the deformation structure, the deformation texture character is not necessarily retained. In fact, recrystallization textures can be entirely different than those of the as-deformed state.[69] The problem then is identifying what types of texture components prevail and why.

In general, nucleation of grains during recrystallization occur along particularly favorable sites of the as-deformed structure. Five general types of nucleation sites have been identified and include: 1) pre-existing grain boundaries (high angle), 2) deformation bands, 3) near precipitates, 4) shear bands and 5) throughout heavily deformed materials.[75] Since the nucleation does occur from regions of the parent deformation structure, some aspects of the deformation texture might be expected to be retained in a fully recrystallized structure. However, the inhomogeneous nature of the nucleation process prevents a full retention of the deformation texture character and instead only certain orientations from the as-deformed state remain after annealing. Furthermore, grains of entirely unique orientation can develop for fundamentally different recrystallization textures. This is perhaps expected considering that the probability of finding some

favorable nuclei to grow during recrystallization in a conventionally deformed substructure is extremely rare, ~ 1 out of 10^6 subgrains. This low probability, in turn, also dictates the kinetics of the conventional recrystallization processes.

Recrystallization processes described above have been classified as so-called discontinuous recrystallization (dRX). The term discontinuous is used because the nucleation and growth of the fine nuclei occurs only in particular regions of the microstructure.[74] Furthermore, the recrystallization in obvious with distinct nucleation events of annealed grains growing into a deformed structure. In most deformation processes (e.g., rolling, drawing, extrusion), dRX is the dominant mode of recrystallization. However, some deformation techniques are capable of imposing large strains to develop comparatively unique substructures. These techniques, so-called severe plastic deformation (SPD) processes, refine the original material microstructure into one containing many subgrains with a larger portion of high angle grain boundaries compared to conventional deformation processes. These ultrafine grain (UFG) structures are fundamentally different than the low angle substructures that result from conventional processing and are developed either through the gradual application of strain or catastrophically through grain ‘fragmentation’. Since these UFGs contain a higher volume fraction of high angle grain boundaries in the substructure, the response to thermal treatments is significantly different and more homogeneous than conventional dRX. Because of the high angle substructures, the UFGS of the substructure can be considered as favorable nuclei to grow throughout the entirety of the sample homogeneously, a process coined as continuous recrystallization (cRX). Because many more nuclei are active during recrystallization, retention of the deformation texture character is necessary, unlike dRX in

which different texture components can nucleate to present entirely different recrystallization textures.

Textures measured for the Fe-Si specimens here reflect a behavior expected in cRX. This is perhaps not surprising, considering that the large strains and temperatures of machining are known to develop microstructures with distinct UFGs.[10,53] However, texture retention alone is insufficient evidence for identifying the cRX mechanism. Because dRX and cRX are governed by fundamentally different physical processes, comparing the recrystallization behavior of rolled and machined Fe-Si should allow for a quantitative description of the annealing differences.

6.1.2 Overview of Recrystallization Kinetics

The rate (kinetics) of recrystallization is a function of both time and temperature of the annealing treatment for a given plastic strain, material composition and structure. Classically, recrystallization kinetics can be determined using a variety of characterization methods, including diffraction (EBSD, neutron), calorimetry, microscopy and mechanical/electrical property analysis.[75] From such analysis, recrystallization kinetics are commonly reported as fraction recrystallized against time, where the natural shape is often identified as sigmoidal (Figure 6-2).

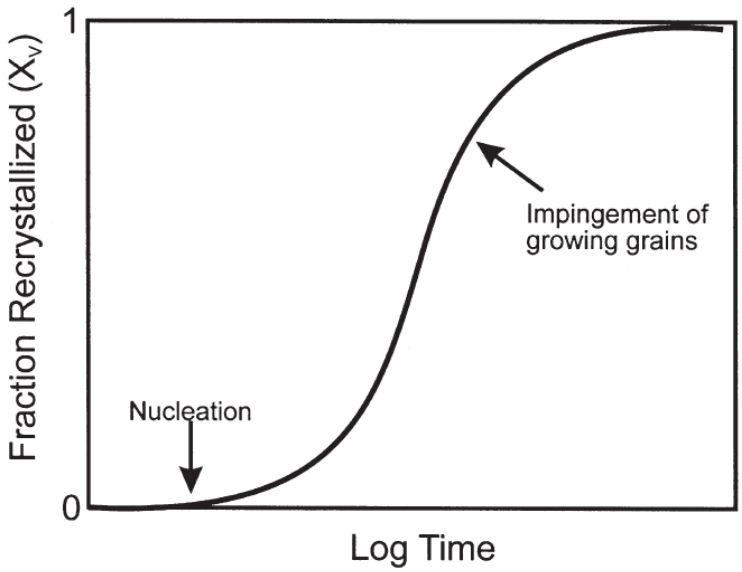

Figure 6-2 – Classical sigmoidal plot of fraction recrystallized vs. log time commonly used to document the recrystallization process and kinetics (after [75], with permission of Elsevier).

The shape of the recrystallization curve is a result of the various metallurgical phenomena (i.e., nucleation and growth) occurring within a metal structure during annealing. Early pioneering work of Kolmogorov, Johnson, Mehl and Avrami led to the first quantitative models used to mathematically characterize the kinetics of the annealing processes, cumulatively termed as the so-called JMAK model.[76] This model assumes: 1) nuclei develop randomly within the microstructure at some constant rate, 2) the growth is isotropic and 3) the growth rate is constant, yielding the following:[76,77]

$$X_v = 1 - \exp(-Bt^n) \tag{6-1}$$

where X_v is the volume fraction recrystallized, B is a constant, t is time at temperature and n is the JMAK (or Avrami) exponent. While the JMAK model is generally considered too

simple to accurately capture all the phenomena of annealing processes, it is convenient to use to identify differences in recrystallization behavior. From the JMAK model, a so-called JMAK plot can be created by plotting $\ln(\ln(1/(1-X_v)))$ against $\ln t$, the slope of which is the Avrami exponent, n. An example of JMAK plots is shown for copper in Figure 6-3. Theoretically, Avrami exponent values of 4 should be measured for 3-D growth of recrystallization nuclei at random nucleation sites. However, typical reported values are less than 4, suggesting that the assumption of random nucleation sites is not accurate for most deformation structures. In spite of this, meaningful comparisons can be drawn between different samples by discussing avrami-based recrystallization kinetics.

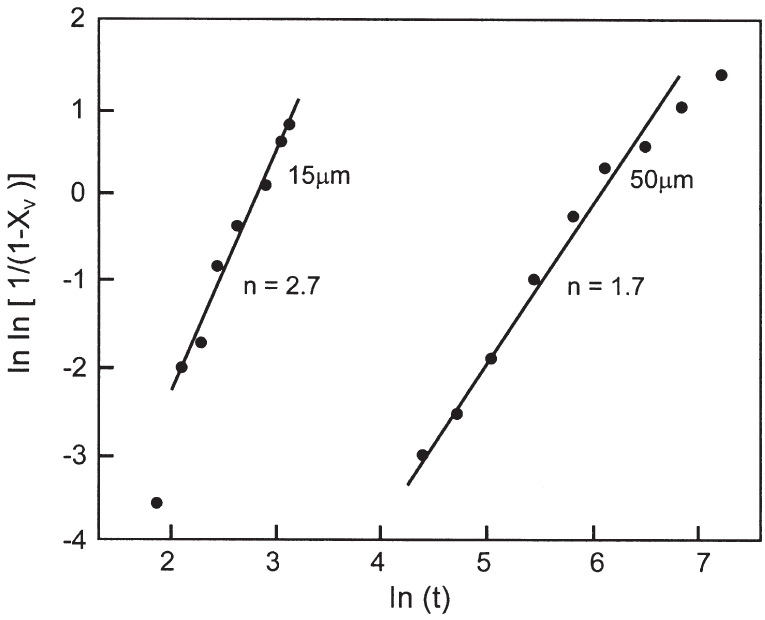

Figure 6-3 – JMAK plot for two different copper samples. Note, the slope of the data represents the Avrami exponent (after [75], with permission of Elsevier).

6.2 Fe-Si Microstructure Results

6.2.1 Rolling Experiments

In general, texture development in both the NGO and GO sheets of Fe-Si is complex, where the particular texture components that develop, the respective intensities and degree of texture inhomogeneity are all a function of the particular stage in the commercial rolling processing.[35] However, clear discontinuous type recrystallization is most commonly observed in the commercial rolling process. In an effort to reproduce the typical commercial recrystallization behavior, the Fe-4wt%Si plate was subjected to two distinct stages of rolling both at a 70% reduction separated by a 700°C intermediate annealing for 4 hours. Similar two-stage cold rolling is common in commercial processing of Fe-Si sheet. The results are summarized in the series of optical micrographs of Figure 6-4.

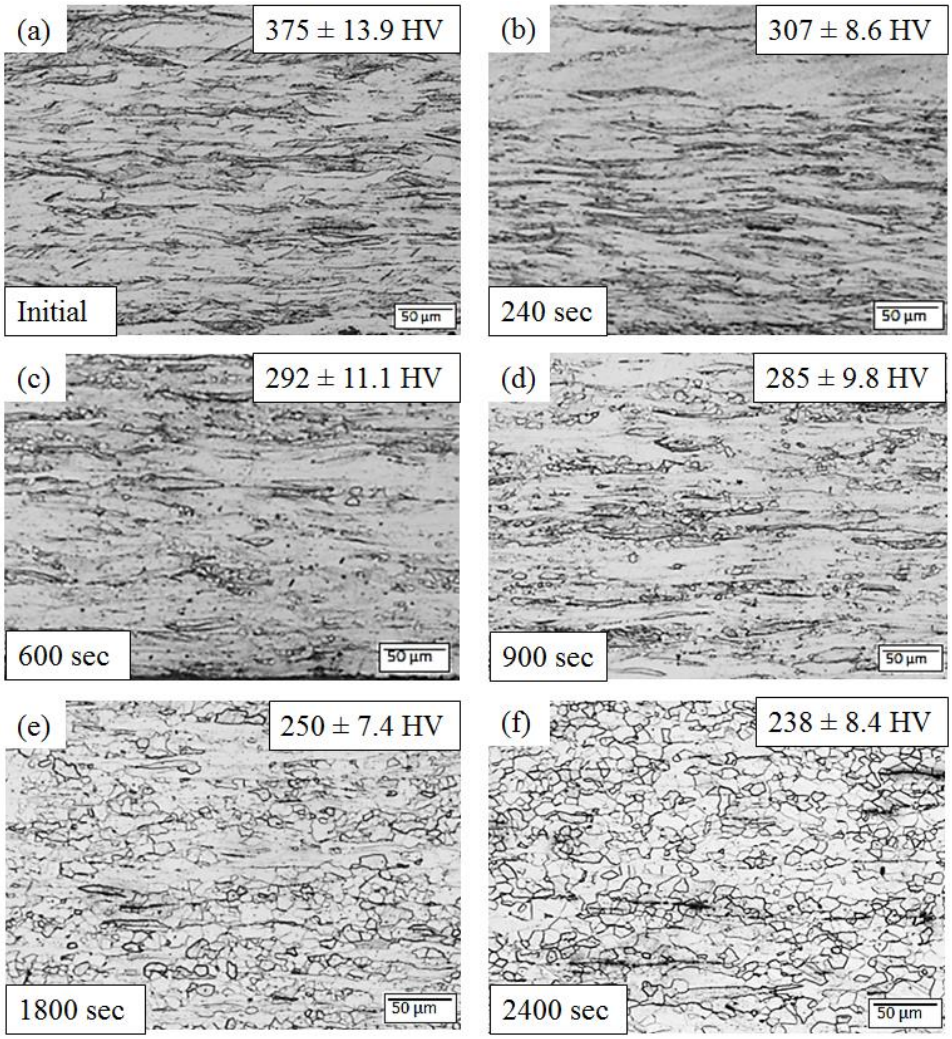

Figure 6-4 – Isothermal incremental annealing experiments for the two-stage cold rolling of Fe-4wt%Si material. Annealing was performed at 700°C in an open air box furnace at various times (in seconds) of: (a) 0 (as-deformed), (b) 240, (c) 360, (d) 600, (e) 1800, (f) 2400.

As expected in rolled Fe-Si sheet, the microstructure following the second stage rolling (Figure 6-4a) possessed a classical cold-worked structure with grains elongated in the rolling direction and a correspondingly high hardness of ~375 kg/mm^2. Such a microstructure and hardness are perhaps expected for the 70% rolling reduction used ($\bar{\varepsilon}$ ~ 1.2). Of particular interest is the homogeneity of the deformation structure, which

essentially revealed no signs of significant secondary shear deformation at the surfaces nor any signs shear bands. After the first annealing experiment, a similar, homogeneous deformation structure was observed (Figure 6-4b), despite being annealed for 4 minutes (240 sec) at 600°C. However, a sharp drop in hardness was observed (307 kg/mm^2), representing nearly an 18% decrease from the initial as-deformed condition. Note, no visible recrystallization nuclei were present and therefore the hardness drop is believed to be solely the result of recovery processes, as outlined in Section 6.1.1. In fact, recrystallization nuclei were not observed until the annealing was performed for 10 min (600 sec), at which point the initial stages of recrystallization were observed optically (Figure 6-5c) with a corresponding decrease in hardness (292 kg/mm^2). In agreement with conventional recrystallization theory, these nuclei mostly appeared along previous high angle grain boundaries of the deformation structure, which are known to be favorable nucleation sites for recrystallization. Additionally, the nuclei were extremely small, $d < 10$ μm, indicating limited growth. This nucleation continued after annealing for 15 min (900 sec), where a larger portion of the deformation structure was consumed by the fine annealed nuclei (Figure 6-4d) and a slightly reduced hardness (285 kg/mm^2) was measured.

During the last two time intervals of 30 (1800 sec) and 40 min (2400 sec), a significant change in the deformation structure was observed, where both the volume fraction and size of the recrystallization nuclei increased (Figure 6-4 e and f). This microstructural change was accompanied by a substantial decrease in hardness. At these longer annealing times, recrystallization was rampant throughout the structure and the final state (Figure 6-4f) revealed a fully annealed structure with a grain size $d \sim 15$ μm and

hardness of 238 kg/mm^2. Metallographic and hardness analysis of additional time at temperature revealed no noticable change (not shown).

As a whole, the incremental annealing experiments of rolled Fe-Si suggest a discontinuous type recrystallization mechanism, where, with increasing time, recovery occurred (Figure 6-4b) followed by extended periods of nucleation (Figure 6-4c and d) and subsequent growth (Figure 6-4e and f) of annealed grains. As such, crystallographic textures are therefore expected to not be fully retained, which has been documented previously for various stages of the Fe-Si commercial rolling process.[35]

6.2.2 Metal Cutting

To compare with rolling, both a conventional machining and LSEM condition were selected for recrystallization studies. The machining parameters (λ and α) were selected to impose similar deformation strains to those used during rolling without significant shear banding (i.e., $V_o < 4$ m/s). First discussed is the conventional machining results, which are summarized in Figure 6-5.

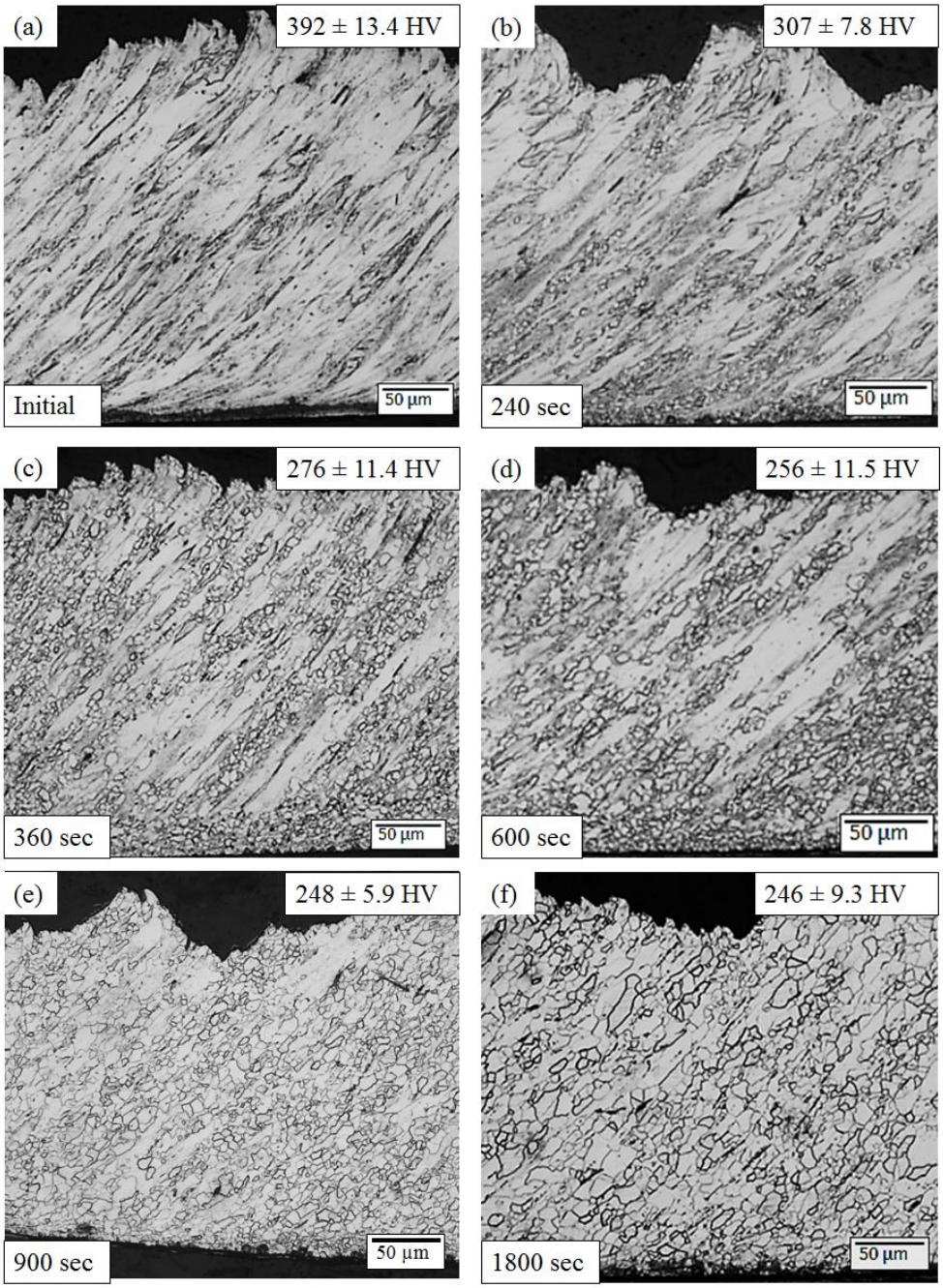

Figure 6-5 – Isothermal incremental annealing experiments for conventional machining of Fe-4wt%Si material. Annealing was performed at 700°C for (in seconds): (a) 0 (as-deformed), (b) 240, (c) 360, (d) 600, (e) 900, (f) 1800.

The as-deformed microstructure possessed heavily sheared grains inclined with respect to the chip flow direction, the angle of which is related to the deformation parameters (Figure 6-5a). For the free machining (FM) case, λ ~1.7 and α = 0°, corresponding to $\bar{\varepsilon}$ = 1.3. This large strain led to a hardness of 392 kg/mm^2, which is within 5% of the initial hardness of the rolled condition (375 kg/mm^2), indicating a similar level of deformation was imposed between the two processing methods. Interestingly, at the first annealing time of 4 min (240 sec) – the same time interval for rolling – several recrystallization nuclei were observed and a significant drop in hardness (307 kg/mm^2) was measured (Figure 6-5b). The degree of softening was, in fact, very similar to the rolling case, representing a decrease of ~ 22%. The essential difference, however is the appearance of recrystallization nuclei in the deformation structure of the FM condition. Nucleation appeared to occur primarily along the narrow secondary shear zone of the chip, in addition to several dispersed throughout the bulk. Similar to the rolled condition, nuclei in the bulk appeared to emerge along grain boundaries of the deformation structure and were quite fine (d ~ 5 μm). This nucleation continued throughout the next three incremental annealing times (Figure 6-5c-e) with rapid decrease in hardness, resulting from an increase in both the volume fraction and size of the annealed nuclei. After ~15 min (900 sec), a fully annealed hardness was reported and metallographic analysis revealed that a majority (~95%) of the specimen cross-section was consumed with larger (d ~ 10 μm) nuclei, which slightly increased in size at the 30 min interval for d ~ 15 μm (Figure 6-5f).

Annealing behavior for the LSEM condition was similar to the conventional machining case (Figure 6-6). However, as a whole, the recrystallization occurred more homogeneously and rapidly, which is perhaps expected given the application of a constraint

to confine the deformation. The initial deformation showed a significantly refined flow-line type structure and the presence of a significant secondary shear zone, which was noted previously to also retain texture following recrystallization (like the primary shear zone, see Section 5.3.4). The confinement of the deformation promoted an overall higher as-deformed hardness, which was 448 kg/mm^2.

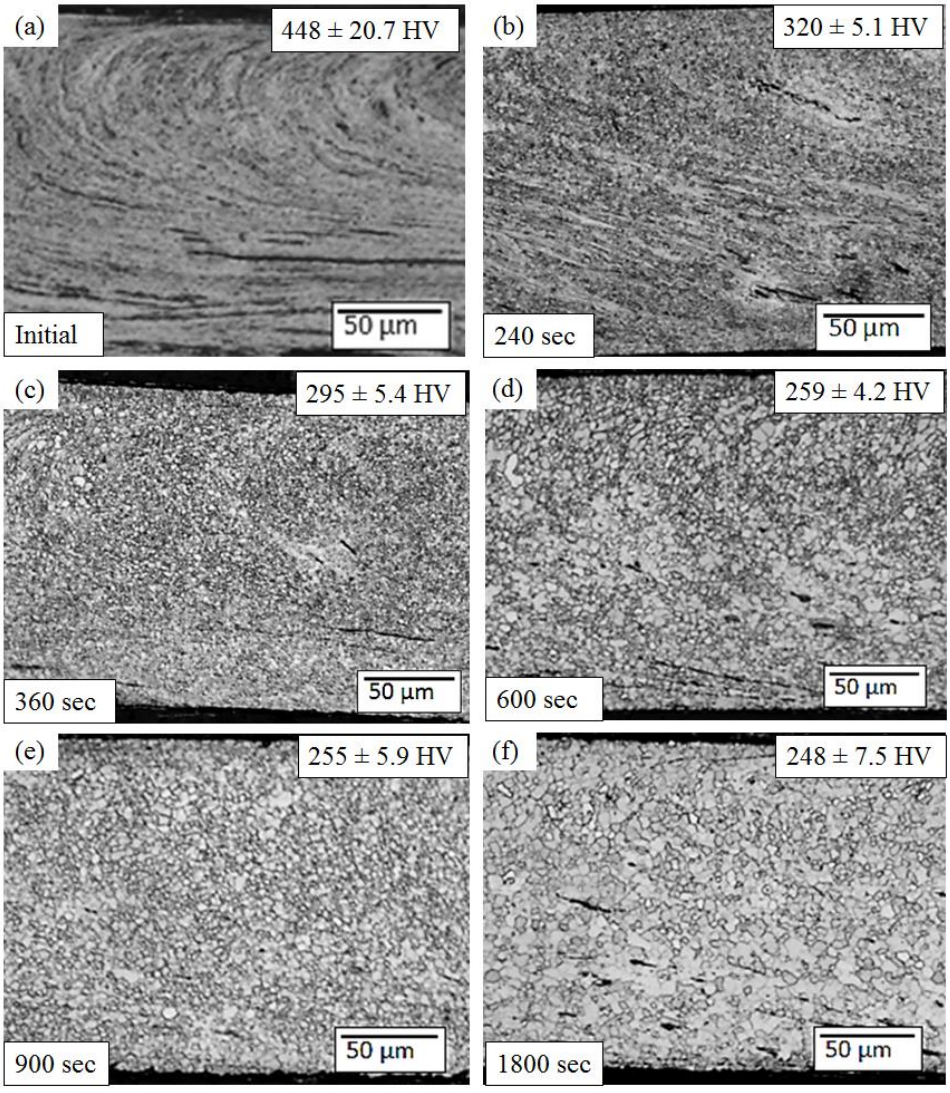

Figure 6-6 – Isothermal incremental annealing experiments of LSEM specimens for (in seconds): (a) 0 (as-deformed), (b) 120, (c) 240, (d) 600, (e) 600, (f) 900.

Following the first recrystallization treatment interval of 4 min (240 sec), recrystallization began to appear in the deformation structure and a large hardness drop of ~ 29% was noted. This recrystallization continued until the entire structure was dominated by fine nuclei homogeneously distributed throughout the deformation structure, requiring only 6 min (360 sec) at temperature. The annealed grain size after 6 min was significantly small, $d \sim 1\ \mu$m, and a relatively high hardness remained (295 kg/mm^2). With additional annealing times, the grain size increased fairly rapidly (and homogeneously) and the associated hardness also rapidly decreased until after 15 min (900 sec), at which point the grain size was $d \sim 10\ \mu$m and the hardness decreased to the annealed softness (255 kg/mm^2). Note, additional time at temperature increased the grain size and decreased the hardness slightly (Figure 6-6f).

6.2.3 Microstructural Comparison

As a whole, significant differences in the recovery and recrystallization behavior were noted between the machined and rolled specimens. The first distinct difference was the amount of time of recovery that preceded the onset of initial recrystallization. In the case for the rolled specimen, compared to the two machining cases, a near 2.5-fold increase in time was required at temperature before optically visible signs of the onset of recrystallization (i.e., incubation period) could be seen (i.e., 600 sec vs. 240 sec). It is important to note, that the optical micrographs can have limits in detecting the very end of the incubation period (i.e., beginning of nucleation). In fact, microhardness analysis of the machining conditions revealed that recrystallization onset time was actually closer to 120 sec. This was identified by constructing JMAK plots for the entire isothermal annealing

history and determining the cross-over between the two slopes to indicate recovery and recrystallization (see Figure 6-7). Consequentially, it is this time that was used as the zero recrystallization fraction for the subsequent Avrami analysis.

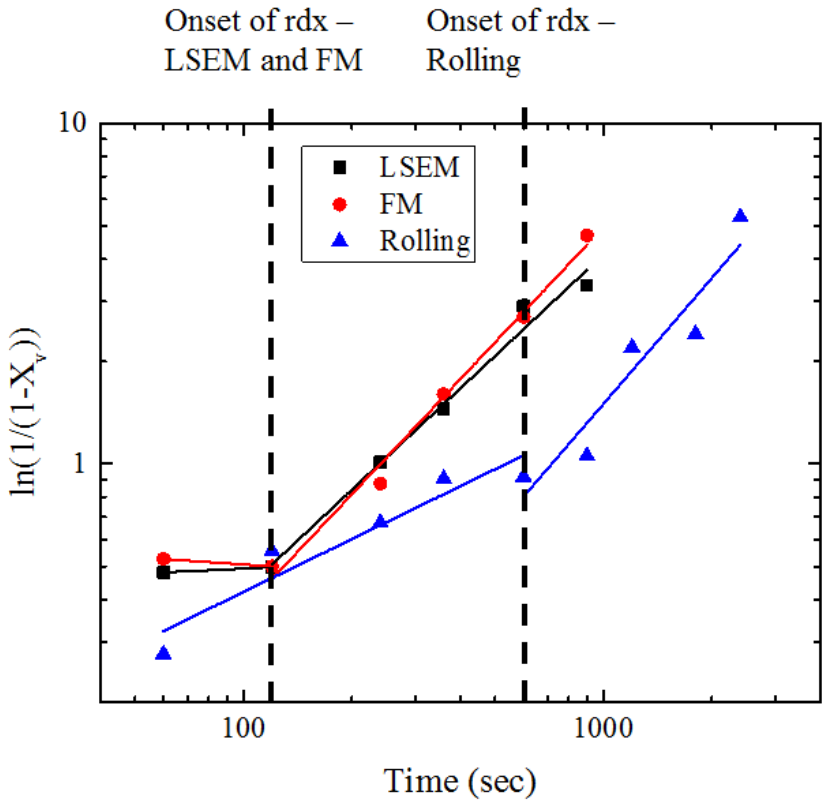

Figure 6-7 – JMAK plot showing by regions of recovery and recrystallization for the Fe-Si samples. Analysis here revealed two distinct slopes, one defining recovery (shallow slope) and the other recrystallization (steep slope). Recrystallization is believed to have begun at ~120 sec for the machined samples, despite lack of evidence optically, while rolling was ~600 sec.

The second major distinction was the amount of time required to complete full recrystallization. For the rolled condition, the time at temperature required was ~2400 sec. By comparison, the machining conditions required 900 sec (FM) and 600 sec (LSEM),

respectively. Disparities in both the extent of recovery and the required time for recrystallization can be related to the fundamental microstructure differences that result from the two different processing routes. Typically, in rolled sheet, a majority of the deformation substructure consists mostly of diffuse dislocation boundaries and/or low angle subgrain boundaries, which must rearrange into lower energy configurations prior to the nucleation and growth of recrystallization nuclei.[69,70] Furthermore, the relatively low mobility of the low angle substructures that form during rolling limit the nucleation and growth rates during annealing. This is unlike machining which, by virtue of its single step, high temperature and large strain characteristics, has been shown to develop deformation substructures with a significantly larger volume fraction of high angle subgrains. Such substructures have been observed previously in work on machined Mg alloys.[10] Since these boundaries on average are expected to possess higher mobility than the low angle counterparts, it is perhaps not surprising to see a significantly reduction incubation period prior to the onset of recrystallization. This also suggests that the probability of finding a critical nuclei suitable to grow into a fully annealed grain size is necessarily higher, thereby leading to overall more rapid recrystallization kinetics. The rapid and comparatively more homogeneous recrystallization, in part, suggests continuous recrystallization as the operative mechanism. For reference, a summary of the incubation and recrystallization time differences is given in Table 6-1.

Table 6-1 – Incubation and annealing times for the three Fe-Si sample conditions. Note, the duration of incubation and recrystallization were significantly shorter for the machined samples compared to the rolled condition, suggesting a different recrystallization mechanism.

Specimen Condition	Incubation Time (sec)	Full Annealing Time (sec)
Rolled Fe-4wt%Si	600	2400
FM Fe-4wt%Si	120	900
LSEM	120	600

A few important notes are worth discussing in relation to the microstructural results. First, the deformation strain can also influence the recrystallization kinetics. Since the amount of strain imposed during the two different processing routes, especially the FM condition, was nominally the same as in the rolling, differences in the deformation were not likely the major factor differentiating the recovery and recrystallization behavior. Second, it should be noted that the starting hardness for the LSEM condition was significantly larger than the rolled and FM conditions. This difference can be attributed to the additional effects of constraining the deformation from selection of a low $\lambda = 1$. Interestingly the time to onset of recrystallization was essentially the same as for the FM condition. Large deformation strains also, in general, promote continuous type recrystallization.[69,70] Finally, the relative inhomogeneity of the recrystallization between the two machining samples was significantly different. In the case for FM, while recrystallization was rapid overall, distinct regions recrystallized while others remained unaffected at various times at temperature. LSEM, on the other hand, was very homogeneous and the recrystallization took place essentially isotopically in the specimen thickness. These discrepancies can be explained by differences in the two processing

methods. In FM, while a slow cutting velocity (V_o) was employed, it is clear that the deformation was not perfectly homogeneous. Adiabatic shear bands did not appear to form, however that does not forgo the presence of general inhomogeneous deformation. The application of a constraint in LSEM further confines the shear deformation, sharpening the deformation zone and greatly reducing inhomogeneous deformation tendencies. Therefore, it is perhaps expected to see a more homogeneous recrystallization behavior for LSEM.

6.3 Avrami Kinetics Analysis

While the microstructural analysis showed distinct discrepancies in the apparent recrystallization behavior for the deformation conditions, consideration of the kinetics is important to further emphasize these differences. For this study, the JMAK model was used to assess the isothermal recrystallization kinetics. As a way of quantitatively determining the recrystallization fraction, hardness data was utilized and the fraction recrystallized was estimated by:

$$X_v = \frac{H_d - H_i}{H_d - H_a} \tag{6-2}$$

where H_d, H_i and H_a represent the as-deformed, incremental and annealed hardness, respectively. In order to fully capture the recrystallization kinetics, all hardness measurements, except the initial and final, were used. Furthermore, analysis only considered the recrystallization regime. Hence, recovery was subtracted away. The results of the hardness evolution during annealing are presented in Figure 6-8, along with the recrystallization JMAK plot.

As noted on the micrographs, the decrease in hardness was significantly different for the rolled and machined samples. Those of machining exhibited an extremely rapid decrease in hardness simultaneously with a rapid appearance of recrystallization nuclei (Figure 6-8a). The overall shape was, in fact, quite sigmoidal. Furthermore, recrystallization was nearly complete in the machined samples before the onset in the rolling condition, which was characterized by a large period of recovery prior to the classical sigmoidal recrystallization curve.

Using the hardness evolution as a measure of the fraction recrystallized, which has been noted as an accurate approach, classical JMAK curves were developed.[78] In accordance with the literature, the slope of the JMAK curves represents the Avrami exponent, n. While the model as a whole has some shortcomings with respect to the underlying assumptions governing recrystallization, a comparison of these values is useful. For the two machining conditions, avrami exponent values were $n = 1.4$ (LSEM) and $n = 1.8$ (FM). Interestingly, the avrami exponent measured for the rolled condition was significantly larger, with $n = 3$. Theoretically, the avrami exponent is a function of both the nucleation rate and the growth morphology and can give insight into the recrystallization behavior.[79] Some idealized recrystallization processes can be approximated by the avrami number. For the case in which all the recrystallization nuclei exist at the initiation of recrystallization and growth is isotropic in three dimensions, n should be a value of 3. If the nuclei instead nucleate at some constant rate but still grow in three dimensions, n should be 4.[77]

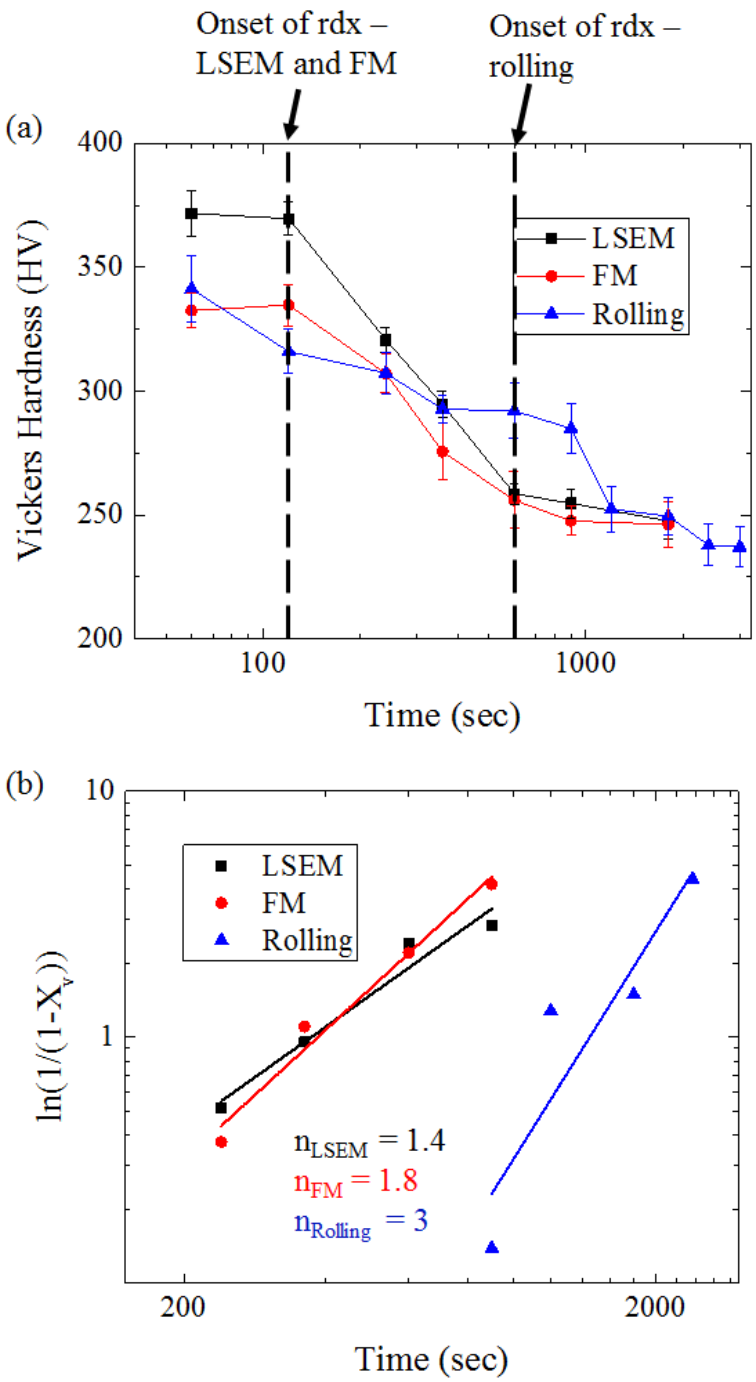

Figure 6-8 – Kinetics of recrystallization as determined from microhardness measurements: (top) hardness decay as a function of time at 600°C, (bottom) corresponding JMAK plot.

In most recrystallization studies, *n* values are less than both of these idealized cases, even approaching lower values of 1 in some studies. The reasons are complex and are still

debated. Factors such as the deformation microstructure, annealing microstructure and recovery have all been cited as contributing to a lower value.[76,80] Surprisingly, an *n* value of 3 was measured here for the rolled Fe-Si sheet, which is significantly larger than the two machining values. A tentative explanation is put forth to explain the differences.

Since the *n* was three for the rolled sample, theory suggests that the nuclei were all present right at the initiation of recrystallization. Despite this, discontinuous recrystallization was obviously observed during the annealing treatments. Consequentially, recovery in the rolling case is believed to have produced a substructure with low angle subgrains. Since recovery is a homogeneous process, upon its completion, a fairly homogeneous set of nuclei likely existed at the onset of recrystallization. This is particularly interesting given the inhomogeneous nature of the observed annealing nuclei. Therefore, the discontinuous nature of the recrystallization here is proposed to have been the result of differential growth rates among the various nuclei in the substructure. Particular nuclei possessing higher mobilities are expected to consume the deformation structure first while others grow at a slower rate. The origin of the differential growth rates is not known, however inhomogeneous deformation, local crystallographic texture and precipitates can all influence the nuclei growth rates.[77]

The machining conditions, on the other hand, exhibited significantly lower Avrami exponents. These lower values have generally been proposed to occur as result of higher density of defects acting as favorable nucleation sites within a deformation structure for annealed grains to develop.[77,81] Hence, larger deformation strains tend to promote smaller values of *n*. In the case for machined samples, deformation structures have been

shown previously to contain a larger volume fraction of UFG structures amidst a network of a high dislocation density structure.[10] Therefore, these UFGs could act as heterogeneous nucleation sites during recrystallization and grow at similar rates into the deformation structure, leading to more rapid kinetics and homogeneous recrystallization behavior. This is in general agree with literature in which more deformation leads to a larger percentage of high angle subgrain boundaries and defects, both of which lead to a transition to continuous type recrystallization.[69,70]

In summary, a series of recrystallization experiments were conducted on rolled and machined Fe-Si. Micrographs showed that the rolled condition possessed significantly more sluggish recrystallization kinetics compared to machined samples. Furthermore, the recrystallization of the rolled specimen occurred over a significantly longer time period and in a more discontinuous manner compared to the machined cases. Analysis of the hardness behavior and corresponding JMAK kinetics further emphasized the recrystallization differences, which are concluded as discontinuous for the rolled condition and continuous for the machined samples. As a whole, SPD-type processing like machining is expected to promote continuous recrystallization and consequentially preserve deformation textures.

CHAPTER 7. MAGNETIC PROPERTIES

This chapter summarizes preliminary magnetic properties of the shear-textured Fe-Si samples. First, an introduction to the common magnetic testing methods used by commercial vendors of Fe-Si sheet is discussed with typical properties for the two commercial non-grain-oriented (NGO) and grain-oriented (GO) sheets. The second part will discuss preliminary magnetic property measurements of the shear-textured sheets from three alloys: the commercial Fe-4wt%Si fine grain plate, Fe-3.5wt%Si and Fe-6.5wt%Si castings. Particular emphasis is on relative property differences as a function of the Fe-Si shear textures and composition. The final section will discuss some implications of the texture and preliminary properties.

7.1 Standard Magnetic Characterization Methods

Magnetic measurements must acquire accurate values of both the applied *H* and measured *B* fields for a give material. In doing so, several different magnetic testing methods have been developed in the literature.[82–84] Generally, magnetic characterization methods are classified as either open or closed loop techniques, depending on the characteristics of the particular applied magnetic flux. The physics of each, along with typical measurement devices, are briefly summarized.

7.1.1 Open Circuit Methods

A magnetic characterization method is said to be open if the applied magnetic flux, *H*, passes through both a strongly magnetic and non-magnetic material, the non-magnetic material typically being air.[9,83,84] An example of this type of field is shown for a bar specimen after being magnetized from left to right and removed from the field (Figure 7-1). In this case, the magnetic field passes through both the bar magnet and air, constituting an open circuit. For the bar magnet shown, free poles at the ends of the specimen generate *H* fields both inside and outside the bar, connecting the north and south poles. These fields act in direct opposition to the original applied *H* field and act to demagnetize the sample by a value $H_d = N \times M$. [84] Here, *M* is the measured magnetization of the specimen directly from the hysteresis loop and *N* is a tensor representing the demagnetization factor. Since these H_d fields act in a direction opposing the true *H* field and are usually unavoidable in open circuit measurement methods, the magnitude of the demagnetization must be dealt with rigorously to obtain accurate values of the true applied *H* field. Mathematically, this is accomplished by subtracting the H_d contribution from the apparent field by $H = H_a - H_d$, where H_a is the apparent (or measured) applied field directly from the hysteresis loop. This demagnetization correct is demonstrated for some data on grain-oriented Fe-Si in an open magnetic circuit (Figure 7-2). In general, the influence of the demagnetizing field is particularly important in soft magnets, where the magnitude can be a significant portion of the true field *H* or, even in some cases, much larger than *H*.

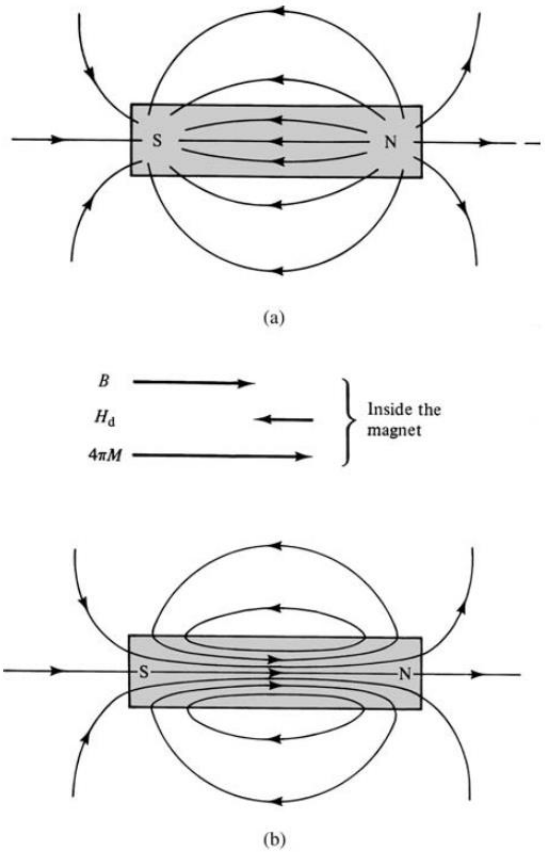

Figure 7-1 –Fields of an open bar magnetic (in zero field) after being subjected to an applied field from left to right: (a) H field, (b) B field. Poles develop on the free ends, which create fields that act against the applied field direction, demagnetizing the magnetic (after [9], with permission of Wiley).

Since only one particular geometry allows for a single demagnetization factor to be used, other geometries require additional demagnetization factors. To do so, two specific demagnetization factors are commonly used, depending on how the sample is magnetized.[85,86] If the magnetization occurs along a portion of the sample volume, typically near the sample midplane *via* a fluxmeter, a so-called fluxmetric demagnetization factor, N_f, is appropriate. This factor is defined as the ratio of the average demagnetizing

field to the average magnetizing field at the sample midplane. The second type, referred to as the magnetometric demagnetization factor, N_m, is the ratio of the average demagnetization field to the average magnetization field for the entire sample volume. Such a demagnetization correction must be applied if the entire sample is situated with a coil, for example in a vibrating sample magnetometer (VSM).

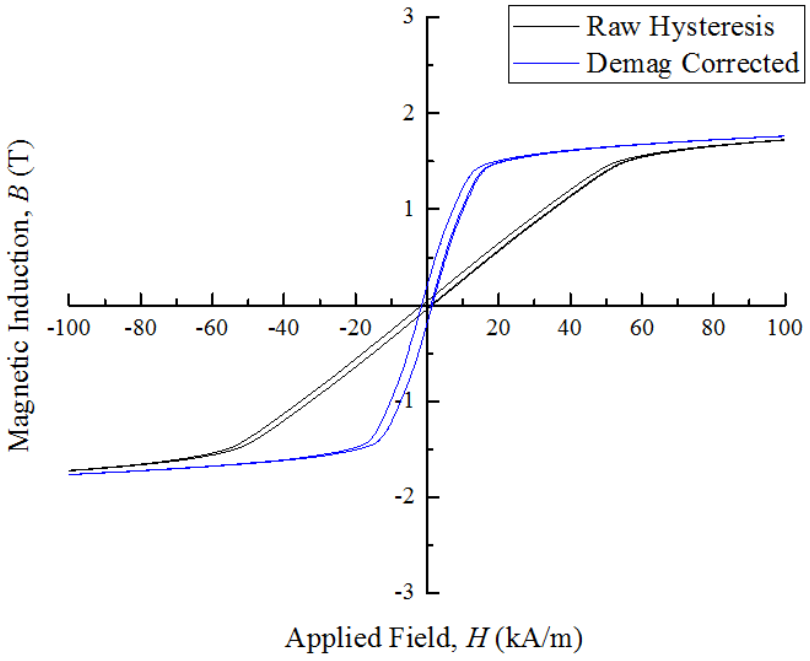

Figure 7-2 – Hysteresis loops for grain-oriented Fe-Si sheet specimen with and without demagnetization correction. Note, compensating for demagnetization shifts the hysteresis loop counterclockwise significantly, indicating the large influence of proper demagnetization.

Since the demagnetization factors are particularly important, open circuit measurement methods are ideal for sample geometries possessing large aspect ratios, such as thin-films and ribbons. Since sheet geometries processed here were of similar widths to these types of samples, initial magnetic properly measurements were attempted using an

open-circuit VSM apparatus. Rectangular samples from LSEM and the two commercial non-grain-oriented (NGO) and grain-oriented (GO) sheets from AK Steel were tested along the longitudinal direction. Unfortunately, after trial and error and despite proper demagnetization corrections using N_m factors –determined using a double linear interpolation method recommended by Chen et al. for simulated N_m values for general high permeability rectangular prism shaped samples – the resulting hysteresis loops gave poorly correlated magnetic properties. Specifically, for the commercial sheets, the magnetic permeability was orders of magnitude too low and coercivity was at minimum a factor of ~6 too large compared to the expected values published by AK Steel. For example, in the case of the GO sheet, the measured relative permeability was ~ 300, which is much lower than the value reported by AK Steel, ~50,000. A similar order of magnitude discrepancy was observed for the NGO sheet, where permeabilities were ~500 and compared to the expected values of ~11,000. These large errors are believed to be solely a result of inadequate demagnetization correction, suggesting the numerical correction methods available for the given specimen geometry and permeability are insufficient. Consequentially, the VSM approach was determined inadequate and a different closed-loop approach was taken.

7.1.2 Closed Circuit Methods

Unlike the open-circuit counterparts, closed-circuits do not have a significant amount of flux traveling through a non-magnetic substance. Instead, the flux is contained with the magnetic material of interest. Consequentially, demagnetization fields are essentially

negligible compared to the open methods and are especially useful for soft magnetic materials. Three common closed-circuit methods are described here.

7.1.2.1 Epstein Frame

In closed magnetic circuits, one of the most common configurations to measure magnetic properties is through a disk or ring-shaped sample, which includes stacked rings, coiled ribbon, sintered ring and a stack of discrete sheets with overlapping corners. This latter method, referred to as the so-called Epstein test (or frame), provides a way of measuring the directional magnetic properties of sheet laminates stacked in a rectangular geometry. Due to this ability, it is the main measurement method used by the electrical steel sheet manufacturers, like AK Steel, to characterize the anisotropic magnetic properties of Fe-Si sheets. The Epstein frame is an ASTM standardized method, cited in ASTM A343/A343M-14 and ASTM A596/A596M-14, for measuring AC and DC directional magnetic properties.[87,88]

The Epstein frame consists of several laminates stacked in alternating order in a square configuration (Figure 7-3). Care is used to ensure sheets are flat and only make contact (lap) at the corners of the frame. Individual sheets are standardized to 3 cm in width and no less than 28 cm long. The number of sheet specimens used in the frame depends on the desired mass, which ASTM standardizes at 500, 1,000 and 2,000 grams. Four sets of coils are used for magnetizing the sheets and measuring the properties, with two sets of windings within each coil. The interior winding is used for measuring the properties while the external winding is used to magnetize the sheets. To determine the applied H field, the magnetization current I is measured along the length of the magnetization path of the sheets.

For determining the induction *B*, polarization *J* is measured and converted using the specimen geometry.[89] For this method, it is critical to minimize the air-gap between the two windings and the specimens, which can artificially 'shear' the hysteresis loops in the same manner, but a much lesser extent, as the demagnetization effects for open-circuit methods.

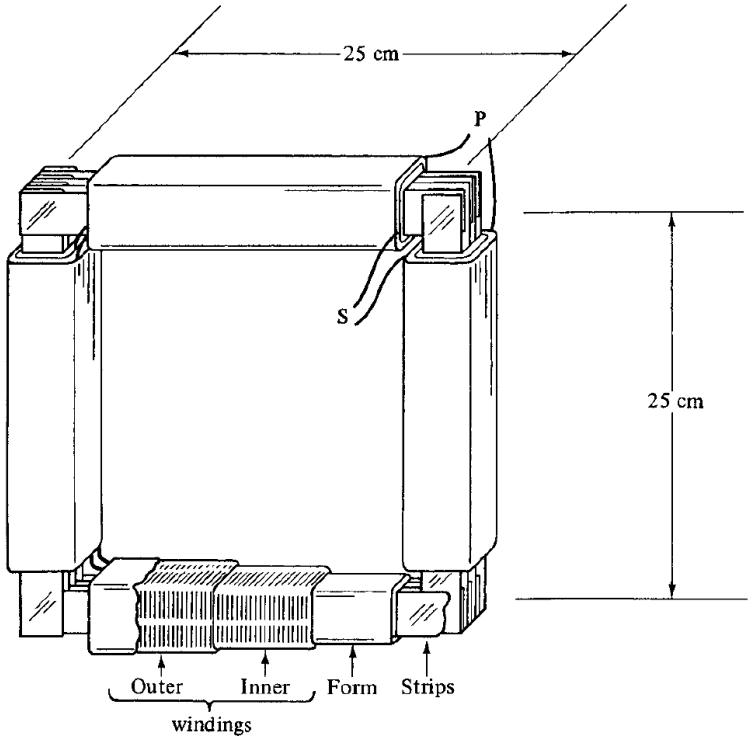

Figure 7-3 – Schematic of the Epstein frame, showing a series of narrow strips stacked in alternating order in a square configuration. Note, the sheets only make contact at the lapped corners (after [9], with permissions of Wiley).

For AK Steel, the major domestic producer of electrical steel sheet, DC hysteresis loops are obtained using the Epstein configuration, where permeability, coercivity and saturation induction are reported for various grades of Fe-Si. Typical relative maximum

permeability values for the grain-oriented (GO) sheets (magnetized along the rolling direction, RD) are significantly large, ~50,000, while the non-grain-oriented (NGO) sheets range from 6,000-16,000.[90,91] Coercivity values have also been reported for fully processed NGO sheets (at B = 1 T), with values ranging from 20-80 A/m depending on the silicon content.[91] Note, coercivity drops dramatically with increasing silicon content. Saturation induction values tend to vary from 1.9-2.1 T, also decreasing with increasing silicon content.

Perhaps the most advertised magnetic property is the core loss, a parameter which is composed primarily of hysteresis and eddy current losses. For some motor laminates (NGO), the losses are measured up to 10,000 Hz while transformer cores (GO sheets), are quantified in the 50 and 60 Hz range.[90] These values are usually normalized to the sheet mass and reported as W/kg as a function of frequency and flux density. For the NGO sheets, maximum core loss values at 60 Hz vary from 1.5-3.2 W/kg, where the lower values are measured from higher silicon alloys (~ 4wt%) and thinner sheet thicknesses (~ 0.36 mm).[91] Typical values for the GO sheets (along the RD) are 1.3-2.6 W/kg, depending on the particular grade.[26,90]

7.1.2.2 Single Sheet Tester

In addition to the Epstein configuration, these same properties, particularly the core loss, can be obtained using a single-sheet characterization method. This so-called single sheet tester is also standardized with ASTM, as outlined in ASTM A804/A804M-04 and ASTM A596/A596M-14.[88,92] Unlike the Epstein test, which requires a stacking of individual electrical steel laminations, this method allows for characterization of single

laminations to obtain directional properties. Two different types are cited in the ASTM standards, defined as either single or double-yoke configurations. An assembly view of the double yoke is shown in Figure 7-4. The yoke serves to close the magnetic circuit with the magnetic material of interest. Yokes themselves are made of extremely soft magnetic materials or are laminates of soft ferromagnets, which are then coated if AC measurements are performed to minimize eddy current contributions. Single or multiple sheets are inserted and clamped between both a top and bottom yoke, composing the yoke frame. For a single yoke, the sheets are in contact with that particular yoke. Coils used for both magnetization and measurements are then wrapped around the single sheet, where, like the Epstein, the inner windings are used for measurement and the outer magnetize the sample. The sheet specimen geometry is variable. Lengths must be at least as long as the yoke lengths and, for best accuracy, widths should be at least 50% the width that can be accommodated by the test coil. Specimens are usually sheared and must be as square shaped as possible.

Compared to the Epstein frame, the single sheet tester method is particularly useful for quantifying the magnetic properties of single sheets, thereby allowing for characterization of the anisotropy of individual laminates. It's primary use, for AK Steel, is in characterization of the core loss for the GO sheets, where the high degree of anisotropy is best captured using single sheet tests.[90] In that case, care is taken to ensure that the individual laminates are aligned within 1° of the RD.

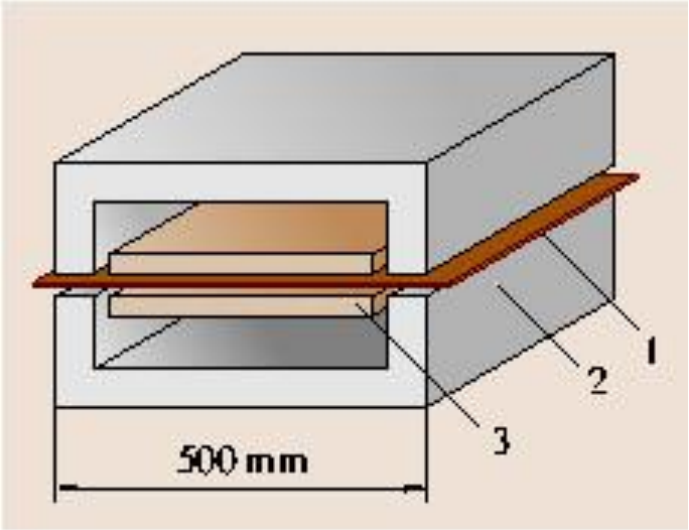

Figure 7-4 – Double yoke single sheet testing method for acquiring directional magnetic properties of individual sheet laminations: (1) test specimen, (2) assembly yokes and (3) magnetizing and measuring coils (from [89], with permission of Springer).

7.1.2.3 Permeameters

Yet another closed-circuit analysis method are the so-called permeameters, or hysteresisgraphs, which are used for both AC and DC (or quasi-static) hysteresis loop analysis. Due to the versatility of this approach, a permeameter was used to characterize the Fe-Si specimens in this study. Measurements were carried out using quasi-static hysteresis loop analysis, courtesy of Magnet-Physics Inc. (Fishers, IN). Two main configurations of permeameters are most commonly used, depending on the shape of the magnetic material. If samples are in ring form, or similar closed-circuit geometry, a separate permeameter configuration is used and based on the shape of the sample. Samples in the form of bars or sheet require the use of yokes, similar to those described for the single

sheet tester. For such geometries, three different yoke configurations are most popular. In the present study, the configuration used is shown Figure 7-5.

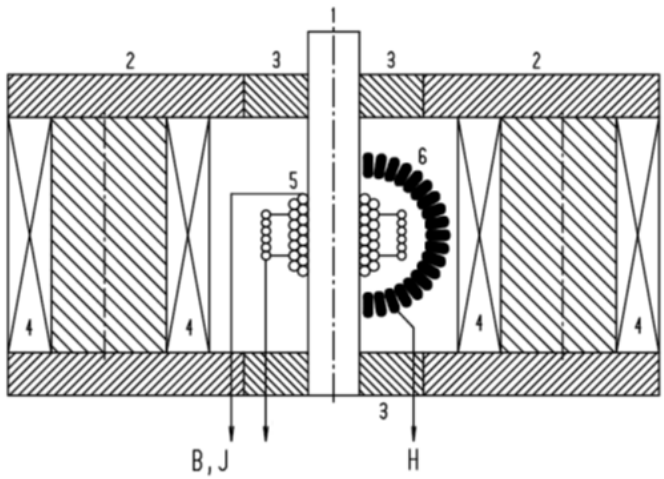

Figure 7-5 – Schematic of the measuring yoke used by Magnet-Physics Inc. to characterize the Fe-Si sheet samples: (1) specimen, (2) soft magnetic steel, (3) pole pieces, (4) field generating coils, (5) J-compensated surrounding coil, (6) potential coil (after [93]).

The permeameter configuration used here, a so-called type B permeameter, is useful for measuring sheet and strip sample geometries. In this method, the sample is clamped between the poles of a double-C yoke and the polarization *J* is measured using *J*-compensated surrounding coils, which are wrapped as closely as possible around the sample surfaces to minimize the air-gap contribution. A schematic showing the *J*-compensated coil used here is shown in Figure 7-6.

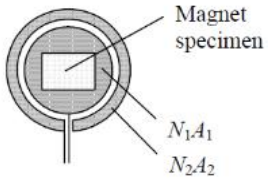

Figure 7-6 – Example *J*-compensated coil used to magnetize and measure the Fe-Si sheets (after [93]).

The basic principle of using a *J*-compensated coil is through the use of two separate coils, defined by different area turns of N_1A_1 and N_2A_2, respectively. Coil one accepts the magnetic sample and determines the magnetic flux by:

$$\phi_s = B_s N_1 A_S \tag{7-1}$$

where B_s is the flux density of the sample, N_1 is the number of turns for the interior coil and A_s is the sample cross-sectional area. Often times, the sample is not perfectly surrounded by the interior coil and an unavoidable air-gap results. Compensating for this air-gap is accomplished by calculating the air flux by:

$$\phi_1 = (\mu_o H) N_1 (A_1 - A_S) \tag{7-2}$$

where μ_o is the free-space permeability, H is the field strength in air adjacent to the sample, N_1 is the number of turns of the interior coil, A_1 is the area of the interior coil and A_s is the sample cross-sectional area. An external coil is then applied, which also surrounds the sample without enclosing it and is therefore used to estimate only the flux contribution from air by:

$$\phi_2 = (\mu_o H) N_2 A_2 \tag{7-3}$$

The effective (total) magnetic flux is then determined by:

$$\phi = \phi_s + \phi_1 - \phi_2 = (J) N_1 A_s \tag{7-4}$$

From the above expression, determination of *J* only requires the number of turns of the interior coil, N_1 and the cross-sectional area of the sample, A_s. The measuring and magnetizing coils are then connected to fluxmeters and used with a data acquisition system to obtain full hysteresis loops. As a whole, *J*-compensated coils then provide an accurate *J*-*H* curve, which can be converted to a *B*-*H* curve by:

$$B(H) = \mu_o H + J \tag{7-5}$$

For a permeameter type B, the applied field strength *H* is measured using a c-shaped potential coil that is attached directly to the sample surface (Figure 7-5). The potential coil is used to measure the magnetic potential (*P*) between two points along the sample surface, separated by distance *S*, and *H* is then determined by simply taking the ratio of *P*/*S*. In order to ensure a homogeneous magnetic flux distribution over the entire specimen cross-section, samples must be a minimum of 90 mm in length.

Procedurally, samples tested in the hysteresisgraph were demagnetized prior to measurement. This was done by applying an AC magnetic field with gradually decreasing amplitude. Once the sample was fully demagnetized, a “virgin” magnetization curve was obtained for determining accurate permeability values, followed immediately by a full hysteresis loop, constituting a five-quadrant sequence hysteresis loop analysis. Speed of the measurement was computer controlled to maintain a constant change in *B* with time *t*.

For these type of measurements, it is critically important to maintain a slow scan speed so as to minimize eddy current contributions, yet fast enough to maintain stability in the fluxmeters.[93]

In summary, open and closed circuit magnetic measurements were detailed. Preliminary studies using an open circuit VSM were carried out on the Fe-Si sheet, with little success at producing reliable properties of commercial standards matching the Epstein frame. Consequentially, closed magnetic circuit methods were explored and a type B permeameter was detailed as the final candidate for obtaining magnetic properties from the Fe-Si specimens. Results are now disclosed and a discussion is provided relating the properties with respect to texture and composition.

7.2 Results

This section discusses the preliminary magnetic properties for a variety of Fe-Si alloy conditions. Hysteresis loops are first given for two commercial GO (TRAN-COR®H) and NGO (DI-MAX® HF-10X) sheets, courtesy of AK Steel, followed by a series of shear-textured Fe-Si specimens of varying silicon content. For the experimental (machined) Fe-Si conditions, annealed grain sizes were held nearly constant, $d \sim 20\ \mu$m, allowing for a discussion of the properties with respect to crystallographic texture and composition. Comparisons between the experimental samples and commercial samples are also given and related to both microstructural and compositional differences.

7.2.1 Commercial NGO and GO Sheets

For calibration purposes, samples from the NGO and GO sheets provided by AK Steel were characterized initially. The resulting hysteresis loops are shown in Figure 7-7. It is important to note that the H field limits during testing were ±65 kA/m (Section 4.5), which is unlike the traditional Epstein frame. As a consequence, magnetic properties including the coercivity, H_c, maximum induction, B_{max}, and hysteresis loss, W, are considered accurate for loops ending at these H field values. However, maximum relative permeability μ_{max}, which occurs at relatively small H values, are generally unaffected by the upper H field limitations.

The loops for the NGO and GO samples are plotted as magnetic induction, B in Telsa (T), against applied field, H in kA/m. Hysteresis loops for the two commercial sheets were very similar in overall appearance, characterized as magnetically soft, as expected of ferromagnetic materials like Fe-Si. Closer inspection revealed subtle yet important differences in the two loops, thereby providing the basis for comparison with expected values from the Epstein frame. The first major distinction of the two loops was the respective hysteresis widths. As shown in the lower right inset, the NGO sheet possessed a significantly larger hysteresis width than the GO sheet, with a coercivity H_c = 29 A/m (NGO) compared to H_c = 6 A/m (GO). Interestingly, despite the larger H_c values for the NGO sheet, the hysteresis loss W (integrated loop area) was 97 J/m^2 for the NGO and 139 J/m^{2}for the GO conditions, respectively.

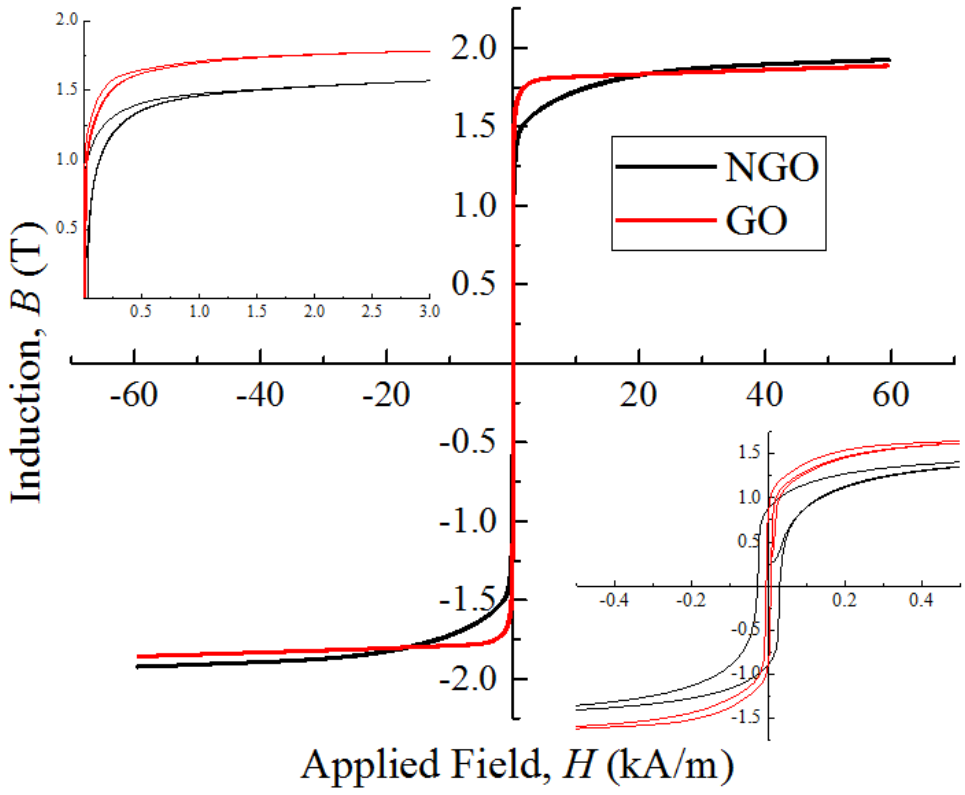

Figure 7-7 – Hysteresis loops for the NGO and GO sheet samples from AK Steel: (left) portion of the right quadrant, (middle) fully hysteresis loops, (right) 500 A/m zoomed hysteresis loop. Note, the loops shown here include the virgin magnetization curve, from which maximum relative permeability is calculated.

Analysis of the hysteresis loops near the "knee", shown in the upper left inset, indicated that the NGO sheet required significantly larger *H* values to achieve nominally similar *B* values, suggesting a lower overall permeability. This is in agreement with the calculated (relative) μ_{max} values of the two samples, which was 10,900 for NGO and 33,400 for GO, respectively. At large *H* fields, both began to approach high *B* values with a decreasing slope. Typically, at these large *H* fields, the (polarization) *J* values tend to reach a maximum for soft ferromagnets and the corresponding *B* value determines the saturation

induction, B_s. However, true saturation induction values were not achievable for most samples here–except the GO condition due to the applied H field limits. Instead, maximum induction values (B_{max}) are quantified at the largest H field, H_{max} = 65 kA/m. For the NGO sheet, B_{max} = 1.92 T, compared to B_{max} = 1.88 T for the GO condition. In the case for the GO sheet, $B_{max} = B_s$, i.e., the J values reached a maximum with J_{max} = 1.81 T. While the measured J values for the NGO specimen never truly saturated, only a very slight residual slope remained at the largest H field, indicating true saturation was very near.

In the strictest sense, a direct comparison between data gathered from the permeameter and the Epstein frame for the same sheet products from AK Steel is difficult because most reported values are at particular values of H and/or B. Furthermore, some of the properties, including H_c and W are not available for the tested sheets from AK Steel. As such, the most useful comparison is in the permeability analysis, which can be estimated from the measured quasi-static virgin magnetization curves, which are published by AK Steel. Analysis of these curves revealed that common μ_{max} values for NGO and GO sheets from the Epstein analysis are ~11,000 and ~65,000, respectively. Values measured by the permeameter, 10,900 for NGO and 33,400 for GO, were significantly close to the expectations, especially the NGO sheets, where the values were essentially the same. This comparison indicates that the permeameter approach is a validated closed circuit method and effectively calibrated to the industrial standards. Note, the larger discrepancy between the permeameter and Epstein tested GO datasets is likely due to alignment differences. Permeability is known to decrease drastically when the applied flux is off the rolling direction axes by even 1° for the GO condition. Consequentially, exactly matching of the Epstein values is perhaps not expected and instead an order of magnitude comparison is

sufficient. Due to the much weaker texture and lower anisotropy, the NGO samples are not particularly dependent on the magnetization direction, leading to nearly identical values between the two characterization methods. As a result, the magnitude of the permeability values are expected to be accurate for the experimental Fe-Si conditions presented here.

7.2.2 Fe-4wt%Si

Discussed first are the tests from the shear-textured Fe-4wt%Si plate. A series of specimens were prepared from the commercial Fe-4wt%Si alloy plate, courtesy of Scientific Alloys Inc. Magnetic properties were assessed for five total conditions, four of which were machined and one rolled. The rolled condition served as the baseline for the given alloy composition and purity The resultant hysteresis loops are summarized in Figure 7-8. As with the NGO and GO sheets, the full-field view of the hysteresis loops appeared to resemble soft magnetic behavior with generally narrow hysteresis loop widths. Furthermore, high B values were achieved at relatively small H fields, indicative of fairly high permeability. From the full field view, it is clear that the rolled sample exhibited the highest maximum induction, with B_{max} = 1.75 T, while the shear-textured samples exhibited values of B_{max} = 1.5 – 1.61 T, depending on the condition.

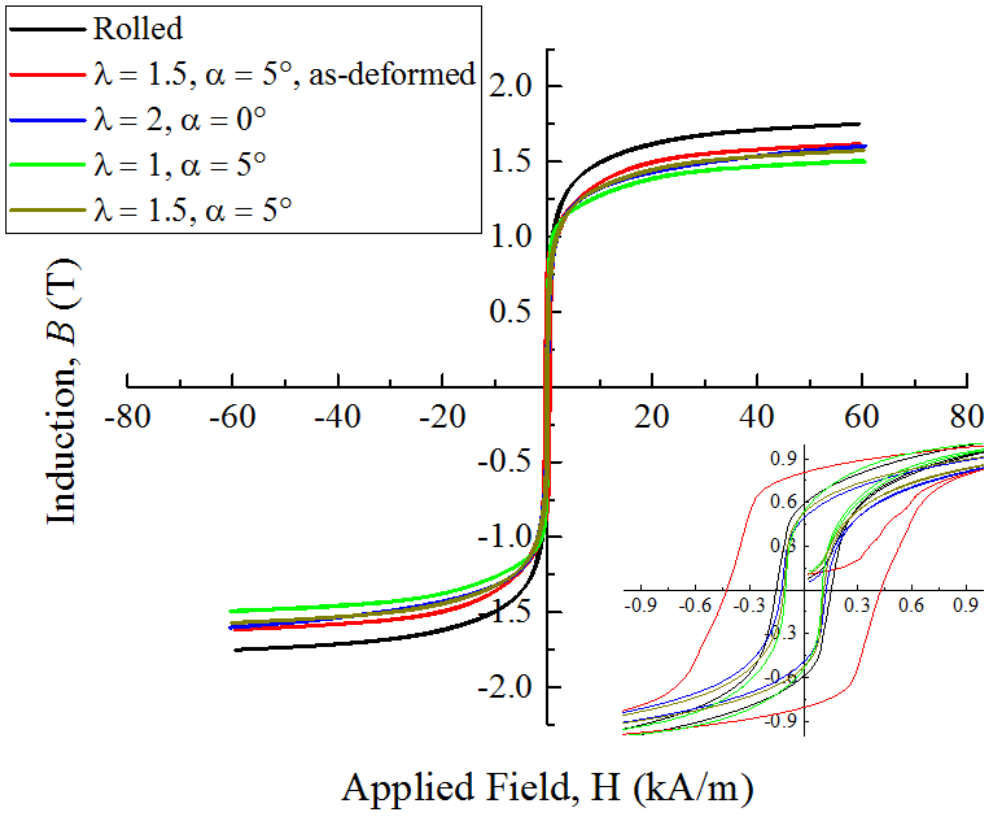

Figure 7-8 – Hysteresis loops for the five Fe-4wt%Si conditions analyzed in this study. The lower right inset shows a zoomed-in view of the loops, identifying the relative loop widths. Similar to the loops for the NGO and GO sheets, the initial magnetization curves are also shown.

At smaller *H* field values, important differences in the 4wt%Si hysteresis loops were observed. The differences can be identified on the inset of Figure 7-8 and from tabulated data of Table 7-1. The first, perhaps most notable difference identified is the hysteresis loop width for the as-deformed Fe-Si condition (red loop), which had a large coercivity H_c = 426 A/m. This is compared to the lower values for the annealed conditions, which presented variable coercivity values with H_c = 102-153 A/m (Table 7-1). The wider hysteresis loop produced a correspondingly larger loss W = 1950 J/m^2, compared to the

relatively lower range from the annealed conditions with W = 400-1,000 J/m^2. Additionally, the virgin magnetization of this particular condition had a much shallower slope, leading to a μ_{max} = 829, compared to μ_{max} = 1440-1783. Consequentially, the as-deformed condition systematically possessed the worst soft magnetic properties of the Fe-4wt%Si alloy series. The reasons for the poor performance can be related back to the microstructural differences. In the as-deformed condition, a microstructure containing ultrafine grains with a high dislocation density is expected. Since dislocations and grain boundaries are known to reduce impede the motion of magnetic domains, magnetic performance declines. It is perhaps not surprising then to see this condition exhibit the lowest permeability and highest coercivity and hysteresis loss.

For the annealed specimens, properties were relatively similar in absolute magnitude. The λ = 2 processing condition was characterized by the lowest permeability (μ_{max} = 1441) with highest coercivity (H_c = 124 A/m) and hysteresis loss (W = 1000 J/m^2), followed by the rolled (μ_{max} = 1560, H_c = 153 A/m, W = 410 J/m^2), λ = 1.5 (μ_{max} = 1698, H_c = 111 A/m, W = 401 J/m^2) and λ = 1 (μ_{max} = 1783, H_c = 102 A/m, W = 438 J/m^2) conditions, respectively. Overall, differences were minor compared to the sharp discrepancies between the commercial NGO and GO sheets. Therefore, despite a significantly large range of λ values, the properties suggest that the shear processing did not develop textures that contain a particularly high degree of anisotropy compared to conventional NGO rolling textures. However, the differences that do exist are worth discussing in relation to the crystallographic textures between the various processing conditions.

Table 7-1 – Summary of magnetic properties for the Fe-4wt%Si sheets obtained from analysis of hysteresis loops measured by a permeameter.

Specimen	Maximum Permeability, μ_{max}	H_c (A/m)	Hysteresis Loss, W (J/m^2)	Max Induction, B_{max} (T)
$\lambda = 1.5$ $\alpha = 5°$*	829	426	1950	1.62
Rolled	1560	153	410	1.75
$\lambda = 1.5$ $\alpha = 5°$	1698	111	401	1.58
$\lambda = 2$ $\alpha = 0°$	1441	124	1000	1.61
$\lambda = 1$ $\alpha = 5°$	1783	102	438	1.51

* - as-deformed condition

Since the grain size and composition for the annealed conditions were all essentially identical, the subtle differences in reported property values are believed to be a result of differences in the crystallographic texture. As discussed in Section 5.3.8, a basic unit cell model was introduced for calculating the orientation of <001> easy magnetization directions with respect to the applied magnetic flux along the sheet length. It was suggested that this could give first-order insight into shear texture angle effects on magnetic properties. This model is used here to aid in the explanation of the property trends, specifically focused on permeability and coercivity. To demonstrate this, the plot of the <001> orientation from the applied field along the sheet length as a function of the shear plane angle is reformatted to focus on the *active* <001> directions. In determining the active easy magnetization directions, it was assumed that the <001> directions closest to the applied H field was the operative or active direction involved in the magnetization processes. The active <001> directions are shown in the reformatted model as solid lines (Figure 7-9). For reference, the other (inactive) <001> direction orientations are shown as dotted lines.

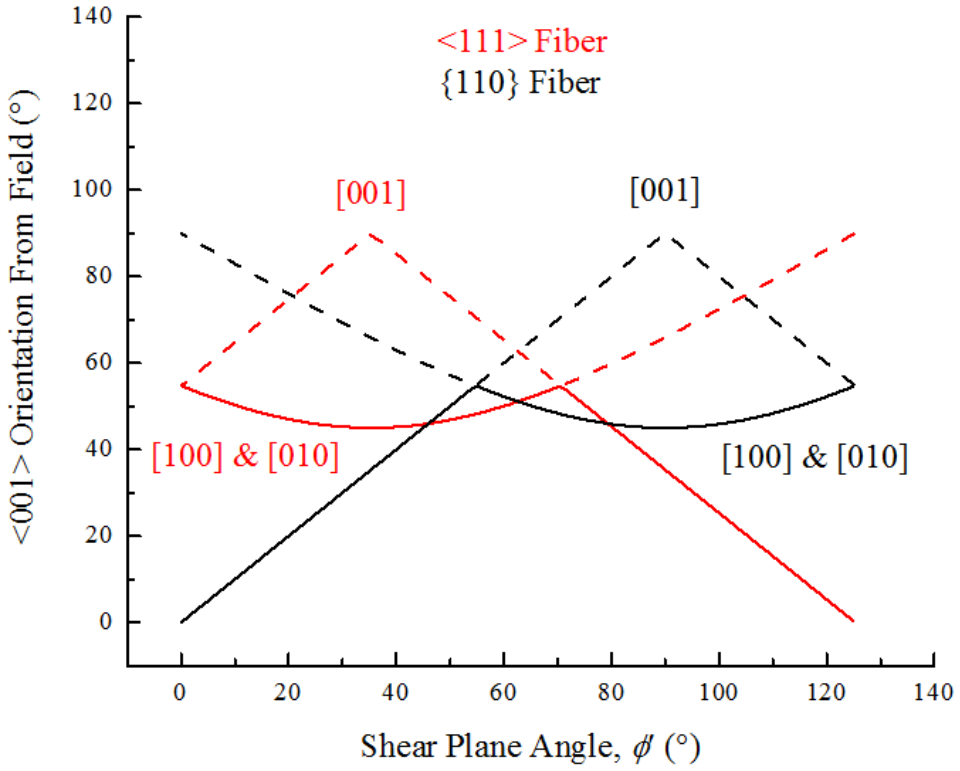

Figure 7-9 – Orientation of the <001> directions from the field as a function of the shear plane angle. In this case, the orientation for the active <001> directions of the two shear fibers are solid lines. The remaining orientation angles of the inactive <001> directions are shown as dotted lines.

With this updated analysis, the structure sensitive properties, i.e., permeability and coercivity, can be plotted as a function of the shear plane angle and compared with the active <001> direction orientations for both <111> and {110} fibers. Both plots are shown in Figure 7-10.

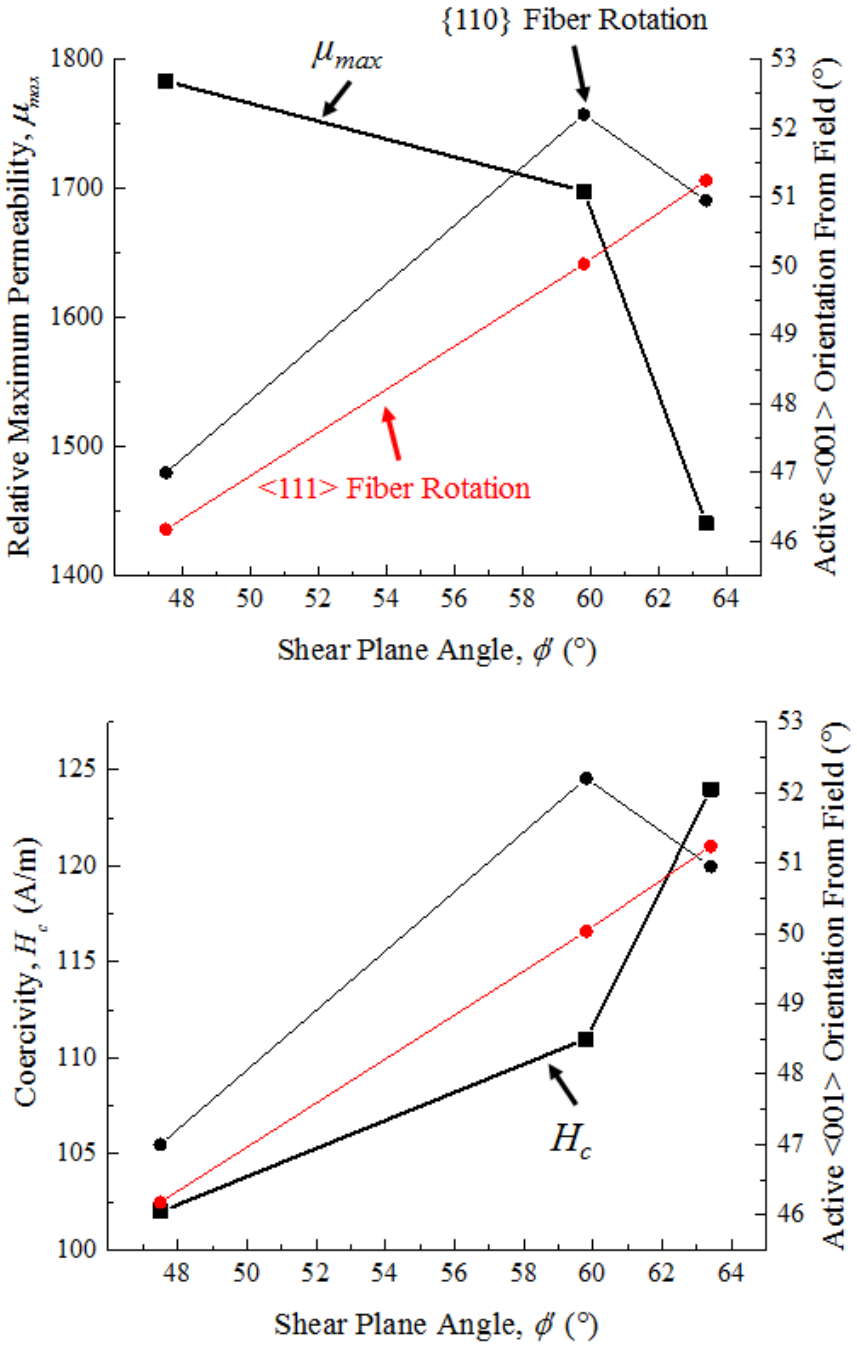

Figure 7-10 – Effect of shear plane angle on select magnetic properties: (top) maximum relative permeability μ_{max}, (bottom) coercivity, H_c. Provided with the properties is the active <001> orientation from the applied field, determined from the unit cell model. Properties are shown to improve with decreasing shear plane angle by virtue of a closer active <001> direction orientation to the applied field for the <111> fiber.

Important insights can be gained from analysis of the plots in Figure 7-10. A general trend is revealed, suggesting that select structure-sensitive magnetic properties for the Fe-4wt%Si alloy generally improved with decreasing shear plane angle ϕ', for a given grain size. This is noted by a steadily increasing maximum relative permeability, μ_{max}, and a decreasing coercivity, H_c, with a decreasing shear plane angle. These trends in permeability and coercivity can perhaps be explained from the unit cell model when compared to the active <001> orientations from the field for the two {110} and <111> (Figure 7-10). For a majority of the two fibers over this experimental processing range of nearly 20° (shear plane angle range), the orientation of the active <001> directions with respect to the field for the <111> fiber tend to increase with increasing shear plane angle. The <001> orientation angles from the field for the {110} fiber show a similar increase with increasing shear plane angle until $\phi' = 60°$, after which the orientation from the field begins to decrease. As a whole, it is expected that a texture orientation with lower <001> orientations from the applied field would improve the magnetic properties by virtue of a lower required *H* field to achieve high induction *B* values.

Textures presented in this study were shown to contain both {110} and <111> fibers inclined relative to the sheet surface. However, a significantly larger portion of the diffraction data was found to be situated along the <111> fibers compared to the {110} fibers, suggesting a larger volume fraction of grains followed along the <111> partial fiber. Consequentially, it is expected that the magnetic properties for the shear textured specimens are more heavily influenced by the orientation of the <111> fiber. Permeability and coercivity measurements here support this hypothesis, where the trends in

measurements match the expectations of the <001> orientations from the field for the <111> fiber.

The implications of this analysis are potentially significant. While properties were generally not considerably different in terms of overall magnitude, as compared to the NGO and GO examples, subtle differences in two important structure-sensitive properties were indeed measured as a function of the sheet texture. Due to the wide range of texture control *via* selection of the deformation path, simple deformation by LSEM should then be expected to develop a range of sheets with varying magnetic properties which can, to a small extent, be controlled. Furthermore, the observed trends of the measured properties as a function of texture followed expectations of a unit cell model. This is important because it suggests that, in addition to controlling the magnetic properties through the deformation path, a first-order prediction of the properties might be possible from a simple unit cell model for the inclined simple shear textures. Sheet might then be developed in the future with particular processing conditions to engineer textures for particular performance.

7.2.2.1 Comparisons with Commercial Sheets

When compared to the commercial sheets, magnetic properties measured for the Fe-4wt%Si alloy, including the rolled and annealed condition, were noticeable worse in terms of a lower maximum permeability – which in turn prevented true induction saturation – in addition to a higher coercivity and hysteresis loss. These differences are worth discussing with respect to the intrinsic metallurgical dissimilarities.

The first main difference between the commercial sheets and the experimental conditions of the 4wt%Si alloy is the as-tested grain size. For the two commercial AK Steel sheets, grains were significantly large, with d~ 150 μm (NGO) and d ~ 4-5 mm (GO). This is compared to fine annealed grain sizes of the experimental conditions, d ~ 20 μm. Since the finer grains of the experimental conditions constitute a larger total grain boundary area and grain boundaries are known to impede the microscale magnetization processes, the structures of the experimental conditions might be expected to contribute to the lower magnetic performance in the structure-sensitive properties.

Furthermore, structures of the commercial sheets possess fundamentally different crystallographic textures, with the nearly random rolling textures of the NGO sheet and the sharp Goss grains of the GO condition. In the case for the NGO sheet, textures are expected to be similar to the rolled Fe-4wt%Si condition here. Since the magnetic properties of the rolled condition were nominally the same as the shear-textured counterparts, it is suggested that the simple shear textures alone were not a significant factor in deteriorating the properties, at least compared to the NGO sheet. The GO condition, on the other hand, has the best magnetization situation when the applied H field is parallel to the sheet length (rolling direction), due to the alignment of one of the <001> directions. Theoretically, only special simple shear textures can even be attempted to achieve similar <001> orientations in a Goss-type fiber. This was not explored in a bulk sheet for properties analysis here. Therefore, compared to the GO condition, both the grain size and texture of the LSEM conditions likely contributed to the differences in properties.

An additional consideration is differences in the alloy purities. For the two commercial NGO and GO sheets, alloy compositions had only trace amounts of interstitial elements from sophisticated decarburization annealing treatments, leading to alloys with <0.003wt%C and S. This is unlike the 4wt%Si alloy used here, which had ~0.03wt%C and 0.015wt%S, respectively. Since these interstitial impurities are known to influence magnetic performance, it was likely a contributing factor. To explore this effect, custom Fe-Si castings were developed and sheet were produced.

7.2.3 Cast Fe-3.5wt%Si and Fe-6.5wt%Si

In an effort to develop Fe-Si alloy sheets with higher purity, two separate castings were developed at Fe-3.5wt%Si and Fe-6.5wt%Si. The former is a composition closer to the commercial Fe-Si sheet compositions for the NGO and GO sheets, while the latter is the ideal composition. Hysteresis loops for the complete set of conditions from each alloy are shown in Figure 7-11. As charge materials for the castings, interstitial free (IF) steel (courtesy of ArcerlorMittal) and semiconductor silicon were used. The chief desire of using the IF Steel was for the reduced carbon content (0.002wt%), which was about one order of magnitude higher in the 4wt%Si starting workpiece material.

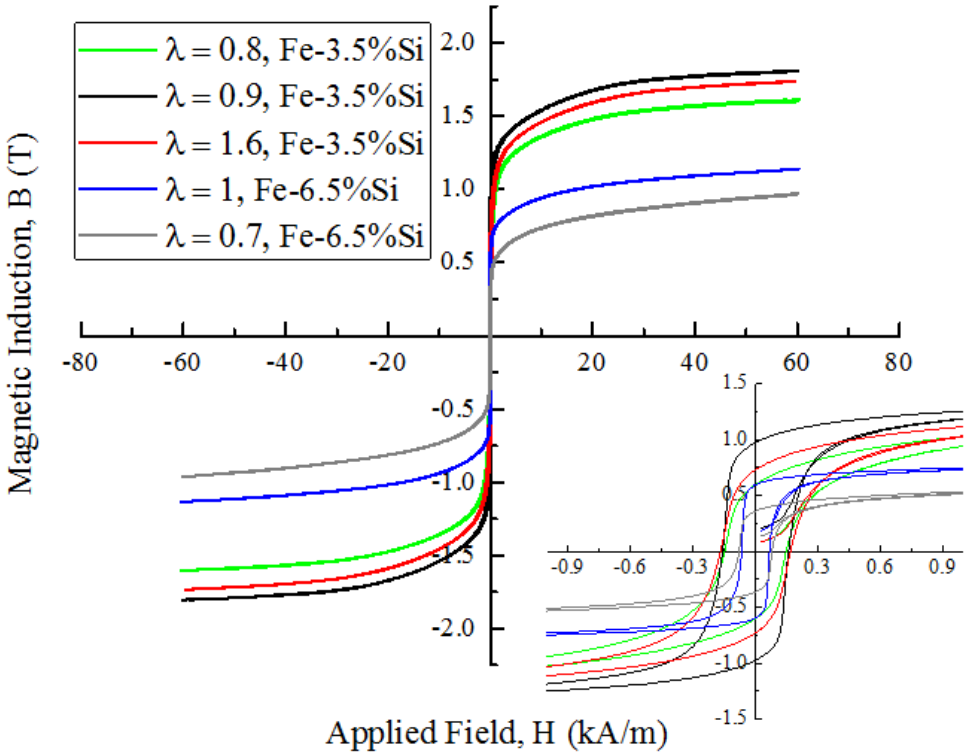

Figure 7-11 – Hysteresis loops for specimens produced from cast Fe-3.5wt%Si and Fe-6.5wt%Si. Note the significantly reduced B_{max} for the higher silicon content alloy. Inset in lower right shows the hysteresis loop widths, where the 6.5wt%Si alloy possessed a considerably lower H_c.

Full field view of the hysteresis loops again shows soft magnetic behavior for the two alloy sheets. The qualitative appearance of the loops for the 3.5wt%Si alloy composition were similar to the 4wt%Si commercial plate, with μ_{max} = 1468 – 2292, H_c = 148 – 168 A/m, W = 978 – 1590 J/m^2, B_{max} = 1.61 – 1.81 T. At the higher silicon content, the two 6.5wt%Si alloy sheets possessed significantly different properties, with μ_{max} = 2292 and 2655, H_c = 79 and 67 A/m, W = 651 and 310 J/m^2 and B_{max} = 0.97 and 1.14 T, respectively. Tabulated values are given in Table 7-2.

Table 7-2 – Summary of magnetic properties for the Fe-3.5wt%Si and Fe-6.5wt%Si sheets obtained from analysis of hysteresis loops measured by a permeameter

Specimen	Maximum Permeability, μ_{max}	H_c (A/m)	Hysteresis Loss, W (J/m^2)	Max Induction, B_{max} (T)
λ = 0.8, 3.5%Si	1468	148	1590	1.61
λ = 0.9, 3.5%Si	2292	159	1510	1.81
λ = 1.6, 3.5%Si	1583	168	978	1.74
λ = 1, 6.5%Si	2655	67	310	1.14
λ = 0.7, 6.5%Si	2292	79	651	0.97

Despite the comparatively lower carbon levels of the charge materials used to create the Fe-Si castings, the magnitude of the magnetic properties was not significantly different than the Fe-4wt%Si alloy. However, as with the 4wt%Si alloy results, relative differences are important to discuss. When comparing the two cast alloy compositions, the Fe-6.5wt%Si alloy exhibited significantly lower H_c, W, and B_{max} values than the 3.5wt%Si sheets. Furthermore, μ_{max} values for the 6.5wt%Si alloy were larger than nearly all experimental Fe-Si conditions studied (equal permeability with only one Fe-3.5wt%Si condition, see Table 7-2). As disclosed throughout Chapter 2, the addition of silicon generally improves the intrinsic magnetic properties of iron up to the ideal 6.5wt%Si. Commonly reported effects include increased permeability, decreased coercivity and core loss and decreased saturation induction. All these property changes, except the core loss (not tested), were observed for the 6.5wt%Si alloy compared to the 3.5 and 4wt%Si compositions. With nearly constant grain size throughout this study, the effects observed in the 6.5wt%Si alloy are likely related to the increased silicon content only and not related to texture. It is worth noting however that in-depth crystallographic texture analysis of the

cast Fe-Si sheets have not yet been performed. In Section 5.3.6, shear textures were shown to develop in cast Fe-6.5wt%Si when deformed at high temperatures. It is therefore expected that similar textures were developed in the cold-worked and annealed 3.5wt%Si and 6.5wt%Si sheets from cast precursors. However, texture effects on magnetic properties cannot be commented on, as in the 4wt%Si experiments, since even a qualitative understanding of the relative volume fractions of the two {110} and <111> fibers are currently unknown. Furthermore, the as-deformed structures of the cast Fe-Si sheet following LSEM at room temperature were, for some conditions, characterized by significant inhomogeneous deformation. This is partially due to the coarse cast grain size $d \sim 500\ \mu$m. Consequentially, these inhomogeneous regions might produce different simple shear texture orientations and therefore make prediction of the bulk sheet properties significantly more difficult. Further texture analysis is underway to determine this more precisely.

7.2.3.1 Comparisons with Commercial Sheets

While the relative properties were as expected with the higher silicon content, B_{max} and μ_{max} values were again lower in absolute magnitude than expected for the cast compositions. The primary source of the lower values is, currently, not fully understood. However, a few plausible reasons are worth discussing. First, as with the 4wt%Si alloy specimens, the as-tested and annealed grain sizes were significantly smaller than those of the fully processed NGO and GO conditions. Since this aspect is the only common feature between the sheets produced from the two cast alloys and the 4wt%Si plate, it is a strong candidate to consider.

Second, while the IF steel contained very small amounts of detrimental carbon (0.002wt%), elemental analysis by ArcerlorMittal indicated that the virgin IF Steel contained (in wt%) 0.1Mn, 0.009P, 0.01S, 0.01Si, 0.02Cu, 0.01Ni, 0.01Mo, 0.03Cr, 0.06Al, 0.01Sn, and 0.054Ti. While only trace in amount, these additional micro-alloying components may have had some negative effects on the magnetic properties of the cast alloys, suggesting that other elements in addition to carbon should be minimized for high performance electrical steels.

Another consideration is the annealing treatment for the Fe-Si sheet specimens. The annealing was performed in air, which caused some visible oxidation of the steel surfaces. Prior to characterization, the oxides were removed using mechanical polishing and subsequently pickled in an acidic solution. Despite this procedure and the appearance of fresh metallurgical surfaces on both sides of the sheets prior to testing, some trace amounts of oxide may have remained on the sample surfaces. These may have slightly altered the measured properties, particularly the measured B_{max} values. However, previous experiments have shown that the oxide essentially has no measureable effect on the permeability and coercivity (not shown)

As a final comment, while the LSEM process was able to produce continuous sheets from the cast starting ingots, any residual cast defects that were not eliminated during processing could negatively impact the properties. Microscopy of the virgin cast ingot did not reveal any significant porosity and the low freezing range of the alloy, coupled with the small ingot geometry, did not lead to measurable macrosegregation. However, even

small amounts might be expected to negatively affect properties. Therefore, mentioning the possibility is important.

7.2.4 Implications and General Comments

Preliminary magnetic properties of the Fe-Si sheets studied here did not reveal competitive performance when compared to the two NGO and GO sheet grades of AK Steel. However, the essential takeaway is in demonstrating some preliminary magnetic properties analysis of shear-textured Fe-Si sheet. Most importantly, the properties of the well characterized Fe-4wt%Si shear-textured sheets aligned in good agreement with the predictions of a simple unit cell model for general BCC shear textures. This analysis suggests that the <111> fiber might dominate the magnetic properties by virtue of a high volume fraction. Furthermore, these results suggest that by virtue of engineering different shear textures in Fe-Si through a controlled deformation path in LSEM, or more generally, shear deformation, some range of magnetic properties could, in turn, be developed in Fe-Si sheets in a predictable manner. Note, while the basic unit cell model showed some interesting correlations with the measurements, it in itself is not a true predictive model for analyzing the effects of the full three dimensional shear texture on properties. As such, it should only be considered as a pilot attempt to quantify some general trends. Additionally, while the experimental sheet conditions did not have comparable properties to the two NGO and GO conditions, select NGO conditions currently sold by AK Steel possess only slight larger permeabilities (~6,000), which are significantly closer to the as-tested values for the Fe-Si specimens here. Consequentially, the simple shear process is an encouraging

approach to produce Fe-Si sheets with close to commercial performance to select NGO grades.

Furthermore, the LSEM process was shown to produce continuous sheets from the ideal Fe-6.5wt%Si composition in an as-cast form and without any workpiece preheating. This is especially impactful because of the extremely low ductility of the ideal Fe-Si composition. It should, in the future, be possible to continue the development of high silicon Fe-Si sheet for improved magnetic properties by accessing a wider range of compositions coupled with deeper texture control.

CHAPTER 8. SUMMARY AND FUTURE WORK

Simple shear deformation through conventional unconstrained (free) metal cutting and hybrid cutting extrusion *via* large strain extrusion machining (LSEM) was used to process continuous sheets from a variety of Fe-Si alloys, which are notorious for limited workability in conventional sheet thermomechanical processing. Through the use of high cutting velocities and deformation temperatures, a range of deformation structures were developed from homogeneous cold-worked type to shear localized material flows, which were then made homogeneous through the application of a constraint in LSEM. Processing-microstructure maps were developed to qualitatively identify respective flow morphologies as a function of deformation speed and temperature.

Simple shear crystallographic textures were found to develop in the Fe-Si sheet, defined by partial <111> and {110} fibers inclined relative to the sheet surface. Interestingly, these textures were found to be retained following recrystallization (annealing) treatments, both *in-situ* and post-processing. Through selection of the deformation path, the orientation (inclination) of these partial fibers was controlled over a significantly wide range, matching closely with the predictions from a geometric shear plane model. Select conditions were shown to develop magnetically important texture components (i.e., Goss and rotated Goss) when the deformation parameters were selected to promote large secondary shear deformation at the cutting tool-material interface. After high temperature annealing, grains in the secondary shear zone were found to preferentially

consume those in the body of sheet, deformed only by primary shear. The preferential grain growth is suggested to result from greater average grain boundary mobility in the local region.

Recrystallization kinetics were studied through a series of isothermal, incremental annealing experiments to elucidate the recrystallization mechanisms for retaining the deformation shear texture following annealing. Micrographs revealed a significantly more rapid and homogeneous recrystallization behavior in samples deformed by simple shear, compared to flat sheet rolling. From hardness measurements, recrystallization kinetics were obtained and compared using the JMAK kinetics model. The rolled specimen was characterized by a larger Avrami exponent, $n = 3$, compared to the much lower values of $n = 1.8$ and 1.4 for two different machining conditions. Differences were proposed to be the result of fundamentally different recovery and nucleation processes, classified by classical discontinuous recrystallization for the rolled condition and continuous recrystallization for the machined samples.

Preliminary magnetic properties were assessed using a closed circuit magnetic permeameter. Directional magnetic properties along the lengths of the two NGO and GO commercial standards were assessed with a series of experimental sheet conditions from Fe-4wt%Si, cast Fe-3.5wt%Si and cast Fe-6.5wt%Si alloys. Analysis of the processing-texture relationships revealed that the trend in magnetic properties as a function of sheet texture for the 4wt%Si alloy aligned well with a basic geometric unit cell model, suggesting that properties could, to a first-order, be qualitatively predicted from the model. Properties of the cast 3.5wt%Si were nominally similar to the 4wt%Si alloy, while the 6.5wt%Si

conditions exhibited higher maximum relative permeability and lower coercivity, hysteresis loss and maximum induction. Deviations between the properties of the experimental conditions and commercial sheets were suggested to be related mostly to alloy purity and grain size, both of which were lower for the experimental conditions.

8.1 Future Work

The texture character was found to be retained during annealing treatments. However, annealing atmospheres and temperatures are known to influence texture development. It is therefore recommended that more detailed annealing studies be performed on the shear-textured Fe-Si sheets, especially at higher grain growth temperatures to document any effects. Furthermore, due to the particularly interesting textures at a shear plane angle of 0° with the Goss fiber, an in-depth study of varying secondary shear thicknesses is warranted. In particular, it would be useful to conduct a series of LSEM experiments on the exact commercial Fe-Si composition that undergoes abnormal grain growth during rolling and impose significant secondary shear deformation in this type of sheet. Perhaps conditions could be produced with the Goss fiber and preferential grain growth of the secondary shear zone could occur during high temperature annealing to yield a Goss fiber orientation throughout the sheet thickness. Properties of this hypothetical sheet would be interesting to evaluate.

Additionally, continued development of the magnetic properties model would be useful to include the orientation of the <001> directions for the full three-dimensional simple shear texture fibers. This would more adequately characterize the textures and provide a better basis for future processing-texture-properties relationships. Magnetic

properties should also be measured in more detail from a wider range of iron-silicon alloys with simple shear textures and with higher purity.

LIST OF REFERENCES

LIST OF REFERENCES

1. M. F. Littmann, IEEE Trans. Magn. **7**, 48 (1970).
2. Office of Energy Efficiency and Renewable Energy, *Energy Conservation Standard for Distribution Transformers: Notice of Proposed Rulemaking Technical Support Document* (2012).
3. J. M. D. Coey, *Magnetism and Magnetic Materials* (2010).
4. J. L. Walter, in *Sorby Centen. Symp. Hist. Metall.* (1963), pp. 519–540.
5. H. Haiji, K. Okada, T. Hiratani, M. Abe, and M. Ninomiya, J. Magn. Magn. Mater. **160**, (1996).
6. Y. Takada, M. Abe, S. Masuda, and J. Inagaki, J. Appl. Phys. **64**, 5367 (1988).
7. M. Abe, Y. Takada, T. Murakami, Y. Tanaka, and Y. Mihara, **11**, 109 (1989).
8. Q. F.-S. Ribbon, C. F. Chang, V. Laxmanan, and S. K. Das, IEEE Trans. Magn. **M**, 6 (1984).
9. B. Cullity and C. Graham, *Introduction to Magnetic Materials* (2011).
10. D. Sagapuram, M. Efe, W. Moscoso, S. Chandrasekar, and K. P. Trumble, Acta Mater. **61**, 6843 (2013).
11. D. Sagapuram, A. B. Kustas, W. Dale Compton, K. P. Trumble, and S. Chandrasekar, **137**, 1 (2015).
12. C. Chen, *Magnetism and Metallurgy of Soft Magnetic Materials* (1986).
13. A. J. Moses, IEE Proc. A **137**, 233 (1990).
14. W. F. Barrett, W. Brown, and R. A. Hadfield, Sci. Trans. Roy. Soc. Dublin **7**, 67 (1900).
15. T. D. Yensen and N. A. Ziegler, Trans. A.S.M. **23**, 337 (1936).
16. N. P. Goss, Trans. A.S.M. **23**, 511 (1935).
17. R. M. Bozorth, in *Ferromagnetism* (1993), p. 79.
18. G. E. Lakso and M. J. Marcinkowski, Metall. Trans. **5**, 839 (1974).
19. F. González and Y. Houbaert, Rev. Metal. **49**, 178 (2013).
20. D. W. Dietrich, in *ASM Handb. Vol 2* (1990), pp. 761–781.
21. H. Fu, Z. Zhang, Y. Jiang, and J. Xie, Mater. Lett. **65**, 1416 (2011).
22. G. Tian and X. Bi, J. Alloys Compd. **502**, 1 (2010).
23. C. Bolfarini, M. C. A. Silva, A. M. Jorge, C. S. Kiminami, and W. J. Botta, J. Magn. Magn. Mater. **320**, e653 (2008).
24. R. Li, Q. Shen, L. Zhang, and T. Zhang, J. Magn. Magn. Mater. **281**, 135 (2004).
25. O. Kubaschewski, in *Iron-Binary Phase Diagrams* (1982), pp. 136–139.
26. C. Chen, *Chih-Wen Chen* (1977).

27. T. D. Yensen, Trans. Am. Inst. Electr. Eng. **XLIII**, 145 (1924).
28. J. G. Benford, J. Appl. Phys. **38**, 1100 (1967).
29. D. A. Leak and G. M. Leak, J. Iron Steel Inst. 190 (1957).
30. R. PremKumar, I. Samajdar, N. N. Viswanathan, V. Singal, and V. Seshadri, J. Magn. Magn. Mater. **264**, 75 (2003).
31. Y. H. Sha, F. Zhang, S. C. Zhou, W. Pei, and L. Zuo, J. Magn. Magn. Mater. **320**, 393 (2008).
32. L. Kestens and S. Jacobs, Texture, Stress. Microstruct. **2008**, (2008).
33. D. S. Petrovic, Mater. Technol. **44**, 317 (2010).
34. Y. Shimizu, Y. Ito, and Y. Iida, Metall. Mater. Trans. A **17**, 1323 (1986).
35. S. Mishra, Acta Mater. **32**, (1984).
36. D. Dorner, S. Zaefferer, L. Lahn, and D. Raabe, J. Magn. Magn. Mater. **304**, 183 (2006).
37. D. Dorner, S. Zaefferer, and D. Raabe, Acta Mater. **55**, 2519 (2007).
38. F. J. G. Landgraf, Jom **64**, 764 (2012).
39. K. Matsumura and B. Fukuda, IEEE Trans. Magn. **20**, 1533 (1984).
40. P. Rodríguez-Calvillo, Y. Houbaert, R. Petrov, L. Kestens, and R. Colás, Mater. Chem. Phys. **136**, 710 (2012).
41. F. Sorbello, P. E. J. Flewitt, G. Smith, and A. G. Crocker, Acta Mater. **57**, 2646 (2009).
42. D. Hull, Acta Metall. **9**, 191 (1961).
43. C. C. Lima, M. C. A. da Silva, M. D. C. Sobral, R. E. Coelho, and C. Bolfarini, J. Alloys Compd. **586**, S314 (2014).
44. M. Efe, Extrusion Machining: A Thermo-Mechanical Process for Producing Strips of Alloys Having Limited Workability, 2013.
45. W. Moscoso, Severe Plastic Deformation and Nanostructured Materials by Large Strain Extrusion Machining, 2008.
46. D. Sagapuram, H. Yeung, Y. Guo, A. Mahato, R. M'Saoubi, W. D. Compton, K. P. Trumble, and S. Chandrasekar, CIRP Ann. - Manuf. Technol. **64**, 49 (2015).
47. M. A. Meyers, G. Subhash, B. K. Kad, and L. Prasad, Mech. Mater. **17**, 175 (1994).
48. U. Andrade, M. A. Meyers, K. S. Vecchio, and A. H. Chokshi, **42**, 3183 (1994).
49. A. B. Kustas, D. Sagapuram, S. Chandrasekar, and K. P. Trumble, IOP Conf. Ser. Mater. Sci. Eng. **82**, 012054 (2015).
50. A. B. Kustas, D. Sagapuram, K. P. Trumble, and S. Chandrasekar, Metall. Mater. Trans. A **47**, 3095 (2016).
51. M. Cockcroft and D. Latham, J Inst Met. **96**, 33 (1968).
52. W. A. Backofen, *Deformation Processing* (Addison-Wesley Publishing Company, Inc., 1972).
53. M. Efe, W. Moscoso, K. P. Trumble, W. Dale Compton, and S. Chandrasekar, Acta Mater. **60**, 2031 (2012).
54. Y. Guo, M. Efe, W. Moscoso, D. Sagapuram, K. P. Trumble, and S. Chandrasekar, Scr. Mater. **66**, 235 (2012).
55. D. Sagapuram, Controlling Microstructure and Texture in Magnesium Alloy Sheet by Shear-Based Deformation Processing, 2013.
56. T. Ros-Yáñez, J. Barros, R. Colás, and Y. Houbaert, ISIJ Int. **43**, 447 (2003).

57. J. Xie, H. Fu, Z. Zhang, and Y. Jiang, Mater. Sci. Eng. A **538**, 315 (2012).
58. C. N. Reid, Metall. Trans. A **12**, 371 (1981).
59. M. Atake, M. Barnett, B. Hutchinson, and K. Ushioda, Acta Mater. **96**, 410 (2015).
60. S. M. Fatemi-Varzaneh, A. Zarei-Hanzaki, and H. Beladi, Mater. Sci. Eng. A **456**, 52 (2007).
61. T. Sakai and J. J. Jonas, Acta Metall. **32**, 189 (1984).
62. D. Smolenicki, J. Boos, F. Kuster, H. Roelofs, and C. F. Wyen, CIRP Ann. - Manuf. Technol. **63**, 97 (2014).
63. I. J. Beyerlein and S. L. Toth, Prog. Mater. Sci. **54**, (2009).
64. S. Li, I. J. Beyerlein, and M. a. M. Bourke, Mater. Sci. Eng. A **394**, 66 (2005).
65. A. Belyakov, T. Sakai, H. Miura, R. Kaibyshev, and K. Tsuzaki, Acta Mater. **50**, 1547 (2002).
66. Y. H. Jin and M. Y. Huh, **9**, 5311 (2004).
67. C. Y. Yu, P. L. Sun, P. W. Kao, and C. P. Chang, Mater. Sci. Eng. A **366**, 310 (2004).
68. a. Takayama, X. Yang, H. Miura, and T. Sakai, Mater. Sci. Eng. A **478**, 221 (2008).
69. H. Jazaeri and F. J. Humphreys, Acta Mater. **52**, 3239 (2004).
70. H. Jazaeri and F. J. Humphreys, Acta Mater. **52**, 3251 (2004).
71. F. J. Humphreys, Acta Mater. **45**, 4231 (1997).
72. S. Zaefferer and N. Chen, Solid State Phenom. **105**, 29 (2005).
73. W. Guo and W. Mao, J. Mater. Sci. Technol. **26**, 759 (2010).
74. R. D. Doherty, D. A. Hughes, F. J. Humphreys, J. J. Jonas, D. J. Jensen, M. E. Kassner, W. E. King, T. R. McNelley, H. J. McQueen, and A. D. Rollett, Mater. Sci. Eng. A **238**, 219 (1997).
75. F. J. Humphreys and M. Hatherly, *Recrystallization and Related Annealing Phenomena (Second Edition)* (1977).
76. F. J. Humphreys, Mater. Sci. Technol. **8**, 135 (1992).
77. A. D. Rollett, D. J. Srolovitz, R. D. Doherty, and M. P. Anderson, Acta Metall. **37**, 627 (1989).
78. E. Woldt and D. J. Jensen, Metall. Mater. Trans. A **26**, 1717 (1995).
79. N. X. Sun, X. D. Liu, and K. Lu, Scr. Mater. **34**, 1201 (1996).
80. K. K. Surthi, R. K. Khatirkar, and S. G. Sapate, ISIJ Int. **53**, 356 (2013).
81. W. Ye, R. L. Gall, and G. Saindrenan, Mater. Sci. Eng. A **A332**, 41 (2002).
82. J. Sievert, **216**, (2000).
83. J. Sievert and H. Ahlers, Bull. Mater. Sci. **17**, 1393 (1994).
84. F. Fiorillo, Metrologia **47**, S114 (2010).
85. a Aharoni, J. Appl. Phys. **83**, 3432 (1998).
86. D. X. Chen, IEEE Trans. Magn. **41**, 2077 (2005).
87. ASTM, *ASTM A343/A343M-14: Standard Test Method for Alternating-Current Magnetic Properties of Materials at Power Frequencies Using Wattmeter-Ammeter-Voltmeter Method and 25-Cm Epstein Test Frame 1* (2014).
88. ASTM, Annu. B. ASTM Stand. **95**, 1 (2011).
89. H. Czichos, T. Saito, and L. Smith, in *Springer Handb. Mater. Meas. Methods* (2006).
90. A. Steel, *Oriented & TRAN-COR H Electrical Steels* (n.d.).
91. A. Steel, *NONORIENTED ELECTRICAL STEELS* (2013).

92. ASTM, *ASTM A804/A804M-04: Standard Test Methods for Alternating-Current Magnetic Properties of Materials at Power Frequencies Using Sheet-Type Test Specimens 1* (2004).
93. E. Steingroever and G. Ross, *Magnet-Physics Inc. - Magnetic Measuring Techniques Manual* (2009).

VITA

VITA

Andrew Benjamin Kustas was born and raised in Colorado, where he attended Chaparral High School in Parker, CO until 2007. While in high school, he worked as an engineering technician for his father's company, Engineered Coatings, Inc. He received his Bachelor of Science degree in Mechanical Engineering 2012 from Colorado State University in Fort Collins, CO. While at Colorado State, he participated in several research projects at the Colorado State University Electric Propulsion and Plasma Engineering Laboratory (CEPPE Lab) from 2009 to 2012. Additionally, he worked for Lockheed Martin Aeronautics in Fort Worth, TX during the 2011 summer as a college intern. In 2012, he began his graduate studies at Purdue University in West Lafayette, IN in the School of Materials Engineering. After receiving a Doctor of Philosophy degree from Purdue, he will transition to a postdoctoral research position at Sandia National Labs in Albuquerque, NM in the Material Mechanics and Tribology Group.